

Baldini, J. U. L., Lechleitner, F. A., Breitenbach, S. F. M., van Hunen, J., Baldini, L. M., Wynn, P. M., Jamieson, R. A., Ridley, H. E., Baker, A. J., Walczak, I. W., Fohlmeister, J. (2021): Detecting and quantifying palaeoseasonality in stalagmites using geochemical and modelling approaches. - Quaternary Science Reviews, 254, 106784.

<https://doi.org/10.1016/j.quascirev.2020.106784>

1 Detecting and quantifying palaeoseasonality in stalagmites using geochemical
2 and modelling approaches

3 James U.L. Baldini¹, Franziska A. Lechleitner^{2, 3}, Sebastian F.M. Breitenbach⁴, Jeroen van
4 Hunen¹, Lisa M. Baldini⁵, Peter M. Wynn⁶, Robert A. Jamieson⁷, Harriet E. Ridley¹, Alex J.
5 Baker⁸, Izabela W. Walczak⁹, and Jens Fohlmeister^{10, 11}

6 ¹Department of Earth Sciences, Durham University, DH1 3LE, United Kingdom.

7 ²Department of Earth Sciences, University of Oxford, South Parks Road, Oxford OX1 3AN,
8 United Kingdom.

9 ³Laboratory for the Analysis of Radiocarbon with AMS (LARA), Department of Chemistry and
10 Biochemistry, and Oeschger Centre for Climate Change Research, University of Bern,
11 Freiestrasse 3, 3012 Bern, Switzerland.

12 ⁴Department of Geography and Environmental Sciences, Northumbria University,
13 Newcastle upon Tyne, NE1 8ST, United Kingdom.

14 ⁵School of Health & Life Sciences, Teesside University, Middlesbrough, TS1 3BX, United
15 Kingdom

16 ⁶Lancaster Environment Centre, Lancaster University, Lancaster, LA1 4YQ, United Kingdom.

17 ⁷School of Earth and Environment, University of Leeds, Leeds, LS2 9JT, United Kingdom

18 ⁸National Centre for Atmospheric Science and Department of Meteorology, University of
19 Reading, RG6 6BB, United Kingdom.

20 ⁹Durham Centre for Academic Development, Durham University, Durham, DH1 1TA, United
21 Kingdom.

22 ¹⁰Potsdam Institute for Climate Impact Research, Telegrafenberg, 14473 Potsdam, Germany.

23 ¹¹GFZ German Research Centre for Geosciences, Section 'Climate Dynamics and Landscape
24 Development', Telegrafenberg, 14473 Potsdam, Germany.

25

26

27

28 **Abstract**

29 Stalagmites are an extraordinarily powerful resource for the reconstruction of climatological
30 palaeoseasonality. Here, we provide a comprehensive review of different types of
31 seasonality preserved by stalagmites and methods for extracting this information. A new
32 drip classification scheme is introduced, which facilitates the identification of stalagmites
33 fed by seasonally responsive drips and which highlights the wide variability in drip types
34 feeding stalagmites. This hydrological variability, combined with seasonality in Earth
35 atmospheric processes, meteoric precipitation, biological processes within the soil, and cave
36 atmosphere composition means that every stalagmite retains a different and distinct (but
37 correct) record of environmental conditions. Replication of a record is extremely useful but
38 should not be expected unless comparing stalagmites affected by the same processes in the
39 same proportion. A short overview of common microanalytical techniques is presented, and
40 suggested best practice discussed. In addition to geochemical methods, a new modelling
41 technique for extracting meteoric precipitation and temperature palaeoseasonality from
42 stalagmite $\delta^{18}\text{O}$ data is discussed and tested with both synthetic and real-world datasets.
43 Finally, world maps of temperature, meteoric precipitation amount, and meteoric
44 precipitation oxygen isotope ratio seasonality are presented and discussed, with an aim of
45 helping to identify regions most sensitive to shifts in seasonality.

46

47 **1. Introduction**

48 Over the past few decades stalagmites have become one of the most important terrestrial
49 archives of climate and environmental change. Their widespread distribution, amenability to

50 radiometric dating, and capacity for retaining seasonal- to decadal-scale environmental
51 information have made them indispensable archives for a wide variety of climate information,
52 most commonly rainfall or temperature variability. The field has developed rapidly, and it is
53 now clear that stalagmites generally do not record a single climate parameter (e.g., cave
54 temperature, rainfall amount, etc.) exclusively, but instead record a combination of
55 processes. It is increasingly acknowledged that every stalagmite contains a robust history of
56 some aspect of environmental change. The issue is one of complexity; generally speaking, the
57 stalagmite with the least complex signal is considered the ideal. Records generated from
58 stalagmites with more complex stratigraphies, whose drip flow route changes through time,
59 or that are influenced by numerous environmental processes, often prove more difficult to
60 interpret. Some stalagmite records may miss short-lived climate excursions because they are
61 fed by drips that do not respond to the transient climate forcing in question. Others might
62 lose sensitivity or respond non-linearly to a climate forcing; for example, a stalagmite might
63 record droughts faithfully, but miss exceptionally wet intervals when the epikarst (the highly
64 fractured transition zone between soil and bedrock) is saturated with water. To exacerbate
65 the issue further, most published stalagmite records lack the requisite analytical resolution to
66 detect palaeoseasonality, an aspect of the climate signal that is increasingly recognised as
67 critical to the interpretation of geochemical records from stalagmites (Baldini et al., 2019;
68 Morellón et al., 2009; Moreno et al., 2017). In other words, the desired climate signal is often
69 compromised by: i) inherent complexities associated with the hydrological transfer of the
70 climate signal to the stalagmite, ii) overprinting of the desired climate-driven signal by other
71 environmental variables, and iii) bias introduced via the necessarily selective sampling of the
72 stalagmite for analysis. The challenge for palaeoclimatologists is to extract and correctly
73 interpret the desired climate signal from a stalagmite, bearing these complexities in mind.

74 The detection of a seasonality signal within a stalagmite can greatly help interpret all datasets
75 from a stalagmite sample, of any temporal resolution. For example, the detection of a
76 seasonal geochemical cycle can contribute to chronological models (Baldini et al., 2002;
77 Carlson et al., 2018; Ridley et al., 2015b), in some cases permitting the development of high-
78 precision chronologies over extended time intervals (Ban et al., 2018; Carlson et al., 2018;
79 Duan et al., 2015; Nagra et al., 2017; Ridley et al., 2015b; Smith et al., 2009). Unlike most
80 other laminated records (e.g., tree rings, ice cores), high-precision radiometric dates can
81 anchor stalagmite layer count chronologies, reducing accumulated counting errors. Proxy
82 information from laminated stalagmites can be linked to environmental variability at seasonal
83 resolution (Mattey et al., 2010; Orland et al., 2019; Ridley et al., 2015b), allowing much
84 needed insights into past climatic dynamics that are difficult to obtain otherwise.

85 The fact that stalagmites can reveal palaeoseasonality, a notoriously difficult climate
86 parameter to reconstruct, is critical for identifying wholesale shifts in climate belts. For
87 example, monthly-scale geochemical data from a stalagmite has detected variability in the
88 Intertropical Convergence Zone influence on rainfall seasonality in Central America over the
89 last two millennia (Asmerom et al., 2020) and the shift from a maritime to a more continental
90 climate in western Ireland in the early Holocene (Baldini et al., 2002), transitions which must
91 otherwise be inferred using annual- to centennial-resolution data (e.g., Breitenbach et al.,
92 2019). High spatial resolution approaches yielding palaeoseasonality can distinguish rainfall
93 occurring at different times of the year, for example, monsoonal rainfall versus dry season
94 rainfall (Ban et al., 2018; Ronay et al., 2019), providing a wealth of information unattainable
95 by other means.

96 Seasonality is one of climate's most important aspects, and this is reflected in the basic
97 subdivisions of the Köppen system, the most commonly used climate classification scheme
98 (Köppen, 1918; Peel et al., 2007). Reconstructing past seasonality is not only relevant for pure
99 palaeoclimatological studies, but also for palaeobotany and archaeology, and for establishing
100 a benchmark by which to compare recent changes in seasonality during the Anthropocene;
101 recent research suggests seasonality in rainfall (e.g., Feng et al., 2013) and temperature (e.g.,
102 Santer et al., 2018) are shifting under modern climate change. This is particularly concerning
103 because changing seasonality has had broad ecological and social implications in the past. For
104 example, human dispersal through Asia was limited more by water availability than by
105 temperature, and likely followed habitable corridors with favourable rainfall seasonality (Li et
106 al., 2019; Parton et al., 2015; Taylor et al., 2018). Also, the domestication and dispersal of
107 crops are linked to rainfall seasonality because optimal growth conditions depend on
108 hydrological conditions. In the Fertile Crescent, barley and wheat were sown in autumn,
109 because in this semi-arid region the winter rains are the limiting factor for their prosperity
110 (Spengler, 2019). Similarly, abundant evidence now exists that variability in seasonal rainfall
111 has played a key role in the waxing and waning of major civilisations (Hsiang et al., 2013;
112 Kennett et al., 2012).

113 Despite the clear importance of reconstructing palaeoseasonality, it is rarely directly
114 observable in climate proxy records. The obfuscation of seasonality by undersampling or
115 aliasing is often a consequence of logical and pragmatic choices designed to maximise returns
116 from available resources. Ideally, analyses would resolve nearly the full climate signal residing
117 within every stalagmite, but this is neither logistically (given the time and funding required)
118 nor realistically (given that the karst system transmutes the signal) possible.

119 Here we review both the advantages of obtaining palaeoseasonality information and methods
120 for its reconstruction using stalagmite geochemistry and modelling, as well as common issues
121 in extracting this information. A short review of the history of speleothem science and
122 techniques frames the discussion and highlights how speleothems have become the premier
123 archives for annual- to sub-annual scale terrestrial climate reconstructions, particularly during
124 the Quaternary. We also suggest a methodology to maximise the likelihood of successfully
125 extracting palaeoseasonality information from a stalagmite, including evaluating the
126 hydrological characteristics of the drip feeding a stalagmite sample prior to collection,
127 modelling palaeoseasonality from lower resolution data, and determining the seasonality of
128 the climate at (and in regions near) the site.

129

130 **2. Background and technique development**

131 Very early studies demonstrated the potential of stalagmites to record climate information
132 (Allison, 1923, 1926; Broecker, 1960; Orr, 1952). However, the real growth in the application
133 of stalagmites as climate archives occurred after the convergence of Thermal Ionisation Mass
134 Spectrometry (TIMS) uranium-thorium dating of stalagmites in the 1990s (e.g., Edwards et al.,
135 1987; Edwards and Gallup, 1993) (which allowed accurate dating) and high resolution
136 sampling techniques in the 2000s (permitting the reconstruction of climate on sub-decadal
137 timescales). The subsequent development and proliferation of multi-collector inductively
138 coupled plasma mass spectrometry (MC-ICP-MS) permitted extraordinarily robust (precise
139 and accurate) chronological control (e.g., Cheng et al., 2013; Hellstrom, 2003; Hoffmann et
140 al., 2007), while the development of a variety of microanalytical techniques provided climate
141 proxy information of an unparalleled temporal resolution. The realisation in the late 1990s

142 (Roberts et al., 1998) and early 2000s that stalagmite carbonate trace element compositions
143 and isotope ratios often vary seasonally (Baldini et al., 2002; Fairchild et al., 2000; McMillan
144 et al., 2005; Treble et al., 2003; Treble et al., 2005b) opened the door to the investigation of
145 palaeoseasonality on an unprecedented level.

146

147 **2.1. Increasing resolution of analysis**

148 Immense technical progress has facilitated the transition from the first speleothem studies,
149 which broadly placed periods of speleothem growth into the global climatic context (Harmon,
150 1979; Hendy and Wilson, 1968; Thompson et al., 1975), to studies adopting increasingly
151 detailed sub-annual resolution sampling (Fairchild et al., 2001; Johnson et al., 2006; Liu et al.,
152 2013; Matthey et al., 2008; Maupin et al., 2014; Myers et al., 2015; Ridley et al., 2015b; Ronay
153 et al., 2019; Treble et al., 2005a). Methodological developments, particularly after the mid-
154 2000s and particularly with respect to trace element analysis, greatly reduced the required
155 sample size and increased measurement precision. This included the widespread adoption of
156 micromilling techniques (Spötl and Matthey, 2006), laser ablation (Müller et al., 2009; Treble
157 et al., 2003), secondary ionisation mass spectrometry (Baldini et al., 2002; Fairchild et al.,
158 2001; Finch et al., 2001; Kolodny et al., 2003; Orland et al., 2008, 2009), and the development
159 of protocols for stable carbon and oxygen isotope measurements with reduced sample sizes
160 (Breitenbach and Bernasconi, 2011), including cold-trap methods capable of analysing less
161 than 5 µg of carbonate powders (Vonhof et al., 2020).

162 Here, we apply the recently compiled Speleothem Isotope Synthesis and Analysis (SISAL)
163 database v1b (Atsawawaranunt et al., 2018; Comas-Bru et al., 2019) to document the

164 evolution of speleothem stable isotope record resolution. SISAL was created with the primary
165 objective of providing access to a comprehensive repository of published stalagmite $\delta^{18}\text{O}$
166 records to the palaeoclimate community and for climate model evaluation (Comas-Bru and
167 Harrison, 2019; Comas-Bru et al., 2019). SISALv1b contains 455 speleothem records (i.e., SISAL
168 'entities') from 211 globally distributed caves published since 1992 (Comas-Bru et al., 2019).
169 More than half the records (264) included in the database cover at least portions of the last
170 10,000 years.

171 To investigate how stable isotope record resolution has evolved over the last three decades,
172 we extracted all records from the database and calculated their temporal resolution as the
173 absolute difference between two consecutive samples. Hiatuses and gaps in the individual
174 records were excluded from the analysis, as these would have erroneously suggested much
175 lower resolution than that actually present. In a second step, we performed the same
176 calculation, considering only Holocene records.

177 The analysis reveals how the number of speleothem stable isotope records steadily increased
178 with publication year (Figure 1), highlighting the increased popularity of speleothem science
179 over the past three decades. A trend of increasing temporal resolution with time becomes
180 apparent after binning all records published in the same year and calculating their mean
181 resolution (Figure 1). This trend becomes even clearer when only Holocene records are
182 considered, with a particularly striking increase in resolution over recent years (post-2010)
183 (records pre-2010: mean resolution = 50.1 years, STDEV = 38.9 years; records between 2010
184 and 2018: mean resolution = 16.5 years, STDEV = 7.4 years), and is likely related to the
185 widespread adoption of microanalytical advances. Additionally, a record's resolution will
186 typically depend on the time period covered by the record; in general, resolution is higher in

187 Holocene records compared to the full dataset, which includes older records as well. This
188 partly arises because of greater availability of independent data and information on climate
189 conditions during more recent time intervals, thus requiring higher resolution records to
190 tackle relevant research questions. It may also be partially due to typically lower growth rates
191 during the last glaciation compared to the Holocene. However, overall, only nine of the
192 records in SISALv1b have resolution <0.5 years, directly allowing for investigations of
193 paleoseasonality. This highlights the difficulties often encountered with conventional
194 sampling techniques, as this compilation only includes stable isotope records, and does not
195 consider other methods (e.g., laser ablation trace element analysis), which can generate
196 higher resolution time-series. The increasing resolution possible via technological
197 developments has largely involved the analysis of trace elements, whereas stable isotope
198 analysis still predominantly relies on micromilling or drilling techniques.

199

200 **2.2. Transition from temperature to rainfall amount to seasonality**

201 Early speleothem palaeoclimate studies focused on using $\delta^{18}\text{O}$ to generate quantitative cave
202 temperature records (Gascoyne et al., 1980; Hendy and Wilson, 1968; Lauritzen, 1995;
203 Lauritzen and Lundberg, 1999), based on the insight that oxygen isotope fractionation during
204 carbonate deposition is temperature dependent (Epstein et al., 1951; O'Neil et al., 1969), and
205 building on similar work on marine carbonates (Emiliani, 1955). It was quickly recognised
206 however that speleothem $\delta^{18}\text{O}$ is a complex mixed signal reflecting variations in cave
207 temperature, changes in dripwater isotope composition, and various kinetic effects, which
208 severely hamper the use of this proxy for quantitative temperature reconstructions
209 (McDermott, 2004). The subsequent shift in how speleothem $\delta^{18}\text{O}$ is interpreted led to its

210 establishment as a proxy for past hydroclimate changes, including atmospheric circulation,
211 regional temperature, moisture source dynamics, and amount of precipitation (Lachniet,
212 2009).

213 At the same time, the toolkit of geochemical proxies available to speleothem researchers
214 continued to expand. In particular, trace element concentrations in speleothem carbonate
215 emerged as tracers for numerous processes, from surface productivity to karst hydrology and
216 transport (Borsato et al., 2007; Fairchild et al., 2001; Huang and Fairchild, 2001; Treble et al.,
217 2005a). The combination of multiple proxies measured on the same speleothem provided a
218 means to disentangle complexities regarding mixed signals in individual proxies and allowed
219 a progressively deeper understanding of the archive and the associated processes in soil,
220 karst, atmosphere, and cave. In tandem with these developments regarding the climate proxy
221 development, monitoring of cave and local atmospheric conditions became increasingly
222 important, as it was recognised that understanding sometimes highly localised controls on
223 geochemical signatures is crucial for their interpretation (Genty, 2008; Matthey et al., 2008;
224 Matthey et al., 2010; Spötl et al., 2005; Verheyden et al., 2008).

225 The presence of annual petrographic cyclicity within stalagmites was recognised very early on
226 (Allison, 1926). The later identification of visible and luminescent annual banding (Baker et
227 al., 1993; Broecker, 1960; Shopov et al., 1994) underscored that the deposition, mineralogy,
228 and chemical composition of speleothems varied seasonally. However, the concept of
229 seasonal shifts in climate variables (e.g., temperature, precipitation) as contributing to the
230 net multi-annual climate signal did not gain traction until the early to mid-2000s (Wang et al.,
231 2001). Cave monitoring revealed drip rate seasonality in Pere Noel Cave, Belgium (Genty and
232 Deflandre, 1998), Crag Cave, Ireland (Baldini et al., 2006), and in Soreq Cave, Israel (Ayalon et

233 al., 1998), and seasonality was discussed within the context of a speleothem-based trace
234 element study at Grotta di Ernesto, Italy (Huang et al., 2001). Meteorological data were
235 compared to seasonal trace element data for an Australian stalagmite (Treble et al., 2003),
236 and the potential to use seasonal-scale geochemical data to reconstruct the East Asian
237 Summer Monsoon (EASM) was investigated using a stalagmite from Heshang Cave, China
238 (Johnson et al., 2006). Studies coupling cave environmental monitoring and ‘farmed’
239 carbonate precipitates were critical for clarifying the links between hydrological and cave
240 atmosphere conditions on the chemistry of stalagmites, including at a seasonal scale
241 (Czuppon et al., 2018; Moerman et al., 2014; Sherwin and Baldini, 2011; Tremaine et al.,
242 2011). Drip monitoring was also key for establishing how cave hydrology attenuates seasonal
243 and interannual rainfall variability, and was used to predict ENSO variability preservation
244 within stalagmites (Chen and Li, 2018; Moerman et al., 2014). These studies all illustrate that
245 a thorough understanding of annual geochemical cycles requires the development of
246 extensive cave monitoring records, which highlight the complexities inherent in signal
247 transfer from surface environment to the stalagmite.

248

249 **2.3. Importance of monitoring for understanding the seasonal signal**

250 Monitoring environmental conditions in and above a cave at a high temporal resolution
251 greatly improves the accuracy of palaeoclimate interpretations derived from stalagmites.
252 Linking proxy characteristics at a given site with current environmental conditions via
253 monitoring is relevant for reconstructing past conditions. Although modern conditions may
254 differ from ancient conditions, monitoring the cave environment clarifies processes operating
255 at a site, including the timing and extent of ventilation and the general nature of a

256 hydrological signal, acknowledging that some hydrological re-routing may have occurred
257 through time for certain drip types.

258 Understanding a stalagmite geochemical proxy record is difficult without first understanding
259 how that signal is transferred and altered from the external environment to the sample.
260 Environmental changes affecting the seasonal signal fall under four main categories: *i) Earth*
261 *atmospheric, ii) meteoric precipitation, iii) biological* (e.g., soil processes), and *iv) cave*
262 *atmospheric*.

263 *Earth atmospheric* processes affect the seasonality signal retained within stalagmites by
264 influencing meteoric precipitation isotope ratios at the cave site. Possibly the most common
265 atmospheric process is the seasonal variation in precipitation $\delta^{18}\text{O}$ induced by shifts in the
266 temperature-dependent water vapour-meteoric precipitation fractionation factor. Other
267 related changes in atmospheric processing include seasonal shifts in moisture source and
268 pathway of the moisture package to the cave site, as, for example, in monsoonal settings.

269 *Meteoric precipitation* variability regards the nature of the primary rainfall amount-derived
270 seasonality signal. Here we include meteoric precipitation amount and seasonal distribution
271 as separate from 'Earth atmospheric' processes (such as changes in moisture source),
272 although clearly the latter affect the former. Meteoric precipitation is a fundamental control
273 on stalagmite seasonality that is worth considering independently of other atmospheric
274 processes. Stalagmites deposited in monsoonal climates (e.g., the East Asian Summer
275 Monsoon, Indian Summer Monsoon, South American Monsoon, and Australian Summer
276 Monsoon) with distinct wet and dry seasons are excellent examples of samples whose
277 geochemistry generally (but not always) responds to hydrologic seasonality. In temperate
278 mid-latitude settings with more evenly distributed rainfall, hydrological shifts might record

279 less seasonal than inter-annual (e.g., ENSO) dynamics or possess a seasonal bias (see section
280 3.1) derived from effective infiltration dynamics.

281 **Biological (soil-derived)** seasonality is the least clearly defined control, and predominantly
282 affects the trace element composition and carbon isotope ratio of cave percolation waters.
283 However, evidence also exists that increased soil bioproductivity can affect oxygen isotope
284 ratios by preferential uptake of water during the growing season during intervals with
285 substantial surface vegetation (Baldini et al., 2005). Trace element transport critically
286 depends on the biological activity and water supply, both factors that are inherently variable
287 and not necessarily in-phase. Hydrology can affect biological seasonality, as leaching of
288 organic matter and trace elements from freshly decomposed litter depends on excess
289 infiltration. Soils may thus produce a wet season pulse of colloidal material (organics as well
290 as weathering products) which contributes to an annual peak in trace element concentrations
291 in some samples; such dynamics are highly site-specific. The evidence for this pulse is derived
292 both from synchrotron-based stalagmite studies (e.g., Borsato et al., 2007) and daily-scale
293 automated dripwater collection schemes (Baldini et al., 2012). Treble et al. (2003) suggest
294 phosphorous enrichment in stalagmite carbonate stemming from seasonal infiltration pulses,
295 and monitoring at Shihua Cave (China) revealed that organic carbon was transported during
296 the wet season (Ban et al., 2018; Tan et al., 2006). Whether this pulse is truly independent
297 from hydrological variability is unclear, but some evidence from dripwater monitoring in
298 temperate Irish caves suggests that the seasonal trace element pulse is not associated with
299 increased autumnal water throughput, but rather with seasonal vegetation die-back (Baldini
300 et al., 2012). In monsoonal north-eastern India biologically-induced litter decomposition
301 reaches a maximum in early summer (Ramakrishnan and Subhash, 1988), which increases

302 element availability in the soil that can be leached during the entire wet season (Khiewtam
303 and Ramakrishnan, 1993). Trace element transport may also hinge directly on the presence
304 of natural organic matter in dripwater, which may link the dripwater directly to surface
305 bioproductivity (Hartland et al., 2012; Hartland et al., 2011). Thus, biological seasonality is
306 highly site-specific and likely variable through time; this and the complexities outlined above,
307 underscore the importance of dripwater monitoring campaigns.

308 **Cave atmospheric** variability can also impart a seasonal signal to a stalagmite geochemical
309 record. Seasonal changes in cave air mixing with outside air lead to conditions within the cave
310 that lower cave air carbon dioxide partial pressure ($p\text{CO}_2$) and potentially even contribute to
311 dripwater evaporation, promoting calcite deposition. Cave atmosphere variability, induced by
312 ventilation (through thermal gradients or changing wind patterns) therefore affects the
313 calcite deposition seasonality, as well as kinetic fractionation amount. Excellent examples of
314 caves whose stalagmites are affected by this variability include New St. Michael's Cave
315 (Gibraltar) (Mattey et al., 2016; Mattey et al., 2010) and numerous caves in Central Texas
316 (Banner et al., 2007; Breecker et al., 2012; Cowan et al., 2013; Wong et al., 2011). These
317 effects are discussed in detail below (Section 3).

318

319 **3. Issues inherent to speleothem-based high-resolution climate reconstructions**

320 Detecting any seasonal component in a stalagmite climate signal includes quantifying growth
321 rate and input signal seasonality. It is worth noting that the input signal is sometimes
322 unexpected, and a thorough site monitoring scheme can help identify the main contributing
323 factors. For example, although many trace element ratios (and particularly Mg/Ca) are

324 affected by recharge (often via prior calcite precipitation (PCP) mechanisms (Fairchild and
325 Treble, 2009)), other factors can also influence (seasonal) stalagmite geochemistry. This is the
326 case at ATM Cave, Belize, where various trace element/calcium ratios (including Mg/Ca)
327 increase in concentration at the beginning of the annual rainy season, and are probably linked
328 to dry deposition during the preceding dry season followed by transport to the stalagmite
329 with the onset of the rainy season (Jamieson et al., 2015). In other cases, the advection of
330 atmospheric aerosols directly into the cave can affect the stalagmite trace element signal
331 (Dredge et al., 2013). Seasonal non-deposition caused by either drying of the feeder drip or
332 by seasonally high cave air $p\text{CO}_2$ can bias any record where every data point integrates more
333 than a few months of deposition. From this perspective, most stalagmite records include
334 palaeoseasonality information to some extent, but, without appropriate monitoring
335 strategies in place, deconvolving the extent to which the shifting seasonal signal dominates
336 the overall record is difficult.

337

338 **3.1. Mixing within the aquifer**

339 The degree of recharge mixing within the aquifer and epikarst is a fundamental control on the
340 preservation of a seasonality signal within stalagmites. A long residence time and/or thorough
341 mixing within the overlying aquifer can greatly attenuate any hydrological seasonal signal,
342 and understanding the hydrology feeding a cave drip is therefore critical (Atkinson, 1977;
343 Ayalon et al., 1998; Baker et al., 1997; Baker and Brunson, 2003; Baker et al., 2019; Kaufman
344 et al., 2003). For conservation and logistical reasons, monitoring and classification of the drip
345 should ideally occur prior to sampling a stalagmite.

346 Smart and Friedrich (1987) undertook one of the earliest efforts to comprehensively
347 categorise cave drips. Their scheme involved measuring drip rates at G.B. Cave, in the Mendip
348 Hills, UK, and parameterising them by plotting maximum drip rate versus the coefficient of
349 variation (C.V.; the standard deviation divided by the mean multiplied by 100). Baker et al.
350 (1997) later modified the scheme, dividing drips into six categories (seepage flow, seasonal
351 drip, percolation stream, shaft flow, vadose flow, subcutaneous flow). Other classification
352 schemes (e.g., Arbel et al., 2010; Arbel et al., 2008) focussed on analysing drip hydrographs,
353 and suggested terminology such as 'post-storm', 'seasonal', 'perennial', and 'overflow', which
354 are broadly consistent with the categories introduced by Smart and Friedrich (1987). The
355 introduction of automated drip loggers revolutionised the field (Mattey and Collister, 2008),
356 partly by ensuring that short-lived hydrological events were not missed. This ensured a
357 substantially more robust characterisation of drips than that possible via manually measuring
358 drip rates only during on-site visits.

359 Understanding the hydrology feeding a stalagmite is fundamental for determining if a
360 stalagmite retains a seasonal signal. Drip rate is controlled by surface processes (e.g.,
361 meteoric precipitation, evaporation, soil moisture capacity, and susceptibility to runoff) and
362 aquifer characteristics including reservoir capacity and bedrock permeability (Markowska et
363 al., 2015; Treble et al., 2013). Bedrock pathways recharging a drip are broadly divisible into
364 diffuse (or 'matrix'), fracture, and conduit flows (Ayalon et al., 1998; Baker et al., 1997; Perrin
365 et al., 2003; Smart and Friedrich, 1987), and recent models suggest that many drips are a
366 combination of diffuse and fracture flow. Diffuse permeability typically refers to either the
367 primary intra-granular bedrock permeability or to secondary permeability along fine
368 fractures, and is characterised by a slow response to precipitation events and a large reservoir
369 capacity (Atkinson, 1977; Smart and Friedrich, 1987). Fracture permeability relates to

370 potentially solution-enlarged bedding plane partings and joints and is characterised by a rapid
371 to intermediate response to precipitation events, and a low to moderate storage capacity.
372 Conduit permeability refers to often solutionally-enlarged pipe-like openings >1 cm in
373 diameter (Atkinson, 1977; Smart and Friedrich, 1987). Such conduit flow is characterised by a
374 rapid response to storm events followed by a rapid return to baseline flow (Baldini et al.,
375 2006), and often carries chemically aggressive waters that do not allow secondary carbonate
376 deposition. Large conduits or bedding planes may intersect a network of more diffuse
377 hydrological pathways, leading to dual-component flow where the fracture is itself fed by
378 some diffuse recharge in addition to the fracture flow. The hydrologic permeability of the
379 fracture flow component compared to the diffuse flow component essentially defines the drip
380 type; 100% diffuse flow would exhibit no response to storm events, whereas 100% fracture
381 flow would usually have no drip except for immediately following storm events large enough
382 to activate the pathway (Figure 2). Most drips would fall along the spectrum between these
383 two endmembers; a constant base drip (the diffuse flow component) combined with a
384 variably rapid response to storm events (the fracture flow component).

385 From a seasonality perspective, pure fracture-flow drips vary considerably seasonally but may
386 experience occasional dripwater undersaturation and/or drying, and consequently the
387 resultant stalagmite could have abundant 'crypto-hiatuses' (hiatuses in growth too brief to
388 leave a clear petrographic expression, or appear in chronological models (Stoll et al., 2015),
389 also referred to as 'microhiatuses' (Baker et al., 2014; Moseley et al., 2015)). We suggest that
390 if these hiatuses are demonstrably seasonally, 'seasonal hiatus' is appropriate terminology.
391 Drips characterised by 100% diffuse flow would be stable with little hydrological or biological
392 seasonality. Although the likelihood for seasonal hiatuses or drying is low for stalagmites fed
393 by diffuse flow, the seasonal signal is probably muted, unless at a site where the seasonal

394 signal is controlled by a forcing other than hydrological variability (see Section 2.4.). The
395 optimal hydrology for imparting seasonality onto a stalagmite is a drip fed by moderately
396 diffuse flow that is responsive to monthly-scale shifts in rainfall, but that does not have a
397 substantial fracture component to transmit event-scale (and possibly undersaturated) water.

398

399 **3.2. Non-deposition and seasonal bias in samples**

400 Although growth hiatuses lasting longer than a few years are often (but not always) apparent
401 within stalagmites as horizons of detrital material followed by competitive growth of
402 carbonate crystals (Broughton, 1983), brief growth hiatuses occurring seasonally are often
403 undetectable (though occasionally they have a petrographic manifestation). Thus, the
404 existence of these seasonal hiatuses is often inferred by applying monitoring data to isolate
405 intervals through the year where environmental conditions suggest temporary non-
406 deposition could exist. Because drip rate is one of the fundamental controls on stalagmite
407 growth (Genty et al., 2001), the use of drip loggers to detect seasonal drying of the stalagmite
408 feeder drip is important for understanding whether a stalagmite record excludes a certain
409 season's climate information.

410 Additionally, careful examination of sample petrography can reveal important insights into
411 the nature of the climate signal retained by a stalagmite. Petrographic microscopy helps in
412 identifying growth interruptions caused by lack of water, and dissolution features caused by
413 undersaturated dripwater. An excellent example of this approach exists for Holocene
414 stalagmites from northern Spain (Railsback et al., 2011; Railsback et al., 2017); the analysis
415 reveals horizons of dissolution (termed Type 'E' surfaces), interpreted as reflecting occasional

416 undersaturation of the feeder drip. Other examples of careful petrographic analysis informing
417 seasonality studies are provided from Drotsky's Cave, Botswana, where the alternating wet
418 and dry seasons are manifested by alternating calcite and aragonite (respectively) laminae
419 (Railsback et al., 1994) and from Grotta di Carburangeli, Italy, where columnar fabrics were
420 interpreted as reflected pronounced seasonal drip rate variability (Frisia, 2015).

421 Cave air carbon dioxide concentrations ($p\text{CO}_2$) are inversely linked to stalagmite growth rate
422 (Banner et al., 2007; Sherwin and Baldini, 2011). For example, in a study of three caves across
423 Texas, it was observed that farmed calcite growth rate was inversely correlated with cave air
424 $p\text{CO}_2$ (Banner et al., 2007). Negligible calcite growth and even seasonal hiatuses occurred
425 during the warmest summer months, when cave air $p\text{CO}_2$ increased due to low cave
426 ventilation rates (Banner et al., 2007). Elevated cave air $p\text{CO}_2$ discourages the dripwater's
427 thermodynamic tendency to degas CO_2 , thereby slowing the carbonate precipitation rate. In
428 most caves where the entrance is located above the rest of the cave, outside air with low
429 $p\text{CO}_2$ advects into the cave when the outside air density becomes greater than the cave air
430 density (e.g., Spötl et al., 2005). This is usually driven by temperature gradients; colder, denser
431 air moves down into a cave during winter, lowering the cave air $p\text{CO}_2$ and encouraging
432 stalagmite growth (James et al., 2015). However, cave air $p\text{CO}_2$ does not act in isolation, but
433 instead the critical growth determining variable is the differential between cave air $p\text{CO}_2$ and
434 dissolved CO_2 in dripwater (Baldini et al., 2008). Carbonate deposition thus could increase in
435 the high cave air $p\text{CO}_2$ season if the dripwater had equilibrated with an atmosphere with even
436 greater seasonal dissolved CO_2 increases (e.g., stemming from seasonal soil bioproductivity
437 increases) which exceed those of the cave atmosphere. These types of drips are generally
438 quite responsive to rain events, so determining if a seasonal growth bias exists should

439 incorporate both hydrology and cave atmospheric chemistry. Drips with stable drip rates, that
440 are not responsive to storm events may have more constant dissolved CO₂ and therefore
441 seasonal deposition rates that are affected exclusively by cave air pCO₂ dynamics. However,
442 several recent publications suggest that dripwater equilibrates not only with soil air, but also
443 with a reservoir of carbon dioxide within the unsaturated zone of aquifers (termed 'ground
444 air') that may have very high pCO₂ values (2 to 7%), much higher than typical soils (0.1 to 2%)
445 (Baldini et al., 2018; Bergel et al., 2017; Markowska et al., 2019; Matthey et al., 2016; Noronha
446 et al., 2015). Thus, it is possible that drip dissolved CO₂ is often near-constant, having
447 equilibrated with a ground air reservoir of near-constant pCO₂, and that carbonate
448 precipitation is anticorrelated with cave air pCO₂ regardless of drip type, although this
449 requires further research. The complexities of cave atmospheres are now reasonably well
450 understood, but more long datasets describing the dissolved CO₂ of cave drips are essential
451 for determining the variability of cave percolation waters.

452 Although a temperate-zone (Peel et al., 2007) cave's tendency to ventilate during the winter
453 is generally predictable from seasonality in external temperature (James et al., 2015),
454 occasionally cave geometry provides a more dominant control. In New St. Michael's Cave in
455 Gibraltar, ventilation is driven by seasonal changes in wind speed and direction (Matthey et al.,
456 2016; Matthey et al., 2009). The cave experiences the lowest cave air pCO₂ values in summer,
457 and consequently growth (assuming constant drip rate) is biased towards summer (Baker et
458 al., 2014). The cave's position high within the Rock of Gibraltar contributes to strong winds
459 and unusual seasonal ventilation, illustrating how cave position or geometry can dominate
460 seasonal ventilation patterns. Other examples include Bunker Cave in Germany, where an
461 essentially horizontal plan with little altitude difference between entrances produces very

462 little seasonal variability in $p\text{CO}_2$ (e.g., Riechelmann et al., 2011; Riechelmann et al., 2019),
463 and Císařská Cave (Czech Republic) where a U-shaped cave produces nonlinearities between
464 air temperature, density, and ventilation (Faimon and Lang, 2013).

465 Because seasonal hiatuses can lack either a petrological or a geochemical manifestation, cave
466 monitoring is critical for assessing the likelihood of seasonal non-deposition (Shen et al.,
467 2013). Stalagmite growth rate modelling, informed by cave monitoring data, can provide
468 invaluable information regarding how seasonal growth variability affects geochemical climate
469 proxy records integrating more than one year's worth of growth. For example, seasonal non-
470 deposition during summer due to either high evapotranspiration-induced drip cessation or
471 elevated cave air $p\text{CO}_2$ might bias lower resolution records towards wintertime rainfall values
472 (generally towards lower $\delta^{18}\text{O}$ values) (e.g., James et al., 2015) at sites where drip water is not
473 well mixed. Stoll et al. (2012) used an inverse model to illustrate that rainfall seasonality shifts
474 relative to the cave air $p\text{CO}_2$ can greatly affect PCP and consequently stalagmite trace element
475 concentrations. Baldini et al. (2008) used theoretical stalagmite growth rate equations and
476 theory developed previously (Buhmann and Dreybrodt, 1985; Dreybrodt, 1980, 1988, 1999),
477 coupled with monitoring information, to model stalagmite $\delta^{18}\text{O}$ for various drips within Crag
478 Cave (Ireland). The results suggest that the amount of time integrated by the analyses, the
479 nature of the drip, and the ventilation dynamics of the cave, all strongly modulate carbonate
480 $\delta^{18}\text{O}$ signals.

481 These studies all highlight how characterising the surface and depositional environment is
482 critical for interpreting the climate signal. Either seasonal hiatuses or reduced growth may
483 bias annual- (or coarser-) scale geochemical records towards particular seasons. Additionally,
484 it is also important to consider how regional climate shifts may have affected a sample in the

485 past, because modern processes may not have applied throughout the record. Understanding
486 climate signal emplacement processes within stalagmite carbonate is therefore fundamental
487 for building robust climate records.

488

489 **3.3. A drip classification scheme to quantify seasonal responsiveness**

490 Existing drip classification schemes are not designed to characterise the likelihood that a
491 sampled stalagmite retains a hydrologically induced seasonal signal. However, such
492 knowledge is crucial if research goals include a component of seasonal climate reconstruction.
493 Here, we introduce a new drip categorisation scheme that not only permits the identification
494 of stalagmites most likely to retain a hydrology-modulated seasonal climate signal, but that
495 also helps predict the general nature of the climate signal within any sample. This is important
496 for both the accurate interpretation of stalagmite palaeoclimate records, but also for cave
497 conservation (i.e., to maximise the usefulness of collected samples for the purpose of the
498 research goals) and for the appropriate usage of research-related resources. A seasonal-
499 resolution stable isotope record of any length requires considerable resources, and we hope
500 that this new drip classification scheme will help direct these resources to appropriate
501 stalagmite samples.

502 The scheme's essence is the collection of (ideally) at least one year of hourly drip rate data
503 for a drip feeding a stalagmite of interest. For every month, the minimum and maximum
504 hourly drip rate values are extracted. When plotted, these data reveal the extent to which
505 the drip is affected by seasonal activation of fracture permeability, and what proportion of
506 the drip consists of diffuse 'baseflow' (and whether this varies through the year). Drip
507 categorisation then involves evaluating the distribution of the datapoints, and is described

508 with terminology broadly consistent with the Smart and Friedrich (1987) scheme. Because the
509 classification scheme uses multiple data points per site, a very large number of possible
510 combinations of descriptors are possible. For example, some drip sites (e.g., drip site YOK-LD
511 within Yok Balum Cave, Belize; (Ridley et al., 2015a)) are fed by a slow diffuse flow most of
512 the year, where the minimum and maximum monthly drip rates are almost identical (Figure
513 3). However, during wetter months an overflow route is activated, and the maximum drip
514 rate increases substantially, whereas the minimum remains the same; this would be
515 characterised as a diffuse drip with a seasonally active overflow component. If this overflow
516 component is saturated with respect to calcite or aragonite, some seasonal signal may be
517 preserved, but if the overflow water is undersaturated a stalagmite fed by this drip type has
518 less potential for seasonal climate reconstructions. Similarly, drip YOK-SK is characterised by
519 almost entirely invariant diffuse recharge and would not record seasonal changes in recharge
520 (Figure 3). At Leamington Cave (Bermuda), drip BER-drip #5 is fed by diffuse recharge during
521 drier intervals of the year, but during wetter months more water is routed to the diffuse flow,
522 increasing the base flow (Walczak, 2016). Consequently, the drip does experience some
523 seasonality without risk of undersaturation, and thus a stalagmite fed by it should retain
524 hydrology-induced seasonality.

525 In this new drip classification plot, drips that are expected to produce stalagmites that retain
526 the clearest seasonal signal are those that plot with a slope approaching unity. In other words,
527 those that are not fed by either an extremely diffuse drip or an extremely flashy drip, and that
528 consequently respond to seasonal rainfall shifts without transient extreme rapid drip rate
529 episodes caused by individual storm events (which may lead to dripwater undersaturation
530 and signal loss). The two drip sites plotted in Figure 3 that best display this type of behaviour
531 (drips YOK-G and BER-drip #5) have both yielded stalagmites retaining exceptional seasonal

532 signals, stalagmites YOK-G (Ridley et al., 2015b) and BER-SWI-13 (Walczak, 2016). Other drip
533 sites that have a slope approaching unity and have a pronounced difference between the
534 highest and the lowest set of drip rates (Figure 3B) should also produce stalagmites with well-
535 developed records of seasonality.

536 Importantly, this drip classification scheme equally helps to identify drips that are unlikely to
537 produce good seasonality records. For example, stalagmites fed by drips that are invariant
538 throughout the year would not record hydrologically-induced seasonality (although a
539 seasonal signal might still be preserved based on non-hydrological factors – see Section 2.4).
540 Stalagmites fed by drips that have one or more monthly values plotting at the origin (i.e., no
541 drips for an entire month, Figure 3D) would contain seasonal hiatuses and would
542 consequently not record that interval's climate information. Drips where the diffuse flow
543 component (i.e., the monthly minimum flow) remains constant but the fracture flow
544 component (i.e., the monthly maximum flow) changes considerably (Figure 3C) may
545 experience undersaturation and either non-deposition or even corrosion of the stalagmite.

546 This classification scheme comes with some caveats. First, as discussed in Section 2.4., it is
547 possible that the seasonality signal is imparted onto the stalagmite independent of hydrology.
548 For example, if seasonal cave ventilation controls the seasonality signal, the application of the
549 scheme would differ. At a site with strong seasonal ventilation, a stalagmite deposited by a
550 purely diffuse flow-fed drip would reflect a largely cave atmospheric seasonality signal (i.e.,
551 with no hydrological seasonality). This would reduce the complexity of the geochemical signal
552 and obviate the need to deconvolve hydrological- and cave atmosphere-induced seasonality
553 from any geochemical record produced. Second, some drips are so-called 'underflow' drip
554 sites, which respond to recharge linearly up until a maximum drip rate and then become

555 unresponsive to further recharge increases. This is often caused by a constriction in the flow
556 pathway leading to the water egress point into the cave. Despite the lack of variability at high
557 flow, the dripwater is still in dynamic equilibrium with recharge (unlike high residence time
558 diffuse flow fed sites) and the stalagmite may reflect the dripwater isotopic variability.
559 Similarly, some drips are affected by piston flow, whereby an increase in hydrologic head
560 might push through a slug of older water, leading to an instantaneous response to recharge
561 but of water with a signature of 'old' water; careful monitoring can identify and mitigate these
562 issues (see Section 3.4). Despite these caveats, this drip evaluation scheme will hopefully
563 provide an efficient means for identifying actively growing stalagmite samples most likely to
564 record a seasonal climate signal prior to collection of that sample.

565

566 **3.4. Dripwater oxygen isotope seasonality**

567 The extent that cave dripwater $\delta^{18}\text{O}$ ($\delta^{18}\text{O}_{\text{dw}}$) values reflect the $\delta^{18}\text{O}$ of meteoric precipitation
568 ($\delta^{18}\text{O}_{\text{p}}$) is critical to climate studies and for understanding the palaeoseasonality signal in
569 particular. Many publications have investigated the relationship between $\delta^{18}\text{O}_{\text{p}}$ and $\delta^{18}\text{O}_{\text{dw}}$
570 (Ayalon et al., 1998; Baker et al., 2019; Baldini et al., 2015; Bar-Matthews et al., 1996; Cruz Jr.
571 et al., 2005; Duan et al., 2016; Feng et al., 2014; Harmon, 1979; Luo et al., 2014; Markowska
572 et al., 2016; Mischel et al., 2015; Moquet et al., 2016; Moreno et al., 2014; Oster et al., 2012;
573 Pu et al., 2016; Riechelmann et al., 2011; Riechelmann et al., 2017; Surić et al., 2017; Tadros
574 et al., 2016; Tremaine et al., 2011; Verheyden et al., 2008; Wu et al., 2014; Yonge et al., 1985;
575 Zeng et al., 2015). Depending on the drip site's hydrological characteristics (Arbel et al., 2010;
576 Baker and Brunsdon, 2003; Smart and Friedrich, 1987), $\delta^{18}\text{O}_{\text{dw}}$ values may reflect $\delta^{18}\text{O}_{\text{p}}$ on
577 timescales ranging from the annual weighted mean (Baker et al., 2019; Cabellero et al., 1996;

578 Chapman et al., 1992; Yonge et al., 1985) to individual (intense) recharge events (Atkinson et
579 al., 1985; Frappier et al., 2007; Harmon, 1979).

580 Factors such as depth below surface, residence time and mixing of the water within the
581 unsaturated zone, soil depth and texture, and aquifer hydraulics can vary between drip sites.
582 Important reservoirs for storage and mixing of effective rainfall are documented as the soil
583 and epikarst zones (Cabellero et al., 1996; Chapman et al., 1992; Gazis and Feng, 2004; Perrin
584 et al., 2003; Yonge et al., 1985). Rainwater infiltrating into the soil reservoir is variably lost to
585 evapotranspiration but in karst regions preferential recharge through dolines and grikes may
586 occasionally circumvent the soil and related evapotranspiration (e.g., Hess and White, 1989).
587 Dripwater $\delta^{18}\text{O}$ and δD values plotted relative to the local meteoric water line can detect
588 secondary evaporation from infiltrating water (Ayalon et al., 1998; Breitenbach et al., 2015).
589 Bar-Matthews et al. (1996) observed a 1.5 ‰ $\delta^{18}\text{O}_{\text{dw}}$ enrichment relative to rainwater and
590 attributed this primarily to seasonal evaporation in the soil and epikarst zones above their
591 Israeli cave site. Evaporative enrichment of infiltrating rainwater is greater in arid and
592 semiarid regions than in temperate regions where conditions of water excess occur through
593 much of the year (Markowska et al., 2016; McDermott, 2004). Any excess, non-
594 evapotranspired water is then transmitted to the epikarst, karst, and finally the cave.
595 Dripwater residence times in the aquifer or epikarst are highly variable, ranging from minutes
596 to years, depending on soil thickness, hydraulic properties (Gazis and Feng, 2004), and drip
597 pathway (e.g., diffuse vs. conduit flow) (Baldini et al., 2006). Mixing of infiltrating rainwater
598 with existing epikarst water can buffer the climate signal and reduce seasonal $\delta^{18}\text{O}_{\text{dw}}$
599 variability from muted to invariant (within analytical error, and assuming no cave
600 atmosphere-induced seasonality) (Baker et al., 2019; Breitenbach et al., 2019; Onac et al.,

601 2008; Schwarz et al., 2009). At some cave sites, $\delta^{18}\text{O}_{\text{dw}}$ does not necessarily correlate with
602 $\delta^{18}\text{O}_{\text{p}}$ shifts, most likely due to mixing within the aquifer (Moquet et al., 2016), underscoring
603 that different hydrologies produce stalagmites retaining different environmental signals.

604 A recent global compilation of available dripwater monitoring data has further clarified the
605 relationship between climate (e.g., mean annual temperature and annual precipitation) and
606 $\delta^{18}\text{O}_{\text{dw}}$ (Baker et al., 2019). In cooler regions where mean annual temperature (MAT) < 10°C,
607 $\delta^{18}\text{O}_{\text{dw}}$ most closely reflects the amount-weighted $\delta^{18}\text{O}_{\text{p}}$ (i.e., evaporation from the soil and
608 epikarst does not exert much influence). In seasonal climates with MAT between 10°C and
609 16°C, $\delta^{18}\text{O}_{\text{dw}}$ values generally reflect the recharge-weighted $\delta^{18}\text{O}_{\text{p}}$ (see Fig. 1 of (Baker et al.,
610 2019)). In regions where MAT > 16°C, $\delta^{18}\text{O}_{\text{dw}}$ is generally higher relative to amount-
611 weighted precipitation $\delta^{18}\text{O}_{\text{p}}$ because fractionation processes related to evaporative effects
612 on stored karst water are more substantial (Baker et al., 2019). Stalagmite $\delta^{18}\text{O}$ records
613 from regions experiencing high temperatures and/or aridity will probably not reflect rainfall
614 $\delta^{18}\text{O}$ (Baker et al., 2019).

615

616 **3.5. The uniqueness of each stalagmite record**

617 Recent publications have made a case for the importance of replication in stalagmite
618 geochemical records (Wong and Breecker, 2015; Zeng et al., 2015), which is a worthwhile and
619 useful goal. Producing the same geochemical record from multiple samples ensures that no
620 analytical issues exist and can facilitate correlating records whose growth intervals overlap in
621 regions and for time periods with high signal-to-noise ratios. Particularly in cases where
622 evidence for a short-lived climate anomaly exists, replication from within the same sample

623 and from other stalagmites is critical. However, stalagmite geochemistry is affected by a
624 myriad of variables, and the precise combination of factors affecting any one sample are
625 essentially unique. Thus, every stalagmite retains a different component of the environmental
626 signal, and a lack of reproducibility does not necessarily indicate that a record is 'incorrect' or
627 flawed. Even stalagmites that are affected by strong kinetic effects retain accurate
628 environmental data; it is a matter of recognising this control and basing any interpretations
629 accordingly.

630 Unless two stalagmites are fed by a very similar drip type (often two samples growing near
631 each other whose feeder drips share the same hydrological pathway), stalagmite records
632 from the same cave may not match. This is a clear consequence of the diversity of possible
633 drip pathways feeding individual stalagmites. For example, a stalagmite growing underneath
634 a diffuse drip fed by an extremely low hydrologic permeability pathway that is unresponsive
635 to large rain events would not contain the same record as a stalagmite growing underneath a
636 drip with no diffuse component but that is instead fed by fracture flow. The former (diffuse
637 flow-fed) stalagmite may retain long-term climate information but lack seasonal-scale
638 information, whereas the latter (fracture flow-fed) stalagmite may retain some seasonal
639 environmental information but may also experience occasional undersaturation following
640 large rain events, leading to hiatuses and information loss. The fracture flow-fed stalagmite
641 may have a more rapid overall growth rate but may experience flow re-routing and stochastic
642 drip variability due to solutional enlargement of the fracture pathway, potentially leading to
643 a shorter overall growth interval due to the eventual diversion of water away from the
644 stalagmite. Once cave- and site-specific ventilation factors are considered as well, it is
645 apparent that no two stalagmites can yield precisely the same record; rather it is imperative

646 to understand the environmental conditions recorded by each individual sample. If the goal
647 is to reconstruct seasonality, it is important to understand the nature of the seasonality signal
648 for each potential sample, e.g., whether the sample is affected by hydrological seasonality or
649 cave atmospheric seasonality. In the latter case, it is then favourable to select a stalagmite
650 from a diffuse flow drip in order to simplify the extraction of the seasonal ventilation signal.

651 The considerable range of stalagmite records possible, even from the same site, is potentially
652 advantageous. The individuality of stalagmite records may yield a powerful tool for the
653 quantitative reconstruction of historically elusive environmental variables. For example,
654 differences in oxygen isotope ratios between two samples from the same site could reflect
655 in-cave temperature-induced kinetic fractionation effects, and modelling (Deininger and
656 Scholz, 2019; Deininger et al., 2016; Dreybrodt, 1988; Dreybrodt and Deininger, 2014;
657 Riechelmann et al., 2013) could theoretically yield the cave temperature, potentially even at
658 a seasonal resolution. This perspective is consistent with the recent appreciation that
659 speleothems deposited at isotopic equilibrium are extremely rare (Daëron et al., 2019;
660 Mickler et al., 2006) and that kinetic effects are an integral part of the environmental signal
661 retained by stalagmites (Millo et al., 2017; Sade and Halevy, 2017). The concept that kinetic
662 effects are undesirable is a vestige of early studies attempting to derive absolute
663 palaeotemperatures from stalagmite oxygen isotope ratios, in which case kinetic effects do
664 indeed interfere with the extraction of the desired signal. However, because stalagmite $\delta^{18}\text{O}$
665 values are no longer considered pure in-cave temperature proxies, kinetic effects no longer
666 present a serious issue, provided that they are considered within any interpretations. In fact,
667 because kinetic effects often vary in sync with the primary rainfall signal (e.g., kinetic effects

668 tend to occur during drier periods accentuating the already elevated stalagmite $\delta^{18}\text{O}$ and $\delta^{13}\text{C}$
669 signature) they tend to help the climate signal stand out above background noise.

670 Stalagmite climate reconstructions are usually based around one record or an overlapping
671 series of records; future research could use the differences between two records (considering
672 in-cave kinetic effects) to reconstruct aspects of the environmental signal, including seasonal
673 temperature shifts. Recent research utilising several stalagmites from along the same
674 moisture trajectory across a wide region to reconstruct oxygen isotope systematics and
675 temperature represent an exciting development in speleothem climate sciences (Deininger
676 et al., 2017; Hu et al., 2008; McDermott et al., 2011; Wang et al., 2017), and similar
677 methodologies could reveal in-cave fractionation processes that are ultimately relatable to
678 temperature, potentially on a seasonal-scale. For example, changes in outside temperature-
679 induced ventilation may affect samples fed by different hydrologies differently (promoting
680 more kinetic fractionation in slower dripping sample), and comparing the isotope ratio
681 records may reveal the range of external seasonal temperature variability. We suggest that
682 the comparison of multiple coeval stalagmite geochemical records from within the same cave
683 site is a crucial research frontier that is well worth investigating further.

684

685 **4. Analytical techniques**

686 Direct detection of seasonal variations in stalagmite geochemical parameters requires
687 sampling or analysis at sufficiently high spatial resolution to mitigate signal averaging (Figure
688 4). Sampling frequency should approach monthly resolution to detect a seasonality signal and
689 to avoid aliasing issues during intervals with slower growth. This necessitates careful

690 consideration prior to analysis to ensure both sufficient sampling resolution to detect
691 seasonal-scale variability, and sufficient material for the analytical method. In addition to the
692 pre-analysis considerations, we also recommend publishing complete micro-analytical data
693 tables, in order to increase transparency. Below we discuss common microanalytical
694 techniques capable of palaeoseasonality reconstruction and compare advantages and
695 disadvantages of each.

696

697 **4.1. Sampling for palaeoseasonality**

698 Sub-sampling stalagmites for geochemical analysis requires careful planning and execution.
699 We recommend a thorough reconnaissance of a sample's petrography using microscopy prior
700 to geochemical analysis. The conversion of a sample into polished thin sections can provide
701 critical information but is destructive. Reflected light microscopy provides a non-destructive
702 alternative that can yield crucial information regarding crystal growth habit, the location of
703 possible hiatuses, inclusions, and porosity.

704 The various methods available for the extraction of proxy data all require different sample
705 amounts depending on analytical limits of detection and other factors (Fairchild et al., 2006).
706 Methods are broadly categorizable as destructive and non-destructive, depending on the
707 amount of material required. The former is further divisible into: i) macro-destructive (e.g.,
708 cuttings for fluid inclusion studies, low-concentration proxies like biomarkers or DNA) (e.g.,
709 Blyth et al., 2011; Vonhof et al., 2006; Wang et al., 2019a), ii) meso-destructive (e.g.,
710 conventional and micro-milling for U-series samples, stable isotopes, ICP-OES, ^{14}C) (e.g.,
711 Lechleitner et al., 2016a; Ridley et al., 2015b; Spötl and Matthey, 2006), and iii) micro-
712 destructive (e.g., laser ablation or secondary ionization mass spectrometer (SIMS) analyses

713 for traditional and non-traditional isotope systems, element concentrations or ratios) (Baldini
714 et al., 2002; Luetscher et al., 2015; Treble et al., 2007; Webb et al., 2014; Welte et al., 2016).
715 Non-destructive methods include (but are not restricted to): i) simple desktop scanning and
716 photography, ii) μ XRF line scanning and mapping (e.g., Breitenbach et al., 2019; Scropton et
717 al., 2018), iii) synchrotron analyses (e.g., Frisia et al., 2005; Vanghi et al., 2019; Wang et al.,
718 2019b; Wynn et al., 2014), iv) phosphor mapping via beta-scanning (e.g., Cole et al., 2003), v)
719 reflected light, and fluorescence, including confocal laser fluorescent microscopy (CLFM) (e.g.,
720 Orland et al., 2012) and other microscopy techniques (e.g. SEM, EMPA, RAMAN), or vi) X-ray
721 Computed Tomography (CT) scanning (e.g., Walczak et al., 2015; Wortham et al., 2019). The
722 choice of technique should consider suitability for answering the targeted research questions,
723 and logistical considerations such as sample sectioning. Although the list above categorises
724 techniques based on their destructiveness, it does not account for sample preparation; for
725 example, SIMS analysis uses only a small amount of sample (i.e., essentially non-destructive),
726 but requires sectioning of the stalagmite into centimetre-scale cubes, polishing and epoxy-
727 mounting. Another major consideration is the length of the record required; it is possible
728 (though labour-intensive) to produce seasonal-scale records extending hundreds or even
729 thousands of years using micromilling, but this is not practical using SIMS, unless automated
730 protocols allowing for unattended analysis can be developed.

731 Although macro-destructive sampling can inform interpretations based on higher resolution
732 data, it cannot generally reconstruct seasonality on its own. Thus, here we discuss only
733 selected meso-, micro-, and non-destructive techniques. The focus is first on 'conventional
734 drilling' and 'micromilling' of powder samples, which probably are the most widely used
735 techniques to obtain material for inorganic chemistry, followed by the highly versatile, fast,
736 and cost-effective laser ablation sampling (LA-ICPMS). SIMS requires substantial sample

737 preparation, offers excellent resolution and is a good choice in situations requiring in-depth
738 characterisation of a short interval. Synchrotron- μ XRF (SR- μ XRF) has advanced considerably
739 over the past decade, and it is now possible to obtain high-resolution (0.5-5 μ m) quantitative
740 trace element data non-destructively through fast scanning of large samples (Borsato et al.,
741 2019). Below we describe the relevance and applicability of these techniques towards the
742 reconstruction of palaeoseasonality.

743

744 **4.1.1. Conventional drilling**

745 Conventional drilling (or 'spot-sampling') (Fairchild et al., 2006) is the drilling of powders from
746 discrete spots that are normally separated by unsampled material, and is still amongst the
747 most widely used methods to obtain carbonate powders from speleothems. This method is
748 comparably fast and, with a sufficiently small drill bit (typical \varnothing ca. 0.2-1 mm), can achieve a
749 spatial resolution of up to 0.3-0.5 mm along the growth axis, although more frequently the
750 resolution is \sim 1 mm. Conventional drilling is ideally performed with instruments that allow
751 computer-aided control of x-y-z dimensions, such as Sherline[®] or Mercantek[®] instruments.

752 With typical stalagmite growth rates of 0.1 to 0.2 mm year⁻¹, this technique is usually
753 inadequate when targeting sub-annual resolution (Figure 5). If used on samples with growth
754 rates approaching twice the sampling interval, aliasing may occur and unfavourably affect the
755 recovery of high-frequency variability (Fairchild et al., 2006). Furthermore, this type of spot
756 sampling usually does not integrate all the carbonate material, i.e. the time slices at the top
757 and bottom of the hole are under-represented in the average for the drill-hole; this
758 undersampling could miss short-lived climate excursions. Consequently, we cannot
759 recommend conventional drilling for recovering a seasonal signal, although the technique is

760 effective at quickly producing a lower-resolution record and is well suited for longer records
761 of climate (e.g., those covering multiple glacial cycles), and for screening potential target
762 stalagmites. Additionally, conventional drilling is possible on a large stalagmite slab, obviating
763 the need for sectioning into multiple smaller slabs. A related technique which is preferred for
764 sampling at seasonal scale is micromilling, discussed below.

765

766 **4.1.2. Micromilling**

767 Micromilling refers to continuous sample cutting along a trench parallel to a stalagmite's
768 growth axis (Fairchild et al., 2006; Frappier et al., 2002; Spötl and Matthey, 2006). Usually
769 performed with computer-controlled milling devices (such as the ESI/New Wave micromill)
770 this technique can achieve ~10-micron spatial resolution e.g. Ridley et al., 2015b, but is
771 critically dependent on the textural characteristics of the sample. Dense columnar, fascicular,
772 radiaxial, or radial fibrous calcites are the most suitable material, but needle-like aragonite
773 can also be sampled, although gaps between needle-shaped crystals may lead to loss of
774 sample and require painstaking cleaning procedures. The sample morphology throughout the
775 stalagmite also warrants consideration. Planar, parallel, and laterally continuous laminae
776 across the sample are ideal, but often stalagmite laminae appear curved in a slabbed sample.
777 These are normally convex, but in some cases are concave (particularly in the case of a 'splash'
778 cup), and with laminae that thin towards the edges. The greater such curvature, the narrower
779 the micromilling trough required for sub-annual (seasonal-scale) sampling (Figure 5), because
780 a wider trench would integrate material from other laminae. Similarly, the sample should
781 allow 2-3 mm sampling into the depth of the sample slab, and ideally the growth layers should
782 not taper out in the third dimension. X-ray and Neutron CT scans can help visualise the 3D

783 internal structure of the sample (Walczak et al., 2015; Wortham et al., 2019), and the
784 appropriate milling depth.

785 The determination of the x, y, and z dimensions of the sampling increment is the first step of
786 any sampling strategy (Figure 5). For seasonal resolution, this strategy will ideally permit a
787 very small y-axis increment (the y-axis is parallel to the stalagmite growth axis). The other
788 dimensions must then allow the collection of enough carbonate for analysis (typically 50-120
789 μg for carbon and oxygen stable isotopes). Depending on sample characteristics and desired
790 resolution, dimensions of $y = 10\text{-}100 \mu\text{m}$ and $x = 10\text{-}300 * y \mu\text{m}$ (parallel to growth layers on
791 the slab) are ideal (Figure 5). The sampling depth (z-axis) is best minimised because lamina
792 behaviour into the sample is often unknown, unless CT scans of the sample exist. Larger
793 sample masses are occasionally needed for non-traditional proxies.

794 A common issue in the speleothem sciences is the precise correlation between two datasets
795 obtained via different means, for example a micromilled stable isotope dataset and a LA-
796 ICPMS derived trace element dataset. Annual- to decadal-scale correlations are usually
797 possible, but rarely are the records correlative on the seasonal- or even annual-scale.
798 Comparisons are achievable using very careful measurements from a datum (often the
799 stalagmite top), with or without the use of banding as 'landmarks' (e.g., (Johnson et al., 2006;
800 Treble et al., 2005a)). A recent technological advance is the development of software, such as
801 the open-source GIS-based QGIS software (Linzmeier et al., 2018), which integrates micro-
802 imaging and analysis into a single spatial reference frame. This approach is particularly useful
803 for organising different analyses derived from differently sectioned portions of samples and
804 has been successfully applied to stalagmite data (Orland et al., 2019).

805 The problem of correlating different types of data is to some extent avoidable by sampling
806 sufficient material with the micromill for both stable isotope and trace elemental analysis via
807 ICP-MS. The sampled powder is divided into two aliquots, one for each analytical technique.
808 The resultant trace element and stable isotope data permit zero-lag cross-correlations and
809 highly robust interpretations of different environmental processes (e.g., Jamieson et al.,
810 2016).

811 For example, if planned multi-proxy analyses require 0.8 mg of carbonate powder (e.g., stable
812 isotope ratios, ^{14}C , and trace elements), and a 50 μm spatial resolution is desired using a
813 milling bit diameter of 0.8 mm, a 0.05 mm x 4.15 mm x 1 mm trench would suffice (assuming
814 calcite density of 2.7 g/cm^3 and no sample loss via incomplete recovery); sample loss and a
815 particularly low-density sample would require a larger volume. An often-overlooked
816 additional consideration involves the corners that are initially unsampled when milling
817 trenches (red corner areas, Figure 5). Depending on the drill bit diameter and trench
818 dimensions, the corners at each end of the trench would lead to unwanted integration of
819 material from several sample increments and thus time slices. Use of a smaller milling bit
820 diameter minimizes this effect. Additionally, a 50% reduction of this sampling effect is
821 achieved if a trench is milled along the growth axis prior to the high-resolution milling, or if
822 the milled trench is adjacent to a longitudinal cut (Figure 5). Material from the first trench can
823 be used for reconnaissance studies. Another approach yielding similar results involves
824 collecting the desired powder, and then moving the milling bit along the horizontal sampling
825 track (i.e., parallel to the growth layer) for a distance corresponding to half the width of the
826 milling bit. This powder is then discarded (or collected as auxiliary powder), and the milling
827 bit returns to the original position, ready to produce the next aliquot of powder. Either of
828 these sampling approaches effectively reduce spatial integration of sample (Kennett et al.,

829 2012; Myers et al., 2015; Ridley et al., 2015b), thereby increasing the likelihood of obtaining
830 a clear seasonal signal (Figure 6). These considerations are important because many
831 stalagmites, particularly from non-tropical localities, may have low growth rates (Railsback,
832 2018) that require a very high sampling resolution with minimal integration across samples
833 to extract a seasonal signal.

834 Many samples may deviate from an idealised geometry, and may contain imperfections along
835 preferred micromilling tracks, growth rate changes, or growth axis shifts. These instances may
836 require special consideration and sample-specific solutions, such as moving to a different
837 track within the sample or changing the resolution of the analyses in response to major
838 changes in growth rate. In the case of the latter, interpretations should consider how changes
839 in sampling resolution might have affected the amplitude of any seasonal cycle.

840 Other issues include growth layers that slope inward rather than geometrically perfect layers
841 (where the layering is perpendicular to section) and the use of tapered rather than cylindrical
842 drill bits, which samples less carbonate at depth than the step size implies, and then integrates
843 this carbonate into subsequent samples. A study comparing micromilling/IRMS and SIMS
844 techniques on annually layered otoliths found that an offset existed between the two
845 techniques (with SIMS yielding values $\sim 0.5\%$ lower) and that the amplitude of annual oxygen
846 isotope signal derived via micromilling was approximately half of the SIMS signal; both of
847 these observations are potentially explained by deviations from an ideal sample geometry,
848 and consequently greater integration of unwanted material arising from micromilling (Helser
849 et al., 2018). Despite these differences, both techniques were able to detect annual isotope
850 ratio cycles (Helser et al., 2018). A thorough reconnaissance of the sample using CT scanning
851 or other means to characterise its geometry in advance of slabbing can minimise these issues.

852 Other minor issues include the possible conversion of aragonite to calcite during milling,
853 which would result in a decrease in $\delta^{18}\text{O}$ values of 0.02‰ for every 1% aragonite converted
854 to calcite (Waite and Swart, 2015). This effect may have implications for modelling oxygen
855 isotope variability or calculating deviations from equilibrium deposition. However, using a
856 slower rotation rate of the milling bit (500-800 rpm) will minimise, or even eliminate, this
857 effect. A final recommendation is to run micromilled samples through the IRMS non-
858 sequentially (i.e., out of stratigraphic order). Ideally the laboratory environment is static and
859 will not affect results, but any unaccounted for changes (e.g., lab temperature) may affect the
860 analyses in a cyclical way. Running samples non-sequentially both helps ensure that any cycles
861 detected (e.g., a seasonal cycle) are not analytical artefacts and helps to identify issues, if they
862 exist (e.g., a persistent cycle when samples are arranged in the order that they were run).

863

864 **4.1.3. LA-ICPMS**

865 Laser Ablation Inductively Coupled Plasma Mass Spectrometry (LA-ICPMS) is a beam method
866 sampling technique. A polished speleothem slab is analysed by ablating small portions of
867 material using a laser within a sample cell. The laser (typically an ArF excimer laser at a 193
868 nm wavelength) physically ablates the sample, aerosolising the material which is then carried
869 into the ICP-MS system by a carrier gas (typically helium and/or argon, with helium yielding a
870 greater signal intensity (Luo et al., 2018)) where trace element concentrations are measured
871 and quantified against standards of known compositions. The specific mass spectrometer set-
872 up depends on the research question; for example, by using a quadrupole ICP-MS for
873 elemental measurements using a reference isotope, or a multi-collector ICP-MS for isotope
874 ratio analyses. Additional analytical set-ups are compatible with LA-ICPMS, including reaction

875 cells, triple-quadrupoles, and split-stream analysis using two mass spectrometers in tandem
876 (Frick et al., 2016; Kylander-Clark et al., 2013; Woodhead et al., 2016).

877 The advantages of LA-ICPMS for speleothem trace element analysis are numerous and include
878 excellent spatial resolution (down to ~3 microns (Müller and Fietzke, 2016) using a
879 rectangular aperture with long axis oriented along laminae) whilst preserving low detection
880 limits (Figure 6). Although historically LA-ICPMS instruments used round 'spots', some laser
881 ablation instruments are now fitted with rectangular masks (apertures), resulting in
882 rectangular spots optimised for speleothem analysis, where the ablation spot's long
883 dimension is oriented perpendicular to speleothem growth axis, along the x-axis (Müller et
884 al., 2009). This permits the ablation of a surface area equivalent to large circular spot sizes,
885 while retaining high spatial resolution in the growth direction (similar to the micromill
886 sampling described in 4.1.2). The speed of analysis via this method is also exceptionally high,
887 with typical scan speed of $10 \mu\text{m s}^{-1}$ (e.g., (Jamieson et al., 2015)). Two-volume laser cells are
888 now available, minimising sample damage incurred via sectioning and ensuring consistent
889 aerosol flow within the cell. The coupling of a laser ablation system with a large-capacity gas
890 exchange device even allows analysis under atmospheric air (Tabersky et al., 2013) although
891 with somewhat elevated limits of detection. This technique is particularly suitable for large
892 stalagmites, or archaeological samples, because it minimises physical sample destruction by
893 requiring less sectioning.

894 The presence of a localised impurity can produce a trace elemental concentration peak even
895 in the absence of a laterally contiguous geochemical horizon with that geochemistry. LA-
896 ICPMS can produce elemental maps that can verify the spatial continuity of geochemical
897 laminae of interest, particularly when combined with a square aperture (Evans and Müller,

898 2013; Rittner and Muller, 2012; Treble et al., 2005b; Woodhead et al., 2007). This permits the
899 resolution of spatial relationships with greater confidence and can corroborate
900 interpretations based on stacked and parallel line scans, thereby avoiding issues related to
901 the overinterpretation of a small number of points. Other microanalytical techniques (e.g.,
902 SIMS, synchrotron, μ XRF, etc.) can also produce elemental maps, but LA-ICPMS techniques
903 can provide greater spatial coverage more rapidly.

904 The most significant disadvantage to LA-ICPMS is related to difficulties with standardisation.
905 The use of matrix matched standards (i.e., made of the same material as the sample) during
906 laser ablation analysis is ideal, but the limited availability, variable degrees of standard
907 homogeneity, and accurate standardisation of carbonate materials are ongoing challenges.
908 Orland et al. (2014) and later Müller et al. (2015) provide promising tests for a carbonate
909 standard, albeit for a limited range of elements. Many analyses are standardised with
910 somewhat greater uncertainty than is ideal using glasses such as NIST 620 or 622. These
911 analyses are often regarded as semi-quantitative, with high levels of confidence regarding
912 variability and data trends but uncertainty regarding absolute values. Another minor
913 disadvantage is lack of precise knowledge regarding the position of individual analytical spots.
914 The sheer number of analyses possible via this technique (often >10,000) and indistinct,
915 continuous track means that the exact position of any one individual spot is often difficult to
916 determine precisely, complicating the correlation with other climate proxies. This
917 disadvantage is mitigatable by precise notetaking, syn-analytical microscopy recording,
918 careful reflected light imaging, cross-correlation, application of QGIS or similar software, and
919 judicious 'wobble-matching' with other proxy records, as well as creating marker laser lines at
920 certain intervals to further help to constrain spatial uncertainties.

921

922 **4.1.4. Secondary ionisation mass spectrometry**

923 Secondary ionisation mass spectrometry (SIMS) uses a primary beam of positive (often
924 caesium) or negative (often oxygen) ions to impact a sample surface under a vacuum,
925 'sputtering' secondary ions into a mass spectrometer (Wiedenbeck et al., 2012). The
926 sputtered secondary ions are then accelerated into a double-focusing mass spectrometer and
927 counted by ion detectors (electron multiplier or Faraday cup). This analytical technique can
928 yield both trace element analysis and stable isotope ratio data in speleothem carbonate at
929 the micron scale, with very little damage to the sample, and with very high sensitivity (Figure
930 6).

931 The spatial resolution typically ranges between 1 to 10 μm spot size and 1-2 μm spot depth
932 for trace elements, with stable isotope analyses historically restricted to 20–30 μm resolution
933 (Fairchild and Baker, 2012) but now capable of achieving 10 μm resolution (Orland et al.,
934 2019). This represents a very high-resolution method for stable isotope analysis within
935 speleothem carbonate and is therefore ideal for detecting palaeoseasonality (Fairchild et al.,
936 2006). The analytical resolution for trace elements is lower than when using synchrotron
937 radiation, but with the added advantage of full quantification of concentration data and the
938 ability to cover much greater areas of sample. Matrix matched materials, typically calcium
939 carbonate, are used for standardisation to ensure consistent ionisation of chemical species
940 and ablation rates (Fairchild and Treble, 2009).

941 Early studies of SIMS-derived trace element trends in speleothems helped to demonstrate
942 that many stalagmites retained a seasonal signal (Baldini et al., 2002; Finch et al., 2001;

943 Roberts et al., 1998), representing a considerable shift in resolving power compared to the
944 former decadal- to centennial-scale of analysis previously possible. The presence of annual
945 trace element cycles was quickly established as the norm rather than the exception for
946 shallow cave sites, even in the absence of visible speleothem laminations (Fairchild et al.,
947 2001). Divalent alkaline earth metals such as magnesium and barium were suggested as
948 palaeohydrological proxies, phosphorus as indicative of bioproductivity, and strontium as
949 reflecting calcite growth rate and/or PCP (Fairchild et al., 2001; Fairchild et al., 2000; Treble
950 et al., 2003). However, the need for better empirical transfer functions between speleothems
951 and external climatic processes, and partitioning between drip waters and speleothem
952 calcite, complicated interpretations (Fairchild et al., 2001). Subsequent process-based studies
953 have revealed the complexity involved in interpreting trace elements at seasonal scales,
954 highlighting the role they play in complexation with organic matter as colloids (Borsato et al.,
955 2007), in speleothem diagenesis (Martin-Garcia et al., 2014), and the complex controls on
956 transfer through vegetation/soil/epikarst (Hartland et al., 2009; Hartland et al., 2012), as well
957 as controls on partitioning via internal cave microclimate and crystallographic structures
958 (Fairchild and Treble, 2009). The use of trace element cycles obtained via SIMS as
959 chronological markers is exemplified through the work of Smith et al. (2009), where the ability
960 of trace element cycles to provide relative age constraints at a finer spatial resolution than
961 traditional U-series age models is unambiguously demonstrated.

962 A frontier for SIMS trace element measurements lies in the potential of combining these trace
963 element records with stable isotope measurements undertaken at sub-annual scale. Prior to
964 the advent of SIMS techniques for stable isotope analysis, there were very few combined
965 trace element – stable isotope studies due to the incompatibility of analytical resolution

966 between the two parameters (Orland et al., 2014). However, the analysis of stable isotopes
967 by SIMS now achieves a spatial resolution capable of allowing direct comparability between
968 both isotopic and trace element indicators of seasonality (Orland et al., 2014).

969 SIMS stable isotope studies have investigated the $\delta^{18}\text{O}$, $\delta^{13}\text{C}$ and $\delta^{34}\text{S-SO}_4$ dynamics in
970 stalagmite records (typical uncertainties (2σ): $\delta^{18}\text{O} = 0.2\text{‰}$ (Orland et al., 2019); $\delta^{13}\text{C} = 0.6\text{-}$
971 0.7‰ (Oerter et al., 2016; Sliwinski et al., 2015); $\delta^{34}\text{S} = 1.6\text{‰}$ (1σ) at 70 ppm S concentrations
972 (Wynn et al., 2010)). Whereas each of these isotope ratios reflects changing surface
973 environmental conditions over inter-annual timescales, only the $\delta^{18}\text{O}$ measurements by SIMS
974 can produce records of intra-annual seasonality. Analysis of $\delta^{13}\text{C}$ in speleothem carbonate
975 cannot be undertaken simultaneously with $\delta^{18}\text{O}$, and any available records in the literature
976 (e.g., (Pacton et al., 2013)) are not undertaken at seasonal resolution. The apparent lack of
977 seasonal change in cave dripwater $\delta^{34}\text{S-SO}_4$ (Borsato et al., 2015) has also so far prevented
978 SIMS speleothem sulphur isotope measurements at the seasonal scale (Wynn et al., 2010).

979 Treble et al. (2005a) produced the first $\delta^{18}\text{O}$ record unambiguously linking seasonal cycles in
980 speleothem oxygen isotopes to rainfall dynamics and corroborated these interpretations with
981 trace element cycles and contemporary rainfall monitoring. Subsequent work at Soreq Cave
982 (Israel), further developed the technique to detect seasonality and links with rainfall dynamics
983 across a range of time periods (Orland et al., 2012; Orland et al., 2009; Orland et al., 2014).

984 Coupled annual variability in fluorescence and $\delta^{18}\text{O}$ provided a seasonal marker of annual
985 variability in rainfall from before the climate instrumental record (Orland et al., 2012; Orland
986 et al., 2009). Careful correlation between fluorescent banding, $\delta^{18}\text{O}$ and trace element
987 measurements, and surface environmental conditions demonstrated that the fluorescent
988 banding represented seasonal organic colloid flux variability into the cave.

989 Despite the clear advantages of utilising SIMS stable isotope analyses of speleothem
990 carbonate to reveal seasonal patterns of rainfall delivery and drivers of climatic change, the
991 technique also comes with its analytical challenges, including the considerable impact of
992 geometric imperfections (e.g., sample topography, porosity, inclusions, cracks, etc) (Kita et
993 al., 2011; Liu et al., 2015; Pacton et al., 2013; Treble et al., 2005a). In most instances, the
994 ability to control the precise location of SIMS analyses enable geometric imperfections to be
995 avoided, provided that i) good surface mapping can be used to identify optimal locations for
996 analysis and that ii) post-processing can visualise geometric imperfections in each analysis pit
997 (Orland et al., 2009). This contrasts with micromilling, where large swathes of sample are
998 often bulked together regardless of sample porosity or imperfections. The need to use matrix
999 matched standard materials presents similar problems of availability and homogeneity for the
1000 accuracy of data analysis as encountered with LA-ICPMS. However, recent improvements in
1001 this area, alongside improvements in sample preparation techniques have been substantial
1002 enough to enable accurate correction for instrumental drift (Valley and Kita, 2009). The
1003 impact of trace element content on carbonate $\delta^{18}\text{O}$ and $\delta^{13}\text{C}$ analyses also requires careful
1004 consideration (Sliwinski et al., 2017), but can be corrected following careful standardisation
1005 and is generally not a problem encountered through speleothem analysis where the trace
1006 element content is typically less than 1 weight %. An emerging analytical frontier concerns
1007 the impact of water and/or organic content on SIMS carbonate $\delta^{18}\text{O}$ and $\delta^{13}\text{C}$, requiring
1008 careful pre-screening of sample material and simultaneous analysis of OH- and CH-
1009 respectively (Orland et al., 2015; Orland et al., 2019; Orland, 2013; Wycech et al., 2018).

1010 Despite these issues, SIMS remains an appealing choice for palaeoseasonality reconstruction
1011 using stalagmites due to its sensitivity and resolution. SIMS has produced some of the highest

1012 resolution records of palaeoseasonality available and will continue to play an important role
1013 in linking stalagmite records to seasonal changes in environmental conditions, particularly
1014 across discrete, short-lived events. Although the technique is not suitable for building long
1015 records, the comparison of discrete timeslices permits seasonality to be contrasted for key
1016 intervals (Orland et al., 2012; Orland et al., 2015; Orland et al., 2019).

1017

1018 **4.1.5. Synchrotron**

1019 The application of Synchrotron Radiation micro X-Ray Fluorescence (SR- μ XRF) to the study of
1020 speleothem carbonate opened up new possibilities in terms of greater resolving power for
1021 geochemical analysis (Kuczumow et al., 2003; Kuczumow et al., 2001). Based on the emission
1022 of electromagnetic radiation from charged electrons accelerated in an orbit, synchrotron
1023 radiation generates secondary radiation from speleothem carbonate based on the
1024 characteristic fluorescent properties of chemical elements. The excellent spatial resolution of
1025 analysis (0.5–5 microns), low detection limits, low background, and the ability to
1026 quantitatively map trace element variability across a given area has enabled the study of
1027 speleothem geochemical structures at the sub-annual timescale and in two dimensions
1028 (Figure 6). The use of XANES (X-Ray Absorption Near Edge structure) can define the oxidation
1029 state of the element under consideration, thereby adding further resolving power to
1030 determine environmental processes.

1031 Applications range from using SR- μ XRF to determine long-term (100 year) secular changes in
1032 elemental signals (Frisia et al., 2005), high resolution event imaging across sub-annual to
1033 multi-annual timescales (Badertscher et al., 2014; Frisia et al., 2008; Vanghi et al., 2019; Wang

1034 et al., 2019b), and for investigating petrological controls on geochemical composition (Frisia
1035 et al., 2018; Ortega et al., 2005; Vanghi et al., 2019). However, it is at the seasonal scale of
1036 analysis where the resolving power of synchrotron radiation has really pushed the boundaries
1037 of speleothem science.

1038 No conventional dating technique provides an absolute timeframe at the sub-annual scale of
1039 speleothem carbonate deposition. However, linking the seasonality of external
1040 environmental processes to speleothem petrology and geochemical characteristics can yield
1041 a monthly scale resolution of trace element content. SR- μ XRF was used to determine the
1042 coincidence of trace element distributions and physical calcite characteristics within annual
1043 stalagmite laminations (Borsato et al., 2007). Based on the annually laminated stalagmite
1044 ER78 from Ernesto Cave, Italy, a suite of trace elements (P, Cu, Zn, Br, Y, and Pb) were found
1045 to form an annual peak, coincident with a characteristic thin (0.5-4 μ m) brown UV-fluorescent
1046 layer in each annual couplet. The brown colouration of each UV-fluorescent layer is probably
1047 due to organic acids derived from high rates of water infiltration during each autumn (Frisia
1048 et al., 2000; Huang et al., 2001; Orland et al., 2014). The transport of trace elements is
1049 associated with colloidal organic molecules (Hartland et al., 2010; Hartland et al., 2012), and
1050 leads to the incorporation of this distinctive elemental suite on a seasonal basis associated
1051 with the autumnal rains (the 'autumnal pulse' as described in Section 2.4). SR- μ XRF permits
1052 the detection of variability inherent to each individual year, which then can be contrasted
1053 against the symmetrical mean annual profile. Any differences (e.g., double peaks or shoulder
1054 peaks) provide an indication that the rainfall distribution throughout that year deviated from
1055 the mean annual profile. Strontium was observed to vary inversely to colloiddally transported
1056 elements (Borsato et al., 2007), possibly due to competition for binding to defect sites, thus
1057 limiting incorporation into the calcite lattice. SR- μ XRF revealed seasonal patterns of zinc, lead,

1058 phosphorus, and strontium within speleothem Obi84 from Obir Cave, Austria, whose
1059 concentration peaks also coincided with the dark coloured visible laminae. These were
1060 similarly interpreted as hydrological event markers associated with autumnal infiltration but
1061 could also result from dry deposition of aerosols (Dredge et al., 2013).

1062 SR- μ XRF 2D mapping within speleothem Obi84 over three annual cycles demonstrated the
1063 effects of several infiltration events each year, present as short-lived peaks in Zn
1064 concentration and which build in magnitude towards the main autumnal flush (Wynn et al.,
1065 2014) (Figure 6). Using these event peaks as markers of autumnal flushing permitted
1066 attribution of annual sulphate cycles to summer high and winter low concentrations. At the
1067 Obir Cave site, these seasonal shifts in speleothem sulphate content were attributed to
1068 temperature-driven cave ventilation and associated cave air $p\text{CO}_2$ variability which controlled
1069 the dripwater pH and the sulphate:carbonate ratio. Wynn et al. (2018) later verified this
1070 proposed seasonal mechanism using controlled laboratory experiments, thereby permitting
1071 the extraction of seasonal temperature information based on the annual sulphate cycle's
1072 topology. SR- μ XRF can thus extract geochemical expressions of seasonality, and the technique
1073 is well-suited to investigating changing rainfall and temperature seasonality dynamics back
1074 through time.

1075

1076 **4.1.6. Data analysis**

1077 Following the geochemical analyses and data processing, the information must be
1078 interpreted. For techniques producing tens to hundreds of data points, this is not particularly
1079 challenging. On the other hand, techniques such as LA-ICPMS can produce tens of thousands
1080 of data points for multiple elements and can greatly increase the processing time on common

1081 spreadsheet programmes. To circumvent these issues, it is possible to simplify the data using
1082 a Principal Component Analysis (PCA), a multivariate statistical analysis technique which
1083 extracts modes of variation from large multivariate timeseries datasets that best describe
1084 overall variability of those datasets. The technique is ideal for large multivariate stalagmite-
1085 derived LA-ICPMS datasets (Borsato et al., 2007; Jamieson et al., 2015; Orland et al., 2014;
1086 Wassenburg et al., 2012). PCA has also been used to extract a seasonal signal from trace
1087 elemental concentrations even in the absence of visible laminae and applied towards the
1088 development of a chronology (Ban et al., 2018).

1089 Comparing the intra-annual amplitude of a geochemical signal (Orland et al., 2012; Orland
1090 et al., 2009; Orland et al., 2014; Orland et al., 2019) from monthly-resolved datasets is ideal
1091 for extracting seasonal information from an otherwise difficult to interpret dataset. For
1092 example, Ridley et al. (2015b) used the well-developed annual carbon isotope cycles with
1093 their Belizean stalagmite to extract seasonal amplitudes, which were then interpreted in
1094 terms of the strength of the seasonal ITCZ incursion into southern Belize. Orland et al.
1095 (2015) used the topology of oxygen isotope variability within individual growth bands in a
1096 Chinese stalagmite to clarify the origin the oxygen isotope variability. Spectral analysis of
1097 well-dated samples can also reduce data complexity (Myers et al., 2015; Ronay et al., 2019).
1098 For example, Asmerom et al. (2020) used a wavelet analysis to reconstruct the strength of
1099 the wet season in Central America over the last two millennia, and to show that modern
1100 seasonality in rainfall was only emplaced in the 15th Century. Extracting a meaningful metric
1101 from numerous more complex data using statistical techniques is one way of simplifying a
1102 complex geochemical dataset.

1103

1104 **5. Modelling techniques**

1105 There have been many efforts at modelling both the hydrology feeding a stalagmite and the
1106 climate signal within. Proxy system models (PSMs) describe how geological or chemical
1107 archives are imprinted with a climate signal (Evans et al., 2013). In terms of stalagmite-specific
1108 models, several exciting geochemical models now exist which can explore the emplacement
1109 of a geochemical signal in a stalagmite (Wong and Breecker, 2015), often based on established
1110 processes which govern stalagmite precipitation (e.g., (Buhmann and Dreybrodt, 1985)). Two
1111 recent examples (specifically of disequilibrium isotope fractionation processes proxy system
1112 models) are the IsoCave model, which can examine disequilibrium isotope effects in
1113 speleothems and related implications for speleothem isotope thermometry (Guo and Zhou,
1114 2019), and the ISOLUTION model which similarly helps to better understand the effect of
1115 these disequilibrium isotope fractionation processes on stalagmite proxy records (Deininger
1116 and Scholz, 2019). The I-STAL model allows the simulation of PCP and how this affects
1117 dripwater Mg, Sr, and Ba (Stoll et al., 2012). Numerous models looking specifically at drip
1118 hydrology now exist (e.g., KarstHydroModel (Baker and Bradley, 2010; Treble et al., 2003)),
1119 and these are extremely useful for understanding how the rainfall input signal is transformed
1120 before reaching the stalagmite. Rather than using hydrological or geochemical modelling, a
1121 recent publication introduced a Monte Carlo approach to model rainfall and temperature
1122 seasonality in a stalagmite from La Garma Cave, northern Spain, over the Holocene (Baldini
1123 et al., 2019). Here, we build a second generation of this model and compare results to both
1124 synthetic and real-world input data. Whereas the older version of the model could only run a
1125 limited number of simulations and a run stopped once the model converged upon a solution
1126 (though it could be run multiple times), this next generation model is able to run a large

1127 number (user-defined; we used 1,000 simulations in the runs presented here) of simulations
1128 and retain the output of each one, permitting the creation of probability distributions for each
1129 timeslice.

1130 This new model requires some widely available types of input data, including: i) a stalagmite-
1131 based $\delta^{18}\text{O}$ record, ii) a record of regional mean annual temperature (MAT) of any resolution
1132 (e.g., borehole, marine sediments, stalagmite fluid inclusions) over the interval of interest, iii)
1133 monthly-scale modern instrumental records of rainfall and temperature above the site (or as
1134 close as possible to the site), and iv) cave air temperature and its relationship with above
1135 ground temperature. The relationship between meteoric precipitation $\delta^{18}\text{O}$ and temperature
1136 at the site is useful but not required information because regional or global meteoric
1137 precipitation $\delta^{18}\text{O}$ and temperature equations can provide a suitable alternative.

1138 Essentially, the model assumes that the MAT of the cave site is similar to the MAT of the
1139 regional surface temperature input record (ii above) and produces a sine function around this
1140 value of an amplitude reflecting modern surface temperature seasonality but with random
1141 variability added to the absolute minimum and maximum temperatures (the amount of
1142 randomness is user-defined). A second sine function reflects the rainfall seasonality, and
1143 whereas the temperature wave's polarity is fixed (i.e., summers are always warmer than
1144 winters), the rainfall seasonality sine wave's polarity is allowed to flip randomly (but where
1145 only outputs that 'converge' are retained, and unrealistic results are rejected – see below).
1146 The seasonal extreme values ('extreme' meaning minima and maxima) associated with either
1147 sine function are fixed to the same calendar months, linked to the timing of the modern
1148 minima and maxima.

1149 These two sine waves produce synthetic monthly temperature and rainfall values, which are
1150 then converted to $\delta^{18}\text{O}_p$ based ideally on local temperature-rainfall $\delta^{18}\text{O}$ relationships, or in
1151 cases where this relationship is not known, to more global equations (e.g., (Schubert and
1152 Jahren, 2015)). It is assumed that the $\delta^{18}\text{O}_p$ is conveyed to the dripwater (see discussion
1153 regarding evapotranspiration, Section 4.3) and that this is converted to carbonate $\delta^{18}\text{O}$ using
1154 the Tremaine equation (Tremaine et al., 2011) at ambient cave air temperature adjusted
1155 according to observed relationships between outside and inside air. This equation was chosen
1156 as most appropriate because its empirical nature accounts for in-cave disequilibrium
1157 fractionation processes more completely than other equations. The model therefore
1158 considers seasonal changes in rainfall but is independent of total annual rainfall. The annual
1159 amount-weighted mean modelled carbonate $\delta^{18}\text{O}$ value is then compared with the actual
1160 measured carbonate $\delta^{18}\text{O}$ value, and if it is within a certain user-defined value, it is logged as
1161 a successful simulation. If the difference between the modelled and actual carbonate $\delta^{18}\text{O}$ is
1162 greater than this value (generally ~ 0.1 per mil), the simulation is logged as unsuccessful. 1,000
1163 of these coupled temperature and rainfall simulations are conducted per time slice, all the
1164 successful and unsuccessful simulations are logged, and the mean monthly modelled rainfall
1165 and temperature values calculated from the successful simulations. For a table describing the
1166 steps in the modelling process, please see Baldini et al. (2019).

1167

1168 **5.1 Test Runs: Gradual shifts in rainfall polarity**

1169 In this section we test the ability of the second-generation model to extract seasonality
1170 information using synthetic data. The model reproduces shifts in rainfall polarity in synthetic

1171 datasets well (Figure 7). In one experiment, the input $\delta^{18}\text{O}$ dataset was created by using i) a
1172 temperature sine function that was set as invariant (i.e., it maintained its polarity and
1173 amplitude throughout the run), and ii) a rainfall sine function that shifted in polarity
1174 completely over 14 model years. The input sine waves were used to create the annually-
1175 resolved synthetic $\delta^{18}\text{O}$ record but were independent from the sine waves generated by the
1176 model. The wettest month in the input rainfall record was April in Year 1, gradually changing
1177 polarity to November by Year 14. As such, model Year 7 was characterised by no seasonality
1178 (Figure 7). The model was run without *a priori* knowledge of these shifts other than the mean
1179 annually-resolved synthetic $\delta^{18}\text{O}$ record, MAT, 'modern' seasonality range, and cave
1180 temperature (i.e., the simulations were run 'modeller blind'), but the output reproduced the
1181 shifting rainfall pattern very well. The gradual shift in rainfall polarity is detected, and the lack
1182 of seasonality in the input rainfall signal during Year 7 is reproduced. The input temperature
1183 data had a 15 °C annual temperature range, and two model simulations were conducted: one
1184 derived using an annual seasonal temperature range of 10 ± 6 °C, and a second using an
1185 annual seasonal temperature range of 15 ± 6 °C. In the case of the lower annual temperature
1186 range, the model overestimates rainfall seasonality to compensate for the inappropriate
1187 annual temperature range, but still detects shifts in rainfall polarity (Figure 7). When the more
1188 appropriate temperature range is used, the simulation captures both the amplitude and
1189 polarity of the shifting rainfall input signal. However, this experiment highlights a limitation
1190 of this modelling approach; $\delta^{18}\text{O}$ data is explicable both in terms of rainfall and temperature
1191 seasonality shifts, and an unknown annual temperature range introduces uncertainties.

1192 A second experiment involved synthetic temperature and rainfall input records with both
1193 considerable inter-annual variability and noise introduced (Figure 8). Notably, one model year

1194 (Year 4) had the polarity of the rainfall signal completely reversed. Again, the model was able
1195 to extract the salient features of the input data very well. Reproduced were inter-annual
1196 variations in rainfall and temperature, and, importantly, the model detected the reversed
1197 seasonality of the rainfall signal in Year 4 (Figure 8).

1198

1199 **5.2 Application to a stalagmite $\delta^{18}\text{O}$ dataset from a seasonally arid continental region**

1200 The first version of the model was run successfully across the Holocene using a $\delta^{18}\text{O}$ dataset
1201 derived from the maritime climate of northern Spain (Baldini et al., 2019). Here, we apply the
1202 second-generation model to a dataset from Bir-Uja Cave in the Keklik-Too mountain ridge,
1203 Kyrgyzstan, a location characterised by extremely strong seasonal fluctuations in both
1204 temperature and rainfall. The cave ($40^{\circ}29'\text{N}$, $72^{\circ}35'\text{E}$) is ~ 60 m long and is developed at an
1205 altitude of $\sim 1,325$ m above sea level (Fohlmeister et al., 2017). The input data consisted of
1206 the $\delta^{18}\text{O}$ dataset from stalagmite Keklik1 reported on in Fohlmeister et al. (2017), a 500-year
1207 long, centennial-resolution borehole temperature record from the Tian Shan mountains
1208 (~ 461 km to the north of the cave site) (Huang et al., 2000), instrumental precipitation and
1209 temperature records since 1880 C.E. from Tashkent, Uzbekistan (~ 300 km to the east) (Menne
1210 et al., 2012), and cave temperature (Fohlmeister et al., 2017). The $\delta^{18}\text{O}$ input data were
1211 decadal-resolved, and the stalagmite was dated using a recently developed radiocarbon
1212 technique (Fohlmeister and Lechleitner, 2019; Fohlmeister et al., 2017; Lechleitner et al.,
1213 2016b). The Keklik1 record extends from 2011 C.E. back to 1150 C.E., but the borehole record
1214 only extends back to 1500 C.E., so the interval modelled only extends to 1500 C.E. On average,
1215 the site receives ~ 450 mm of precipitation per year (based on Global Network of Isotopes in

1216 Precipitation data from Tashkent), with ~80% falling from November to April. Summers are
1217 very dry, with August (the driest month) receiving ~5 mm of rainfall. Monthly temperatures
1218 range from -1.4 °C in January to 25.0 °C in July, with a MAT of 12.1 °C. Stalagmite Keklik1 was
1219 located ~40 meters from the cave entrance and was collected in October 2011. Cave
1220 temperature varies seasonally, from 12 °C from the end of November until April, to a
1221 maximum of 16.5 °C in May. The site is characterised by near 100% relative humidity in the
1222 cold season which drops considerably to ~60% during the warmer months (Fohlmeister et al.,
1223 2017).

1224 Unlike the Spanish GAR-01 record which extended back to ~13,500 years BP and was
1225 modelled using 100-year timeslices (Baldini et al., 2019), the Keklik1 $\delta^{18}\text{O}$ record was
1226 modelled using annual timeslices. The duration of the timeslice is user-defined and is
1227 independent of the resolution of the original stalagmite $\delta^{18}\text{O}$ dataset, but a timeslice with a
1228 somewhat higher resolution than the $\delta^{18}\text{O}$ dataset ensures that the input data are entirely
1229 represented. The timings of the minimum and maximum values of the modelled temperature
1230 sine function were fixed at January and July, respectively. These months were also designated
1231 as the minimum/maximum of the modelled rainfall sine wave, which fits present day
1232 observations, but the sine function's polarity was not prescribed in advance.

1233 Baldini et al. (2019) noted that the modelled temperature curve for northern Iberia closely
1234 resembled a previously published temperature reconstruction for the region (Martin-Chivelet
1235 et al., 2011) with a temporal resolution that exceeded the information provided by the low-
1236 resolution input dataset. Although no annual-scale MAT record exists in the Kyrgyzstan region
1237 for the last 500 years, summer temperatures are well constrained by tree ring records. A
1238 comparison of the modelled July temperature derived from the Keklik1 $\delta^{18}\text{O}$ record reveals a

1239 very good match with the NTREND AG2 temperature anomalies (~300 km to the north of the
1240 cave site) (Anchukaitis et al., 2017; Cook et al., 2013) (Figure 9). The model's ability to
1241 reconstruct palaeotemperature may reflect the fact that the probability of a successful model
1242 run is maximised when modelled temperature approximates the actual temperature shift.
1243 Successful model runs with a different (and incorrect) temperature pattern are possible with
1244 certain modelled rainfall simulations, but the mean monthly temperature values (reflecting
1245 the mean of all successful runs) will be biased towards model simulations with the correct
1246 temperature shift. The apparently robust reconstruction of warm-season palaeotemperature
1247 is an unexpected and exciting model outcome, but one that requires further evaluation.

1248 The rainfall reconstruction reproduces many of the same features highlighted by Fohlmeister
1249 et al. (2017). In particular, decreases in the winter rainfall contributions in the late 1500s, the
1250 mid-1700s, and the early 1800s are apparent in both records. This agreement is expected
1251 because the $\delta^{18}\text{O}$ record is integral to both reconstructions, but it is interesting that the two
1252 reconstructions use two fundamentally different techniques (numerical versus geochemical
1253 modelling) to estimate the importance of winter rainfall to the overall annual water budget
1254 at the site and arrive at broadly similar results. For example, a winter rainfall peak occurs in
1255 1797 CE in both records and transitions to drier winters by 1815 CE, with ~22% and ~50%
1256 reductions in winter rainfall implied by the model and $\delta^{18}\text{O}$ data, respectively. The model
1257 underestimating the reduction in rainfall probably arises because of the model's utilisation of
1258 smooth sine waves rather than more step-like functions; in other words, although it is
1259 possible for one month per year to have zero rainfall in the model, the adjacent two months
1260 must necessarily have some rainfall, whereas in reality, several dry months per summer could
1261 occur. The use of step functions would permit the incorporation of several dry months

1262 annually and would amplify apparent shifts in seasonal rainfall amounts. Modelled DJFM
1263 rainfall compares reasonably well with GHCN rainfall from Tashkent (Figure 9), particularly
1264 considering that the Tashkent meteorological station is ~300 km away from and ~1,000 m
1265 lower in altitude than the cave site.

1266

1267 **5.3 Limitations to the modelling technique and future work**

1268 Several limitations to the presented modelling technique exist. First, the timing of the rainfall
1269 minima and maxima versus temperature signal could affect the model's efficacy; for example,
1270 if the rainiest month occurs three months after (or before) the warmest month, the use of
1271 the sine function means that all outcomes are possible. This is because the maxima/minima
1272 in one parameter's sine function occur at the nodes of the other sine wave, effectively making
1273 both sine waves independent of each other. At many sites, temperature and rainfall are
1274 intrinsically linked and their seasonal cycle broadly synchronous, but the above may be an
1275 issue at some locations. Additionally, the model would require a differently shaped rainfall-
1276 function to model rainfall at locations with two distinct rainy intervals every year, such as low
1277 latitude sites affected by the ITCZ twice each year.

1278 The current version of the model does not incorporate evapotranspiration, and this is an
1279 obvious oversimplification. This may have repercussions for sites like Kyrgyzstan that
1280 experience a pronounced hot and dry season with negative effective infiltration. Similarly,
1281 variable kinetic fractionation almost certainly occurred within the cave (Fohlmeister et al.,
1282 2017) but is not considered within the model. Future versions of the model will incorporate
1283 both evapotranspiration and kinetic effects, but the model currently likely overcomes this

1284 limitation simply by reducing rainfall amount for months with high evapotranspiration rates.
1285 Potentially, coupling the new model discussed here with a dripwater isotope evolution model
1286 (e.g., ISOLUTION (Deininger and Scholz, 2019)) could produce very robust results. The model
1287 also cannot identify intervals characterized by changes in moisture pathway or fractionation
1288 amount; rather, it highlights intervals that are not explicable in terms of changes in
1289 temperature or rainfall amount seasonality (intervals where the model cannot converge on
1290 any solutions), and thus points to the involvement of other processes.

1291 The model is allowed to randomly vary MAT above or below the low-resolution temperature
1292 input record, but only within user-defined bounds. Too great a range of permissible MAT
1293 values would allow essentially any outcome. For example, if there were no limits to minimum
1294 winter temperature, a low $\delta^{18}\text{O}$ value could be modelled as either a very cold winter with a
1295 subdued rainfall seasonality or as a mild winter but with substantial winter rain. Limiting the
1296 temperature seasonality to reasonable bounds (for example, based modern interannual MAT
1297 variability) permits assessing whether any given month is warmer or colder than the low-
1298 resolution temperature input, but may underestimate the total amount of cooling and
1299 warming. In extreme cases, this may manifest itself as a failure to converge upon any
1300 successful model, thus highlighting timeslices that require closer inspection and potentially
1301 an alternative explanation.

1302 As discussed in Section 5.2, the utilisation of step functions to describe rainfall seasonality
1303 may facilitate the modelling of climate for sites where several months receive similar amounts
1304 of rainfall. Future studies should investigate the ramifications of function choice on output.
1305 Additionally, theoretically arriving at a mathematical solution utilising the relevant equations
1306 and input data is possible, obviating the need for MC simulations, and future research will

1307 investigate this possibility. Finally, future models could incorporate options for geochemical
1308 modelling of drip and carbonate chemistry.

1309

1310 **6. Regional seasonality**

1311 In this section we analyse global meteoric precipitation and temperature data to highlight
1312 regions experiencing pronounced seasonal variability in temperature, precipitation amount,
1313 and precipitation $\delta^{18}\text{O}$ (Figures 10 and 11), helping to facilitate the identification of cave sites
1314 sensitive to seasonality. This also highlights locations that are at the margins of such regions,
1315 where seasonality may have affected the record in the past, despite the lack of a modern
1316 influence.

1317

1318 **6.1. Identification of seasonally sensitive regions**

1319 WorldClim Version 2 data were obtained at a 2.5 minute (~4.5 km at the equator) spatial
1320 resolution (Fick and Hijmans, 2017). Inland continental regions within the mid- to high-
1321 latitudes of the Northern Hemisphere (e.g., central and northern Canada, eastern Russia,
1322 northeast China, and Mongolia) are characterised by the greatest mean annual temperature
1323 range (Figure 10a). A greater annual temperature range is characteristic of continental
1324 climates due to the reduced oceanic influence, with ocean water's high heat capacity and
1325 moderating influence on air temperature. The lowest mean annual temperature ranges occur
1326 in the low latitudes (where insolation remains high year-round) and maritime regions of the
1327 world (where oceans moderate temperature variability) (Figure 10a). The pattern of global

1328 temperature seasonality (herein calculated as the maximum temperature of the warmest
1329 month minus the minimum temperature of the coldest month averaged over the period 1970
1330 – 2000 based on WorldClim Version 2 data) is consistent with the geographic pattern of cave
1331 air ventilation reported in (James et al., 2015), a study concerning the role of outside
1332 temperature seasonality in the seasonal ventilation of caves.

1333 Seasonality in precipitation amount (Figure 10b) is greatest in the low latitudes due to the
1334 annual migration of the Intertropical Convergence Zone (ITCZ) and monsoonal systems that
1335 cause distinct wet and dry seasons, along the western coast of North America, southern South
1336 America, and Europe where seasonal westerlies preferentially bring enhanced winter
1337 precipitation, and bordering the Mediterranean where a ‘Mediterranean climate’
1338 characterised by wet-winters and dry-summer dominates (Figure 10b). The lowest
1339 precipitation amount seasonality occurs in arid and semi-arid regions of the world and the
1340 non-coastal mid- to high-latitudes of the northern and southern hemispheres.

1341 Global seasonality in amount-weighted $\delta^{18}\text{O}_p$ (Figure 11) approximates the pattern of
1342 temperature seasonality (Figure 10a), with the greatest annual range in $\delta^{18}\text{O}_p$ observed at
1343 Northern Hemisphere continental interior and high latitude sites (e.g., northeast Asia, central
1344 Canada, northern Greenland). In addition, high altitude sites (e.g., the Andes in western South
1345 America, the Caucasus Mountains at the intersection of Europe and Asia) also exhibit higher
1346 annual WM $\delta^{18}\text{O}_p$ ranges due to the altitude effect. The lowest $\delta^{18}\text{O}_p$ seasonality occurs within
1347 maritime (e.g., NW Europe, SW and SE Australia) and arid/semi-arid regions (e.g., East Africa,
1348 eastern Brazil, South Africa). Many stalagmite records are from temperate regions where
1349 modern MAT ranges from 10 to 16 °C (Baldini et al., 2019; Baldini et al., 2015; Ban et al., 2018;
1350 Huang et al., 2001; Johnson et al., 2006; Orland et al., 2014). Global cave dripwater $\delta^{18}\text{O}$ data

1351 reveal that caves from regions with this MAT range have dripwater chemistry that reflects
1352 recharge-weighted $\delta^{18}\text{O}_p$ (Baker et al., 2019). The seasonal distribution of $\delta^{18}\text{O}_p$ is therefore
1353 a critical control in the case of many different stalagmite samples.

1354 In other cases, very pronounced seasonality inherent in stalagmite geochemical records are
1355 not due to seasonality in $\delta^{18}\text{O}_p$, but instead to seasonality in rainfall amount (Ridley et al.,
1356 2015b) and associated shifts in bioproductivity (Baldini et al., 2005) or PCP (Fairchild and
1357 Hartland, 2010; Fairchild et al., 2006). Seasonality in temperature can also induce cave
1358 ventilation in temperate zone caves during the winter (providing the cave geometry is
1359 appropriate), promoting carbonate deposition within the cave and biasing annual- to decadal-
1360 scale records towards the winter season rainfall (James et al., 2015). The maps provided
1361 herein can help identify regions containing speleothems retaining the desired seasonal signal,
1362 and determine what the most likely control is on any seasonal signal found within a
1363 stalagmite. Furthermore, the maps help highlight cave sites that are located on the
1364 peripheries of climatologically seasonal zones at present, where past seasonality shifts could
1365 have influenced a record. Examples include the Sahel and southern Belize (Figure 12), both
1366 currently at the very northern extent of the ITCZ, where a small ITCZ shift to the south would
1367 produce both severe drying and a substantial decrease in rainfall seasonality. This perspective
1368 was underscored by recent results from Central America that used monthly-scale rainfall
1369 proxy data over the last two millennia to suggest that the region has only been affected by
1370 the ITCZ since ~1400 C.E., and that the ITCZ influence may wane in the near future (Asmerom
1371 et al., 2020) (Figure 12).

1372

1373 **6.2. Complexities despite strong seasonality: northeast India as an example**

1374 The seasonality maps presented here highlight regions most likely to contain stalagmites
1375 which retain seasonal signals in temperature, rainfall amount, or $\delta^{18}\text{O}_p$. However, they also
1376 illustrate that not all seasonal variations in $\delta^{18}\text{O}_p$ are explicable in regional temperature or
1377 rainfall amount terms. In many cases, complex moisture source variability overprints
1378 temperature-induced seasonality, hampering the use of models such as the one presented in
1379 Section 5. Here, we discuss the Indian Summer Monsoon (ISM) as an example of such a
1380 situation, and focus specifically on Mawmluh Cave in Meghalaya, northeast India, one of the
1381 most seasonal locations on Earth in terms of rainfall amount (Fig. 10). In Meghalaya,
1382 hydroclimate is characterised by extreme seasonality, as the plateau constitutes the first
1383 topographic barrier for moisture-laden air masses travelling inland from the Bay of Bengal
1384 (Murata et al., 2007; Prokop and Walanus, 2003). At present, the ISM brings ~80% of the
1385 annual rainfall to the cave site, inducing extreme amounts of rainfall (up to 12 meters per
1386 year (Breitenbach et al., 2015). The seasonal precipitation cycle is reflected in rainfall $\delta^{18}\text{O}$
1387 composition (Berkelhammer et al., 2012; Breitenbach et al., 2010). Rainfall $\delta^{18}\text{O}$ becomes
1388 progressively lighter during the ISM, but this effect is only partially driven by increasing
1389 precipitation intensity and the amount effect because the period of maximum precipitation
1390 (June-August) precedes maximum ^{18}O depletion (August-October) (Breitenbach et al., 2010)).
1391 Instead, the ^{18}O -depletion results predominantly from the moisture source shifting from a
1392 proximal location (the Bay of Bengal) in the early and late ISM to a more distal location (the
1393 open Indian Ocean) during the peak ISM (longer transport times resulting in more Rayleigh
1394 distillation). Rainfall and dripwater $\delta^{18}\text{O}$ at Mawmluh Cave are thus highly seasonal, but the
1395 relationship between temperature, rainfall amount, and rainfall $\delta^{18}\text{O}$ is not straightforward
1396 (Breitenbach et al., 2010; Breitenbach et al., 2015). Additional complexity arises from the
1397 filtering and buffering capacity of the karst aquifer through which rainwater percolates *en*

1398 *route* to a stalagmite. Although a clear seasonal dripwater $\delta^{18}\text{O}$ cycle exists, with its lowest
1399 value approximating ISM rainfall $\delta^{18}\text{O}$, its annual amplitude is compressed, reflecting buffering
1400 in the karst (Breitenbach et al., 2015). This further complicates the interpretation of $\delta^{18}\text{O}$
1401 records from these stalagmites, and information from independent proxies that are sensitive
1402 to processes dominating during the winter season is required to disentangle such processes.
1403 Combining summer-sensitive $\delta^{18}\text{O}$ with winter-sensitive Mg/Ca (reflecting PCP) permitted
1404 disentangling ISM strength and the degree of dry season dryness in a stalagmite from
1405 Mawmluh Cave (Myers et al., 2015; Ronay et al., 2019). Such a multi-proxy approach,
1406 supported by local monitoring and karst process modelling, allows robust interpretations of
1407 seasonal-scale climate from stalagmites, even when the proxy seasonality is driven by more
1408 complex processes than temperature or rainfall amount alone.

1409

1410 **7. Future directions and recommendations**

1411 In this review, we introduce and discuss several concepts that we hope will facilitate the
1412 development and interpretation of robust seasonal-resolution climate records from
1413 stalagmites, will improve the extraction and interpretation of seasonal information from
1414 stalagmites, and promote future discussion, including: **A)** that replication of records should
1415 not always be an expectation without *a priori* knowledge that the drip type and
1416 environmental conditions responsible for the deposition of the stalagmites are comparable
1417 (e.g., some stalagmites retain seasonal information, others do not), **B)** that every stalagmite-
1418 based geochemical record is different and records a unique component of the environmental
1419 signal of varying complexity (i.e., each stalagmite retains an accurate history of its
1420 environment; the question is whether or not this history can be deconvolved), and **C)** that the

1421 application of at least one year's worth of hourly-resolved drip rate monitoring combined
1422 with a new drip classification scheme presented here may help identify stalagmites retaining
1423 a seasonal signal. Furthermore, we have **(D)** developed global seasonality maps of
1424 temperature (as was done previously by (James et al., 2015)), meteoric precipitation amount,
1425 and meteoric precipitation $\delta^{18}\text{O}$ ratios which allow the identification of regions sensitive to
1426 different types of seasonality recordable by stalagmites. The maps facilitate predicting what
1427 type of seasonality potentially affects modern stalagmite samples from that region. They also
1428 assist in palaeoclimate interpretations by identifying locations proximal to regions with
1429 pronounced seasonality, where past migration of key atmospheric circulation systems could
1430 have altered the geochemical record retained by a stalagmite. On a similar note, we **(E)**
1431 present a model that interprets annual- to centennial-scale stalagmite $\delta^{18}\text{O}$ records in terms
1432 of seasonal temperature and meteoric precipitation seasonality shifts. Although we stress
1433 that this model only highlights one possible interpretation (that the data were modulated
1434 primarily by regional long-term mean annual temperature variability combined with
1435 seasonality shifts in rainfall and temperature), often this interpretation is the most
1436 parsimonious. The modelling technique also helps identify time intervals when altered
1437 seasonality cannot account for the observed isotope shifts, suggesting that another variable
1438 needs consideration. We **(F)** discuss four major controls on the seasonality signal within
1439 stalagmites: i) Earth atmospheric, ii) Meteoric precipitation, iii) biological (e.g., soil processes),
1440 and iv) cave atmospheric, and **(G)** discuss a case study from India that serves as an example
1441 of a stalagmite whose seasonal signal is not derived from rainfall amount or regional
1442 temperature, but instead results from seasonal shifts in air mass trajectories (i.e., affected by
1443 seasonal shifts in Earth atmospheric processes).

1444 Stalagmites are remarkable archives of information regarding climate (on both seasonal and
1445 longer timescales), surface and cave environmental conditions, dry deposition, moisture
1446 source pathway, marine aerosols contributions, and hydrological routing. Replication of proxy
1447 records present strong support for palaeoclimatic interpretations and should remain a goal
1448 of any stalagmite science research programme, but unless the climate signal-to-noise ratio of
1449 a region is unusually high, replication is only possible when comparing stalagmites deposited
1450 under similar conditions. A thorough understanding of the environmental processes affecting
1451 both entire caves (e.g., ventilation) as well as individual stalagmites (e.g., drip rate) facilitates
1452 replication efforts. The geochemical record from even adjacent stalagmites will reflect
1453 numerous processes, some of which are common to the two samples but many which are
1454 not, and only through a thorough understanding of the processes affecting each sample are
1455 robust (and replicable) climate interpretations achievable. However, unless analytical issues
1456 exist, non-replication does not imply that one record is incorrect; rather it generally implies
1457 that the two records simply record different environmental parameters.

1458 Cave monitoring prior to the collection of a stalagmite will increase the likelihood of obtaining
1459 a record of the desired sensitivity to seasonal climate shifts, or other desired forcing. We
1460 recommend monitoring the drip feeding the stalagmite for at least one year using an
1461 automated drip logger and plotting the results in a diagram similar to Figure 3 to evaluate a
1462 stalagmite's likelihood of retaining hydrological seasonality. We recommend monitoring
1463 multiple sites within the cave and selecting the most appropriate stalagmite for collection
1464 based on the monitoring results. It is worth bearing in mind that unless the seasonality signal
1465 in a stalagmite is conveyed via seasonal cave ventilation, stalagmites fed by diffuse flow drips
1466 with long residence times may not retain seasonal information. Other drips that are

1467 seasonally either dry or undersaturated with respect to carbonate will lead to the occurrence
1468 of seasonal hiatuses in the stalagmites and signal loss for that particular season. Monitoring
1469 a stalagmite's drip rate and drip chemistry for as long as possible represents one of the
1470 simplest but most effective means of understanding the potential climate signal contained
1471 within a sample prior to collection. This also has implications for cave conservation and
1472 protection efforts, because clearly formulated research goals and drip monitoring prior to
1473 stalagmite sample collection can greatly reduce the number of samples removed from a cave
1474 for research purposes.

1475 If sample growth rate permits, we suggest that the extraction of the palaeoseasonality signal
1476 over millennial timescales is best achieved via micromilling, leaving no gap between adjacent
1477 samples, or LA-ICPMS. The major disadvantages of micromilling are that it is resource
1478 intensive and that many samples may not have growth rates high enough to permit the
1479 required temporal resolution. The major disadvantage of LA-ICPMS is that the trace element
1480 signature of a stalagmite is often dominated by site-specific factors such as temperature, sea
1481 spray, volcanic aerosols, fire, variable throughput of colloidal material, or rainfall, and
1482 consequently aligning the data with other records is sometimes complex. Micromilled
1483 carbonate powders that are divided into two or more aliquots that are subsequently analysed
1484 for stable isotope ratios, trace elements, and other geochemical proxies can provide very
1485 robust interpretations (e.g., Jamieson et al., 2016). This eliminates issues of cross-correlation
1486 and enables a powerful multiproxy approach, where each stable isotope ratio value is linked
1487 directly and unambiguously to numerous elemental concentration values. The technique can
1488 yield important information regarding palaeoseasonality but is considerably more resource
1489 intensive than running multiple LA-ICPMS tracks parallel to each other and the micromilled

1490 stable isotope track. An alternative is to produce a long decadal-scale isotope ratio traverse
1491 complemented by higher resolution transects or maps across key intervals of interest using
1492 LA-ICPMS, SIMS, synchrotron, or μ XRF to corroborate interpretations based on the longer
1493 transects. In the future, proxy mapping at micron-scale resolution using these techniques will
1494 help reduce uncertainties related to geometric ambiguities such as those associated with
1495 crystal boundaries and improve the robustness of interpretations.

1496

1497 **9. Conclusions**

1498 The reconstruction of palaeoseasonality using stalagmites is an exciting research direction
1499 that has yet to mature into its full potential. Numerous records of palaeoseasonality exist, but
1500 few direct reconstructions extend before the last two millennia. Ideally, future studies
1501 concluding that a decadal- to annual-scale isotope ratio record is affected by seasonality
1502 changes should support this by either using short windows of sub-annual data or by
1503 modelling.

1504 Any stalagmite-based climate proxy record is affected by inherent complexities in climate
1505 signal transfer to the stalagmite and by selective sampling of the stalagmite for analysis. A
1506 high-resolution (sub-annual to annual-scale) sampling strategy coupled with appropriate site
1507 monitoring maximises the likelihood of extracting a signal approximating the climate input
1508 signal. For long records annual- to decadal-scale resolution is ideal, and shorter records could
1509 benefit from an even higher resolution if resources permit. Large shifts in isotope ratios could
1510 reflect changes in seasonality, potentially associated with the migration of key atmospheric
1511 circulation systems over the cave site. New models incorporating seasonality can provide

1512 information regarding whether observed geochemical shifts are interpretable in terms of
1513 altered seasonality, and these represent an exciting and inexpensive new research tool. A
1514 seasonal-scale sampling strategy over short intervals of interest can verify these model
1515 interpretations, and LA-ICPMS or line-scan μ XRF represent potentially the most efficient
1516 methods to achieve this; other alternatives include monthly-scale micromilling, synchrotron
1517 analysis (SR- μ XRF), and SIMS.

1518 The robust interpretation of stalagmite geochemical records in terms of seasonality
1519 represents a key challenge for the next decade. Achieving this is complicated by multiple in-
1520 cave and exogenic environmental forcings with dynamic seasonality, including: rainfall,
1521 temperature, humidity, bioproductivity, cave air $p\text{CO}_2$, drip rate, source moisture region and
1522 $\delta^{18}\text{O}$, and moisture mass trajectory from the source region. Even apparently straightforward
1523 $\delta^{18}\text{O}$ records from regions with high signal-to-noise ratios typically interpretable as either
1524 varying total annual rainfall or summer rainfall may reflect another parameter instead (e.g., a
1525 change in moisture source or rainfall seasonality), as is the case with the Indian Summer
1526 Monsoon. Most records would benefit from a rigorous multi-proxy approach utilising not only
1527 multiple geochemical proxy datasets, but also site monitoring and new modelling approaches.
1528 Similarly, focussing research efforts at the same well-understood cave sites both maximises
1529 the quality of interpretations and contributes to the conservation of caves and stalagmite
1530 samples. The application of multiple stalagmites from the same site but with different drip
1531 rates and affected by different amounts of disequilibrium fractionation may provide the key
1532 to reconstructing formerly elusive climate variables, such as temperature. Instead of
1533 representing an irresolvable issue, we suggest that disequilibrium fractionation may present
1534 opportunities to quantify temperature, potentially even at seasonal resolutions. Similarly,

1535 multi-proxy data could yield seasonal information even in the absence of seasonal sampling
1536 resolution; if two or more independent proxies reflect different seasonal data, combining the
1537 proxies could yield palaeoseasonality.

1538 Over the past few decades stalagmites have provided some of the most iconic records in
1539 palaeoclimatology. In the future, stalagmites will continue to not only provide long records of
1540 exceptional quality, but they will also provide rare glimpses into palaeoseasonality at
1541 unprecedented temporal resolution. Recent microanalytical advances have facilitated the
1542 construction of exquisitely resolved stalagmite-based climate records; we are now at a stage
1543 where the interpretation of these records is catching up with their remarkable technical
1544 aspects. Extracting quantitative and accurate seasonal climate information from these
1545 geochemical records is a key challenge over the next decade, and, if this is achieved,
1546 stalagmites will truly be considered in a class of their own as climate archives.

1547

1548 **Acknowledgements**

1549 We thank SISAL and PAGES for access to the SISAL database v1b. Portions of this research
1550 were funded by European Research Council Grant #240167. Tim Horscroft is thanked for his
1551 support in facilitating the preparation of the manuscript. Ian Orland and Jasper Wassenburg
1552 are thanked for detailed constructive reviews that greatly improved the manuscript. Alex
1553 Iveson is thanked for useful comments regarding LA-ICPMS.

1554

1555 **References:**

- 1556 Allison, V.C., 1923. The growth of stalagmites and stalactites. *Journal of Geology* 31, 106-125.
- 1557 Allison, V.C., 1926. The antiquity of the deposit in Jacob's cavern. *American Museum of Natural*
1558 *History, Anthropological Papers* 19, 204-225.
- 1559 Anchukaitis, K.J., Wilson, R., Briffa, K.R., Buntgen, U., Cook, E.R., D'Arrigo, R., Davi, N., Esper, J.,
1560 Frank, D., Gunnarson, B.E., Hegerl, G., Helama, S., Klesse, S., Krusic, P.J., Linderholm, H.W., Myglan,
1561 V., Osborn, T.J., Zhang, P., Rydval, M., Schneider, L., Schurer, A., Wiles, G., Zorita, E., 2017. Last
1562 millennium Northern Hemisphere summer temperatures from tree rings: Part II, spatially resolved
1563 reconstructions. *Quaternary Sci. Rev.* 163, 1-22.
- 1564 Arbel, Y., Greenbaum, N., Lange, J., Inbar, M., 2010. Infiltration processes and flow rates in
1565 developed karst vadose zone using tracers in cave drips. *Earth Surface Processes and Landforms* 35,
1566 1682-1693.
- 1567 Arbel, Y., Greenbaum, N., Lange, J., Shtober-Zisu, N., Grodek, T., Wittenberg, L., Inbar, M., 2008.
1568 Hydrologic classification of cave drips in a Mediterranean climate, based on hydrograph separation
1569 and flow mechanisms. *Israel Journal of Earth Sciences* 57, 291-310.
- 1570 Asmerom, Y., Baldini, J.U.L., Prufer, K.M., Polyak, V.J., Ridley, H.E., Aquino, V.V., Baldini, L.M.,
1571 Breitenbach, S.F.M., Macpherson, C.G., Kennett, D.J., 2020. Intertropical convergence zone
1572 variability in the Neotropics during the Common Era. *Science Advances* 6, eaax3644.
- 1573 Atkinson, T.C., 1977. Diffuse flow and conduit flow in limestone terrain in the Mendip Hills, Somerset
1574 (Great Britain). *J Hydrol* 35, 93-110.
- 1575 Atkinson, T.C., Hess, J.W., Harmon, R.S., 1985. Stable isotope variations in recharge to a karstic
1576 aquifer, Yorkshire dales, England. *Annales de la Société Géologique de Belgique* 108, 225.

1577 Atsawawaranunt, K., Comas-Bru, L., Mozhdehi, S.A., Deininger, M., Harrison, S.P., Baker, A., Boyd,
1578 M., Kaushal, N., Ahmad, S.M., Brahim, Y.A., Arienzo, M., Bajo, P., Braun, K., Burstyn, Y., Chawchai, S.,
1579 Duan, W.H., Hatvani, I.G., Hu, J., Kern, Z., Labuhn, I., Lachniet, M., Lechleitner, F.A., Lorrey, A., Perez-
1580 Mejias, C., Pickering, R., Scropton, N., Members, S.W.G., 2018. The SISAL database: a global resource
1581 to document oxygen and carbon isotope records from speleothems. *Earth System Science Data* 10,
1582 1687-1713.

1583 Ayalon, A., Bar-Matthews, M., Sass, E., 1998. Rainfall-recharge relationships within a karstic terrain
1584 in the Eastern Mediterranean semi-arid region, Israel: $\delta^{18}\text{O}$ and δD characteristics *Journal of*
1585 *Hydrology* 207, 18-31.

1586 Badertscher, S., Borsato, A., Frisia, S., Cheng, H., Edwards, R.L., Tuysuz, O., Fleitmann, D., 2014.
1587 Speleothems as sensitive recorders of volcanic eruptions - the Bronze Age Minoan eruption recorded
1588 in a stalagmite from Turkey. *Earth Planet. Sci. Lett.* 392, 58-66.

1589 Baker, A., Barnes, W.L., Smart, P.L., 1997. Variations in the discharge and organic matter content of
1590 stalagmite drip waters in Lower Cave, Bristol. *Hydrological Processes* 11, 1541-1555.

1591 Baker, A., Bradley, C., 2010. Modern stalagmite $\delta^{18}\text{O}$: Instrumental calibration and forward
1592 modelling. *Global and Planetary Change* 71, 201-206.

1593 Baker, A., Brunsdon, C., 2003. Non-linearities in drip water hydrology: an example from Stump Cross
1594 Caverns, Yorkshire. *Journal of Hydrology* 277, 151-163.

1595 Baker, A., Hartmann, A., Duan, W., Hankin, S., Comas-Bru, L., Cuthbert, M.O., Treble, P.C., Banner, J.,
1596 Genty, D., Baldini, L.M., Bartolomé, M., Moreno, A., Pérez-Mejías, C., Werner, M., 2019. Global
1597 analysis reveals climatic controls on the oxygen isotope composition of cave drip water. *Nature*
1598 *Communications* 10, 2984.

1599 Baker, A., Smart, P.L., Edwards, R.L., Richards, D.A., 1993. Annual growth banding in a cave
1600 stalagmite. *Nature* 364, 518-520.

1601 Baker, A.J., Matthey, D.P., Baldini, J.U.L., 2014. Reconstructing modern stalagmite growth from cave
1602 monitoring, local meteorology, and experimental measurements of dripwater films. *Earth Planet.*
1603 *Sci. Lett.* 392, 239-249.

1604 Baldini, J.U.L., Bertram, R.A., Ridley, H.E., 2018. Ground air: A first approximation of the Earth's
1605 second largest reservoir of carbon dioxide gas. *Sci. Total Environ.* 616-617, 1007-1013.

1606 Baldini, J.U.L., McDermott, F., Baker, A., Baldini, L.M., Matthey, D.P., Railsback, L.B., 2005. Biomass
1607 effects on stalagmite growth and isotope ratios: A 20th century analogue from Wiltshire, England.
1608 *Earth Planet. Sci. Lett.* 240, 486-494.

1609 Baldini, J.U.L., McDermott, F., Baldini, L.M., Ottley, C.J., Linge, K.L., Clipson, N., Jarvis, K.E., 2012.
1610 Identifying short-term and seasonal trends in cave drip water trace element concentrations based on
1611 a daily-scale automatically collected drip water dataset. *Chem. Geol.* 330, 1-16.

1612 Baldini, J.U.L., McDermott, F., Fairchild, I.J., 2002. Structure of the 8200-year cold event revealed by
1613 a speleothem trace element record. *Science* 296, 2203-2206.

1614 Baldini, J.U.L., McDermott, F., Fairchild, I.J., 2006. Spatial variability in cave drip water
1615 hydrochemistry: Implications for stalagmite paleoclimate records. *Chem. Geol.* 235, 390-404.

1616 Baldini, J.U.L., McDermott, F., Hoffmann, D.L., Richards, D.A., Clipson, N., 2008. Very high-frequency
1617 and seasonal cave atmosphere P_{CO_2} variability: Implications for stalagmite growth and oxygen
1618 isotope-based paleoclimate records. *Earth Planet. Sci. Lett.* 272, 118-129.

1619 Baldini, L.M., Baldini, J.U.L., McDermott, F., Arias, P., Cueto, M., Fairchild, I.J., Hoffmann, D.L.,
1620 Matthey, D.P., Müller, W., Nita, D.C., Ontañón, R., Garcíá-Moncó, C., Richards, D.A., 2019. North

1621 Iberian temperature and rainfall seasonality over the Younger Dryas and Holocene. *Quaternary Sci.*
1622 *Rev.* 226, 105998.

1623 Baldini, L.M., McDermott, F., Baldini, J.U.L., Arias, P., Cueto, M., Fairchild, I.J., Hoffmann, D.L.,
1624 Matthey, D.P., Müller, W., Nita, D.C., Ontañón, R., Garcíá-Moncó, C., Richards, D.A., 2015. Regional
1625 temperature, atmospheric circulation, and sea-ice variability within the Younger Dryas Event
1626 constrained using a speleothem from northern Iberia. *Earth Planet. Sci. Lett.* 419, 101-110.

1627 Ban, F.M., Baker, A., Marjo, C.E., Duan, W.H., Li, X.L., Han, J.X., Coleborn, K., Akter, R., Tan, M.,
1628 Nagra, G., 2018. An optimized chronology for a stalagmite using seasonal trace element cycles from
1629 Shihua Cave, Beijing, North China. *Scientific Reports* 8, 4551.

1630 Banner, J.L., Guilfoyle, A., James, E.W., Stern, L.A., Musgrove, M., 2007. Seasonal variations in
1631 modern speleothem calcite growth in Central Texas, USA. *J Sediment Res* 77, 615-622.

1632 Bar-Matthews, M., Ayalon, A., Matthews, A., Sass, E., Halicz, L., 1996. Carbon and oxygen isotope
1633 study of the active water-carbonate system in a karstic Mediterranean cave: Implications for
1634 paleoclimate research in semiarid regions. *Geochim. Cosmochim. Acta* 60, 337-347.

1635 Bergel, S.J., Carlson, P.E., Larson, T.E., Wood, C.T., Johnson, K.R., Banner, J., Breecker, D.O., 2017.
1636 Constraining the subsoil carbon source to cave-air CO₂ and speleothem calcite in central Texas. 217,
1637 112-127.

1638 Berkelhammer, M., Sinha, A., Stott, L., Cheng, H., Pausata, F.S.R., Yoshimura, K., 2012. An abrupt
1639 shift in the Indian Monsoon 4000 years ago. *Geophysical Monograph Series* 198, 75-87.

1640 Blyth, A.J., Baker, A., Thomas, L.E., Van Calsteren, P., 2011. A 2000-year lipid biomarker record
1641 preserved in a stalagmite from north-west Scotland. *J. of Quaternary Sci.* 26, 326-334.

1642 Borsato, A., Frisia, S., Fairchild, I.J., Somogyi, A., Susini, J., 2007. Trace element distribution in annual
1643 stalagmite laminae mapped by micrometer-resolution X-ray fluorescence: Implications for
1644 incorporation of environmentally significant species. *Geochim. Cosmochim. Acta* 71, 1494-1512.

1645 Borsato, A., Frisia, S., Hellstrom, J., Treble, P., Johnson, K., Howard, D., Greig, A., 2019. Fast high-
1646 resolution synchrotron micro-XRF mapping of annually laminated stalagmites, European Geoscience
1647 Union General Assembly. EGU, Vienna.

1648 Borsato, A., Frisia, S., Wynn, P.M., Fairchild, I.J., Miorandi, R., 2015. Sulphate concentration in cave
1649 dripwater and speleothems: long-term trends and overview of its significance as proxy for
1650 environmental processes and climate changes. *Quaternary Sci. Rev.* 127, 48-60.

1651 Breecker, D.O., Payne, A.E., Quade, J., Banner, J.L., Ball, C.E., Meyer, K.W., Cowan, B.D., 2012. The
1652 sources and sinks of CO₂ in caves under mixed woodland and grassland vegetation. *Geochim.
1653 Cosmochim. Acta* 96, 230-246.

1654 Breitenbach, S.F.M., Adkins, J.F., Meyer, H., Marwan, N., Kumar, K.K., Haug, G.H., 2010. Strong
1655 influence of water vapor source dynamics on stable isotopes in precipitation observed in Southern
1656 Meghalaya, NE India. *Earth and Planetary Science Letters* 292, 212-220.

1657 Breitenbach, S.F.M., Bernasconi, S.M., 2011. Carbon and oxygen isotope analysis of small carbonate
1658 samples (20 to 100 μ g) with a GasBench II preparation device. *Rapid Commun. Mass Spectrom.*
1659 25, 1910-1914.

1660 Breitenbach, S.F.M., Lechleitner, F.A., Meyer, H., Diengdoh, G., Matthey, D., Marwan, N., 2015. Cave
1661 ventilation and rainfall signals in dripwater in a monsoonal setting – a monitoring study from NE
1662 India. *Chemical Geology* 402, 111-124.

1663 Breitenbach, S.F.M., Plessen, B., Waltgenbach, S., Tjallingii, R., Leonhardt, J., Jochum, K.P., Meyer, H.,
1664 Goswami, B., Marwan, N., Scholz, D., 2019. Holocene interaction of maritime and continental climate

1665 in Central Europe: New speleothem evidence from Central Germany. *Global and Planet. Change* 176,
1666 144-161.

1667 Broecker, W.S., 1960. Radiocarbon measurements and annual rings in cave formations. *Nature* 185,
1668 93-94.

1669 Broughton, P.L., 1983. Environmental Implications of competitive growth fabrics in stalactitic
1670 carbonate. *International Journal of Speleology*. 13, 31-41.

1671 Buhmann, D., Dreybrodt, W., 1985. The kinetics of calcite dissolution and precipitation in
1672 geologically relevant situations of karst areas. 2. closed system. *Chem. Geol.* 53, 109-124.

1673 Cabellero, E., Jimenez de Cisneros, C., Reyes, E., 1996. A stable isotope study of cave seepage waters.
1674 *Applied Geochemistry* 11, 583-587.

1675 Carlson, P.E., Miller, N.R., Banner, J.L., Breecker, D.O., Casteel, R.C., 2018. The potential of near-
1676 entrance stalagmites as high-resolution terrestrial paleoclimate proxies: Application of isotope and
1677 trace-element geochemistry to seasonally-resolved chronology. *Geochimica et Cosmochimica Acta*
1678 235, 55-75.

1679 Chapman, J.B., Ingraham, N.L., Hess, J.W., 1992. Isotopic investigation of infiltration and unsaturated
1680 zone flow processes at Carlsbad Caverns. *Journal of Hydrology* 133, 343-363.

1681 Chen, C.-J., Li, T.-Y., 2018. Geochemical characteristics of cave drip water respond to ENSO based on
1682 a 6-year monitoring work in Yangkou Cave, Southwest China. *Journal of Hydrology* 561, 896-907.

1683 Cheng, H., Lawrence Edwards, R., Shen, C.-C., Polyak, V.J., Asmerom, Y., Woodhead, J., Hellstrom, J.,
1684 Wang, Y., Kong, X., Spötl, C., Wang, X., Calvin Alexander, E., 2013. Improvements in ^{230}Th dating,
1685 ^{230}Th and ^{234}U half-life values, and U–Th isotopic measurements by multi-collector inductively
1686 coupled plasma mass spectrometry. *Earth and Planetary Science Letters* 371-372, 82-91.

1687 Cole, J.M., Nienstedt, J., Spataro, G., Rasbury, E.T., Lanzirrotti, A., Celestian, A.J., Nilsson, M., Hanson,
1688 G.N., 2003. Phosphor imaging as a tool for in situ mapping of ppm levels of uranium and thorium in
1689 rocks and minerals. *Chem. Geol.* 193, 127-136.

1690 Comas-Bru, L., Harrison, S.P., 2019. SISAL: Bringing Added Value to Speleothem Research.
1691 *Quaternary* 2, 7.

1692 Comas-Bru, L., Harrison, S.P., Werner, M., Rehfeld, K., Scroxton, N., Veiga-Pires, C., Ahmad, S.M.,
1693 Brahim, Y.A., Mozhdehi, S.A., Arienzo, M., Atsawawaranunt, K., Baker, A., Braun, K., Breitenbach, S.,
1694 Burstyn, Y., Chawchai, S., Columbu, A., Deininger, M., Demeny, A., Dixon, B., Hatvani, I.G., Hu, J.,
1695 Kaushal, N., Kern, Z., Labuhn, I., Lachniet, M.S., Lechleitner, F.A., Lorrey, A., Markowska, M., Nehme,
1696 C., Novello, V.F., Oster, J., Perez-Mejias, C., Pickering, R., Sekhon, N., Wang, X.F., Warken, S.,
1697 Atkinson, T., Ayalon, A., Baldini, J., Bar-Matthews, M., Bernal, J.P., Boch, R., Borsato, A., Boyd, M.,
1698 Brierley, C., Cai, Y.J., Carolin, S., Cheng, H., Constantin, S., Couchoud, I., Cruz, F., Denniston, R.,
1699 Dragusin, V., Duan, W.H., Ersek, V., Finne, M., Fleitmann, D., Fohlmeister, J., Frappier, A., Genty, D.,
1700 Holzkamper, S., Hopley, P., Johnston, V., Kathayat, G., Keenan-Jones, D., Koltai, G., Li, T.Y., Lone,
1701 M.A., Luetscher, M., Matthey, D., Moreno, A., Moseley, G., Psomiadis, D., Ruan, J.Y., Scholz, D., Sha,
1702 L.J., Smith, A.C., Strikis, N., Treble, P., Unal-Imer, E., Vaks, A., Vansteenberge, S., Voarintsoa, N.R.G.,
1703 Wong, C., Wortham, B., Wurtzel, J., Zhang, H., Grp, S.W., 2019. Evaluating model outputs using
1704 integrated global speleothem records of climate change since the last glacial. *Clim Past* 15, 1557-
1705 1579.

1706 Cook, E.R., Krusic, P.J., Anchukaitis, K.J., Buckley, B.M., Nakatsuka, T., Sano, M., Asia2K, P., 2013.
1707 Tree-ring reconstructed summer temperature anomalies for temperate East Asia since 800 CE. *Clim.*
1708 *Dynam.* 41, 2957-2972.

1709 Cowan, B.D., Osborne, M.C., Banner, J.L., 2013. Temporal variability of cave air PCO₂ in Central
1710 Texas. *J Cave Karst Stud* 75, 38-50.

1711 Cruz Jr., F.W., Karmann, I., Vianna, J., O., Burns, S.J., Ferrari, J.A., Vuille, M., Sial, A.N., Moreira, M.Z.,
1712 2005. Stable isotope study of cave percolation waters in subtropical Brazil: Implications for
1713 paleoclimate inferences from speleothems. *Chemical Geology* 220, 245-262.

1714 Czuppon, G., Demény, A., Leél-Össy, S., Óvari, M., Stieber, J., Kiss, K., Kármán, K., Surányi, G.,
1715 Haszpra, L., 2018. Cave monitoring in the Béke and Baradla caves (Northeastern Hungary):
1716 implications for the conditions for the formation cave carbonates. *International Journal of*
1717 *Speleology*, 13-28.

1718 Daëron, M., Drysdale, R.N., Peral, M., Huyghe, D., Blamart, D., Coplen, T.B., Lartaud, F., Zanchetta,
1719 G., 2019. Most Earth-surface calcites precipitate out of isotopic equilibrium. *Nat Commun* 10.

1720 Deininger, M., McDermott, F., Mudelsee, M., Werner, M., Frank, N., Mangini, A., 2017. Coherency of
1721 late Holocene European speleothem delta O-18 records linked to North Atlantic Ocean circulation.
1722 *Clim. Dynam.* 49, 595-618.

1723 Deininger, M., Scholz, D., 2019. ISOLUTION 1.0: an ISOTOPE evoLUTION model describing the stable
1724 oxygen (delta O-18) and carbon (delta C-13) isotope values of speleothems. *Int J Speleol* 48, 21-32.

1725 Deininger, M., Werner, M., McDermott, F., 2016. North Atlantic Oscillation controls on oxygen and
1726 hydrogen isotope gradients in winter precipitation across Europe; implications for palaeoclimate
1727 studies. *Clim Past* 12, 2127-2143.

1728 Dredge, J., Fairchild, I.J., Harrison, R.M., Fernandez-Cortes, A., Sanchez-Moral, S., Jurado, V., Gunn, J.,
1729 Smith, A., Spotl, C., Matthey, D., Wynn, P.M., Grassineau, N., 2013. Cave aerosols: distribution and
1730 contribution to speleothem geochemistry. *Quaternary Sci. Rev.* 63, 23-41.

1731 Dreybrodt, W., 1980. Deposition of calcite from thin films of natural calcareous solutions and the
1732 growth of speleothems. *Chem. Geol.* 29, 89-105.

- 1733 Dreybrodt, W., 1988. Processes in karst systems - physics, chemistry and geology. Springer, Berlin,
1734 New York.
- 1735 Dreybrodt, W., 1999. Chemical kinetics, speleothem growth and climate. *Boreas* 28, 347-356.
- 1736 Dreybrodt, W., Deininger, M., 2014. The impact of evaporation to the isotope composition of DIC in
1737 calcite precipitating water films in equilibrium and kinetic fractionation models. *Geochim.*
1738 *Cosmochim. Acta* 125, 433-439.
- 1739 Duan, F.C., Wu, J.Y., Wang, Y.J., Edwards, R.L., Cheng, H., Kong, X.G., Zhang, W.H., 2015. A 3000-yr
1740 annually laminated stalagmite record of the Last Glacial Maximum from Hulu Cave, China.
1741 *Quaternary Res.* 83, 360-369.
- 1742 Duan, W., Ruan, J., Luo, W., Li, T., Tian, L., Zeng, G., Zhang, D., Bai, Y., Li, J., Tao, T., Zhang, P., Baker,
1743 A., Tan, M., 2016. The transfer of seasonal isotopic variability between precipitation and drip water
1744 at eight caves in the monsoon regions of China. *Geochim. Cosmochim. Acta* 183, 250-266.
- 1745 Edwards, L.R., Chen, J.H., Wasserburg, G.J., 1987. ^{238}U - ^{234}U - ^{230}Th - ^{232}Th systematics and the
1746 precise measurement of time over the past 500,000 years. *Earth Planet. Sci. Lett.* 81, 175-192.
- 1747 Edwards, R.L., Gallup, C.D., 1993. Dating of the Devils Hole Calcite Vein. *Science* 259, 1626-1627.
- 1748 Emiliani, C., 1955. Pleistocene temperatures. *Journal of Geology* 63, 538-578.
- 1749 Epstein, S., Buchsbaum, R., Lowenstam, H.A., Urey, H.C., 1951. Carbonate-water isotopic
1750 temperature scale. *Bulletin of the Geological Society of America* 62, 417-427.
- 1751 Evans, D., Müller, W., 2013. LA-ICPMS elemental imaging of complex discontinuous carbonates: An
1752 example using large benthic foraminifera. *J. Anal. At. Spectrom.* 28, 1039-1044.
- 1753 Evans, M.N., Tolwinski-Ward, S.E., Thompson, D.M., Achukaitis, K.J., 2013. Applications of proxy
1754 system modeling in high resolution paleoclimatology. *Quaternary Science Reviews* 76, 16-28.

1755 Faimon, J., Lang, M., 2013. Variances in airflows during different ventilation modes in a dynamic U-
1756 shaped cave. *Int J Speleol* 42, 115-122.

1757 Fairchild, I.J., Baker, A., 2012. *Speleothem Science: From Processes to Past Environments*. Wiley-
1758 Blackwell, Chichester, UK.

1759 Fairchild, I.J., Baker, A., Borsato, A., Frisia, S., Hinton, R.W., McDermott, F., Tooth, A.F., 2001. Annual
1760 to sub-annual resolution of multiple trace-element trends in speleothems. *Journal of the Geological*
1761 *Society of London* 158, 831-841.

1762 Fairchild, I.J., Borsato, A., Tooth, A.F., Frisia, S., Hawkesworth, C.J., Huang, Y., McDermott, F., Spiro,
1763 B., 2000. Controls on trace element (Sr-Mg) compositions of carbonate cave waters: implications for
1764 speleothem climatic records. *Chem. Geol.* 166, 255-269.

1765 Fairchild, I.J., Hartland, A., 2010. Trace element variations in stalagmites: controls by climate and by
1766 karst system processes. *EMU Notes in Mineralogy* 10, 259-287.

1767 Fairchild, I.J., Smith, C.L., Baker, A., Fuller, L., Spotl, C., Matthey, D., McDermott, F., Eimp, 2006.
1768 Modification and preservation of environmental signals in speleothems. *Earth Sci. Rev.* 75, 105-153.

1769 Fairchild, I.J., Treble, P.C., 2009. Trace elements in speleothems as recorders of environmental
1770 change. *Quaternary Science Reviews* 28, 449-468.

1771 Feng, W., Casteel, R.C., Banner, J.L., Heinze-Fry, A., 2014. Oxygen isotope variations in rainfall, drip-
1772 water and speleothem calcite from a well-ventilated cave in Texas, USA: Assessing a new
1773 speleothem temperature proxy. *Geochim. Cosmochim. Acta* 127, 233-250.

1774 Feng, X., Porporato, A., Rodriguez-Iturbe, I., 2013. Changes in rainfall seasonality in the tropics.
1775 *Nature Climate Change* 3, 811-815.

- 1776 Fick, S.E., Hijmans, R.J., 2017. WorldClim 2: new 1-km spatial resolution climate surfaces for global
1777 land areas. *Int J Climatol* 37, 4302-4315.
- 1778 Finch, A.A., Shaw, P.A., Weedon, G.P., Holmgren, K., 2001. Trace element variation in speleothem
1779 aragonite: potential for palaeoenvironmental reconstruction. *Earth Planet. Sci. Lett.* 186, 255-267.
- 1780 Fohlmeister, J., Lechleitner, F.A., 2019. STAlagmite dating by radiocarbon (star): A software tool for
1781 reliable and fast age depth modelling. *Quat Geochronol* 51, 120-129.
- 1782 Fohlmeister, J., Plessen, B., Dudashvili, A.S., Tjallingii, R., Wolff, C., Gafurov, A., Cheng, H., 2017.
1783 Winter precipitation changes during the Medieval Climate Anomaly and the Little Ice Age in arid
1784 Central Asia. *Quaternary Science Reviews* 178, 24-36.
- 1785 Frappier, A., Sahagian, D., González, L.A., Carpenter, S.J., 2002. El Niño Events Recorded by
1786 Stalagmite Carbon Isotopes. *Science* 298, 565-565.
- 1787 Frappier, A.B., Sahagian, D., Carpenter, S.J., González, L.A., Frappier, B.R., 2007. Stalagmite stable
1788 isotope record of recent tropical cyclone events. *Geology* 35.
- 1789 Frick, D.A., Schuessler, J.A., von Blanckenburg, F., 2016. Development of routines for simultaneous in
1790 situ chemical composition and stable Si isotope ratio analysis by femtosecond laser ablation
1791 inductively coupled plasma mass spectrometry. *Analytica Chimica Acta* 938, 33-43.
- 1792 Frisia, S., 2015. Microstratigraphic logging of calcite fabrics in speleothems as tool for palaeoclimate
1793 studies. *Int J Speleol* 44, 1-16.
- 1794 Frisia, S., Borsato, A., Fairchild, I.J., McDermott, F., 2000. Calcite fabrics, growth mechanisms, and
1795 environments of formation in speleothems from the Italian Alps and southwestern Ireland. *J*
1796 *Sediment Res* 70, 1183-1196.

- 1797 Frisia, S., Borsato, A., Fairchild, I.J., Susini, J., 2005. Variations in atmospheric sulphate recorded in
1798 stalagmites by synchrotron micro-XU and XANES analyses. *Earth Planet. Sci. Lett.* 235, 729-740.
- 1799 Frisia, S., Borsato, A., Hellstrom, J., 2018. High spatial resolution investigation of nucleation, growth
1800 and early diagenesis in speleothems as exemplar for sedimentary carbonates. *Earth Sci. Rev.* 178, 68-
1801 91.
- 1802 Frisia, S., Borsato, A., Susini, J., 2008. Synchrotron radiation applications to past volcanism archived
1803 in speleothems: An overview. *J. Volcanol. Geotherm. Res.* 177, 96-100.
- 1804 Gascoyne, M., Schwarcz, H.P., Ford, D.C., 1980. A palaeotemperature record for the mid-Wisconsin
1805 in Vancouver Island. *Nature* 285, 474-476.
- 1806 Gazis, C., Feng, X.H., 2004. A stable isotope study of soil water: evidence for mixing and preferential
1807 flow paths. *Geoderma* 119, 97-111.
- 1808 Genty, D., 2008. Palaeoclimate research in Villars Cave (Dordogne, SW France). *Int J Speleol* 37, 173-
1809 191.
- 1810 Genty, D., Baker, A., Vokal, B., 2001. Intra- and inter-annual growth rate of modern stalagmites.
1811 *Chemical Geology* 176, 191-212.
- 1812 Genty, D., Deflandre, G., 1998. Drip flow variations under a stalactite of the Père Noël cave
1813 (Belgium). Evidence of seasonal variations and air pressure constraints. *J Hydrol* 211, 208-232.
- 1814 Guo, W., Zhou, C., 2019. Patterns and controls of disequilibrium isotope effects in speleothems:
1815 Insights from an isotope-enabled diffusion-reaction model and implications for quantitative
1816 thermometry. *Geochimica et Cosmochimica Acta* 267, 196-226.
- 1817 Harmon, R.S., 1979. An isotopic study of groundwater seepage in the Central Kentucky karst. *Water*
1818 *Resources Research* 15, 476.

1819 Hartland, A., Fairchild, I.J., Lead, J.R., 2009. Colloids in karstic percolation waters: Implications for the
1820 interpretation of trace element variations in speleothems. *Geochim. Cosmochim. Acta* 73, A498-
1821 A498.

1822 Hartland, A., Fairchild, I.J., Lead, J.R., Baker, A., 2010. Fluorescent properties of organic carbon in
1823 cave dripwaters: Effects of filtration, temperature and pH. *Sci. Total Environ.* 408, 5940-5950.

1824 Hartland, A., Fairchild, I.J., Lead, J.R., Borsato, A., Baker, A., Frisia, S., Baalousha, M., 2012. From soil
1825 to cave: Transport of trace metals by natural organic matter in karst dripwaters. *Chem. Geol.* 304,
1826 68-82.

1827 Hartland, A., Fairchild, I.J., Lead, J.R., Zhang, H., Baalousha, M., 2011. Size, speciation and lability of
1828 NOM-metal complexes in hyperalkaline cave dripwater. *Geochim. Cosmochim. Acta* 75, 7533-7551.

1829 Hellstrom, J., 2003. Rapid and accurate U/Th dating using parallel ion-counting multi-collector ICP-
1830 MS. *J. Anal. At. Spectrom.* 18, 1346-1351.

1831 Helser, T.E., Kestelle, C.R., McKay, J.L., Orland, I.J., Kodzon, R., Valley, J.W., 2018. Evaluation of
1832 micromilling/conventional isotope ratio mass spectrometry and secondary ion mass spectrometry of
1833 $\delta^{18}\text{O}$ values in fish otoliths for sclerochronology. *Rapid Commun Mass Spectrom* 32, 1781-1790.

1834 Hendy, C.H., Wilson, A.T., 1968. Paleoclimatic data from speleothems. *Nature* 216, 48-51.

1835 Hess, J.W., White, W.B., 1989. Water Budget and Physical Hydrology, in: B., W.W., White, E.L. (Eds.),
1836 *Karst Hydrology: Concepts from the Mammoth Cave Area*. Springer-Verlag, Boston, pp. 105-126.

1837 Hoffmann, D.L., Prytulak, J., Richards, D.A., Elliott, T.R., Coath, C.D., Smart, P.L., Scholz, D., 2007.
1838 Procedures for accurate U and Th isotope measurements by high precision MC-ICPMS. *Int. J. Mass*
1839 *Spectrom. Ion Processes* 264, 97-109.

1840 Hsiang, S.M., Burke, M., Miguel, E., 2013. Quantifying the Influence of Climate on Human Conflict.
1841 Science 341, 1235367.

1842 Hu, C., Henderson, G.M., Huang, J., Xie, S., Sun, Y., Johnson, K.R., 2008. Quantification of Holocene
1843 Asian monsoon rainfall from spatially separated cave records. Earth Planet. Sci. Lett. 266, 221-232.

1844 Huang, S.P., Pollack, H.N., Shen, P.Y., 2000. Temperature trends over the past five centuries
1845 reconstructed from borehole temperatures. Nature 403, 756-758.

1846 Huang, Y., Fairchild, I.J., 2001. Partitioning of Sr^{2+} and Mg^{2+} into calcite under karst-analogue
1847 experimental conditions. Geochim. Cosmochim. Acta 65, 47-62.

1848 Huang, Y., Fairchild, I.J., Borsato, A., Frisia, S., Cassidy, N.J., McDermott, F., Hawkesworth, C.J., 2001.
1849 Seasonal variations in Sr, Mg and P in modern speleothems (Grotta di Ernesto, Italy). Chem. Geol.
1850 175, 429-448.

1851 IAEA, 2001. GNIP Maps and Animations. , Vienna.

1852 IAEA/WMO, 2001. Global Network of Isotopes in Precipitation. The GNIP Database.

1853 James, E., Banner, J., Hardt, B., 2015. A global model for cave ventilation and seasonal bias in
1854 speleothem paleoclimate records.

1855 Jamieson, R.A., Baldini, J.U.L., Brett, M.J., Taylor, J., Ridley, H.E., Ottley, C.J., Prufer, K.M.,
1856 Wassenburg, J.A., Scholz, D., Breitenbach, S.F.M., 2016. Intra- and inter-annual uranium
1857 concentration variability in a Belizean stalagmite controlled by prior aragonite precipitation: A new
1858 tool for reconstructing hydro-climate using aragonitic speleothems. Geochim. Cosmochim. Acta 190,
1859 332-346.

1860 Jamieson, R.A., Baldini, J.U.L., Frappier, A.B., Muller, W., 2015. Volcanic ash fall events identified
1861 using principle component analysis of a high-resolution speleothem trace element dataset. *Earth*
1862 *Planet. Sci. Lett.* 426, 36-45.

1863 Johnson, K.R., Hu, C., Belshaw, N.S., Henderson, G.M., 2006. Seasonal trace-element and stable-
1864 isotope variations in a Chinese speleothem: The potential for high-resolution paleomonsoon
1865 reconstruction. *Earth Planet. Sci. Lett.* 244, 394-407.

1866 Kaufman, A., Bar-Matthews, M., Ayalon, A., Carmi, I., 2003. The vadose flow above Soreq Cave,
1867 Israel: a tritium study of the cave waters. *Journal of Hydrology* 273, 155-163.

1868 Kennett, D.J., Breitenbach, S.F.M., Aquino, V.V., Asmerom, Y., Awe, J., Baldini, J.U.L., Bartlein, P.,
1869 Culleton, B.J., Ebert, C., Jazwa, C., Macri, M.J., Marwan, N., Polyak, V., Prufer, K.M., Ridley, H.E.,
1870 Sodemann, H., Winterhalder, B., Haug, G.H., 2012. Development and Disintegration of Maya Political
1871 Systems in Response to Climate Change. *Science* 338, 788-791.

1872 Khiewtam, R.S., Ramakrishnan, P.S., 1993. Litter and fine root dynamics of a relict sacred grove
1873 forest at Cherrapunji in north-eastern India. *Forest Ecology and Management* 60, 327-344.

1874 Kita, N.T., Huberty, J.M., Kozdon, R., Beard, B.L., Valley, J.W., 2011. High-precision SIMS oxygen,
1875 sulfur and iron stable isotope analyses of geological materials: accuracy, surface topography and
1876 crystal orientation. *Surf. Interface Anal.* 43, 427-431.

1877 Kolodny, Y., Bar-Matthews, M., Ayalon, A., McKeegan, K.D., 2003. A high spatial resolution $\delta^{18}\text{O}$
1878 profile of a speleothem using an ion-microprobe. *Chemical Geology* 197, 21-28.

1879 Köppen, W., 1918. Classification of climates according to temperature, precipitation and course of
1880 the year. *Petermanns Mitt* 64, 193-203.

- 1881 Kuczumow, A., Genty, D., Chevallier, P., Nowak, J., Ro, C.U., 2003. Annual resolution analysis of a
1882 SW-France stalagmite by X-ray synchrotron microprobe analysis. *Spectrochim Acta B* 58, 851-865.
- 1883 Kuczumow, A., Vekemans, B., Schalm, O., Gysels, K., Ro, C.U., Van Grieken, R., 2001. Analysis of
1884 speleothems by electron and X-ray microprobes. *J. Anal. At. Spectrom.* 16, 90-95.
- 1885 Kylander-Clark, A.R.C., Hacker, B.R., Cottle, J.M., 2013. Laser-ablation split-stream ICP
1886 petrochronology. *Chemical Geology* 345, 99-112.
- 1887 Lachniet, M.S., 2009. Climatic and environmental controls on speleothem oxygen-isotope values.
1888 *Quaternary Science Reviews* 28, 412-432.
- 1889 Lauritzen, S., 1995. High Resolution Paleotemperature Proxy Record for the Last Interglaciation
1890 Based on Norwegian Speleothems. *Quaternary Res.* 43, 133-146.
- 1891 Lauritzen, S., Lundberg, J., 1999. Calibration of the speleothem delta function: an absolute
1892 temperature record for the Holocene in northern Norway. *Holocene* 9, 659-669.
- 1893 Lechleitner, F.A., Baldini, J.U.L., Breitenbach, S.F.M., Fohlmeister, J., McIntyre, C., Goswami, B.,
1894 Jamieson, R.A., van der Voort, T.S., Prufer, K., Marwan, N., Culleton, B.J., Kennett, D.J., Asmerom, Y.,
1895 Polyak, V., Eglinton, T.I., 2016a. Hydrological and climatological controls on radiocarbon
1896 concentrations in a tropical stalagmite. *Geochim. Cosmochim. Acta* 194, 233-252.
- 1897 Lechleitner, F.A., Fohlmeister, J., McIntyre, C., Baldini, L.M., Jamieson, R.A., Hercman, H.,
1898 Gąsiorowski, M., Pawlak, J., Stefaniak, K., Socha, P., Eglinton, T.I., Baldini, J.U.L., 2016b. A novel
1899 approach for construction of radiocarbon-based chronologies for speleothems. *Quaternary*
1900 *Geochronology* 35, 54-66.
- 1901 Li, F., Vanwezer, N., Boivin, N., Gao, X., Ott, F., Petraglia, M., Roberts, P., 2019. Heading north: Late
1902 Pleistocene environments and human dispersals in central and eastern Asia. *Plos One* 14, e0216433.

1903 Linzmeier, B.J., Kitajima, K., Denny, A.C., Cammack, J.N., 2018. Making maps on a micrometer scale.
1904 Eos 99.

1905 Liu, Y., Tang, G., Ling, X., Hu, C., Li, X., 2015. Speleothem annual layers revealed by seasonal SIMS
1906 $\delta^{18}O$ measurements. Science China Earth Sciences 58, 1741-1747.

1907 Liu, Y.H., Henderson, G.M., Hu, C.Y., Mason, A.J., Charnley, N., Johnson, K.R., Xie, S.C., 2013. Links
1908 between the East Asian monsoon and North Atlantic climate during the 8,200 year event. Nat.
1909 Geosci. 6, 117-120.

1910 Luetscher, M., Boch, R., Sodemann, H., Spotl, C., Cheng, H., Edwards, R.L., Frisia, S., Hof, F., Müller,
1911 W., 2015. North Atlantic storm track changes during the Last Glacial Maximum recorded by Alpine
1912 speleothems. Nat Commun 6, 6344.

1913 Luo, T., Hu, Z., Zhang, W., Günther, D., Liu, Y., Zong, K., Hu, S., 2018. Reassessment of the influence
1914 of carrier gases He and Ar on signal intensities in 193 nm excimer LA-ICP-MS analysis. Journal of
1915 Analytical Atomic Spectrometry 33, 1655-1663.

1916 Luo, W., Wang, S., Zeng, G., Zhu, X., Liu, W., 2014. Daily response of drip water isotopes to
1917 precipitation in Liangfeng Cave, Guizhou Province, SW China. Quaternary International 349, 153-158.

1918 Markowska, M., Baker, A., Andersen, M.S., Jex, C.N., Cuthbert, M.O., Rau, G.C., Graham, P.W.,
1919 Rutledge, H., Mariethoz, G., Marjo, C.E., Treble, P.C., Edwards, N., 2016. Semi-arid zone caves:
1920 Evaporation and hydrological controls on delta O-18 drip water composition and implications for
1921 speleothem paleoclimate reconstructions. Quaternary Sci. Rev. 131, 285-301.

1922 Markowska, M., Baker, A., Treble, P.C., Andersen, M.S., Hankin, S., Jex, C.N., Tadros, C.V., Roach, R.,
1923 2015. Unsaturated zone hydrology and cave drip discharge water response: Implications for
1924 speleothem paleoclimate record variability. J Hydrol 529, 662-675.

- 1925 Markowska, M., Fohlmeister, J., Treble, P.C., Baker, A., Andersen, M.S., Hua, Q., 2019. Modelling the
1926 ¹⁴C bomb-pulse in young speleothems using a soil carbon continuum model. *Geochim. Cosmochim.*
1927 *Acta* 261, 342-367.
- 1928 Martin-Chivelet, J., Munoz-Garcia, M.B., Edwards, R.L., Turrero, M.J., Ortega, A.I., 2011. Land surface
1929 temperature changes in Northern Iberia since 4000 yr BP, based on delta C-13 of speleothems.
1930 *Global and Planet. Change* 77, 1-12.
- 1931 Martin-Garcia, R., Alonso-Zarza, A.M., Martin-Perez, A., Schroder-Ritzrau, A., Ludwig, T., 2014.
1932 Relationships between colour and diagenesis in the aragonite-calcite speleothems in Basajaun Etxea
1933 cave, Spain. *Sediment Geol* 312, 63-75.
- 1934 Matthey, D., Collister, C., 2008. Controls on water drop volume at speleothem drip sites: An
1935 experimental study. *J Hydrol* 358, 259-267.
- 1936 Matthey, D., Lowry, D., Duffet, J., Fisher, R., Hodge, E., Frisia, S., 2008. A 53 year seasonally resolved
1937 oxygen and carbon isotope record from a modern Gibraltar speleothem: Reconstructed drip water
1938 and relationship to local precipitation. *Earth Planet. Sci. Lett.* 269, 80-95.
- 1939 Matthey, D.P., Atkinson, T.C., Barker, J.A., Fisher, R., Latin, J.P., Durell, R., Ainsworth, M., 2016. Carbon
1940 dioxide, ground air and carbon cycling in Gibraltar karst. *Geochim. Cosmochim. Acta* 184, 88-113.
- 1941 Matthey, D.P., Fairchild, I.J., Atkinson, T.C., 2009. Seasonal microclimate control on calcite fabrics,
1942 stable isotopes and trace elements in modern speleothem from St. Michaels Cave, Gibraltar.
1943 *Geochim. Cosmochim. Acta* 73, A849-A849.
- 1944 Matthey, D.P., Fairchild, I.J., Atkinson, T.C., Latin, J.-P., Ainsworth, M., Durell, R., 2010. Seasonal
1945 microclimate control of calcite fabrics, stable isotopes and trace elements in modern speleothem
1946 from St Michaels cave, Gibraltar in: Pedley, H.M., Rogerson, M. (Eds.), *Tufas and Speleothems:*

- 1947 Unravelling the Microbial and Physical Controls. Geological Society of London Special Publication,
1948 London, pp. 323-344.
- 1949 Maupin, C.R., Partin, J.W., Shen, C.C., Quinn, T.M., Lin, K., Taylor, F.W., Banner, J.L., Thirumalai, K.,
1950 Sinclair, D.J., 2014. Persistent decadal-scale rainfall variability in the tropical South Pacific
1951 Convergence Zone through the past six centuries. *Clim Past* 10, 1319-1332.
- 1952 McDermott, F., 2004. Palaeo-climate reconstruction from stable isotope variations in speleothems: a
1953 review. *Quaternary Sci. Rev.* 23, 901-918.
- 1954 McDermott, F., Atkinson, T.C., Fairchild, I.J., Baldini, L.M., Matthey, D.P., 2011. A first evaluation of the
1955 spatial gradients in delta O-18 recorded by European Holocene speleothems. *Global and Planet.*
1956 *Change* 79, 275-287.
- 1957 McMillan, E.A., Fairchild, I.J., Frisia, S., Borsato, A., McDermott, F., 2005. Annual trace element cycles
1958 in calcite-aragonite speleothems: evidence of drought in the western Mediterranean 1200-1100 yr
1959 BP. *J. of Quaternary Sci.* 20, 423-433.
- 1960 Menne, M.J., Durre, I., Vose, R.S., Gleason, B.E., Houston, T.G., 2012. An Overview of the Global
1961 Historical Climatology Network-Daily Database. *J Atmos Ocean Tech* 29, 897-910.
- 1962 Mickler, P.J., Stern, L.A., Banner, J.L., 2006. Large kinetic isotope effects in modern speleothems.
1963 *Geol. Soc. Am. Bull.* 118, 65-81.
- 1964 Millo, C., Strikis, N.M., Vonhof, H.B., Deininger, M., da Cruz, F.W., Wang, X.F., Cheng, H., Edwards,
1965 R.L., 2017. Last glacial and Holocene stable isotope record of fossil dripwater from subtropical Brazil
1966 based on analysis of fluid inclusions in stalagmites. *Chem. Geol.* 468, 84-96.
- 1967 Mischel, S.A., Scholz, D., Spötl, C., 2015. $\delta^{18}\text{O}$ values of cave drip water: a promising proxy for the
1968 reconstruction of the North Atlantic Oscillation? *Climate Dynamics* 45, 3035-3050.

- 1969 Moerman, J.W., Cobb, K.M., Partin, J.W., Meckler, A.N., Carolin, S.A., Adkins, J.F., Lejau, S., Malang,
1970 J., Clark, B., Tuen, A.A., 2014. Transformation of ENSO-related rainwater to dripwater $\delta^{18}\text{O}$
1971 variability by vadose water mixing. *Geophys Res Lett* 41, 7907-7915.
- 1972 Moquet, J.S., Cruz, F.W., Novello, V.F., Strikis, N.M., Deininger, M., Karmann, I., Santos, R.V., Millo,
1973 C., Apaestegui, J., Guyot, J.L., Siffedine, A., Vuille, M., Cheng, H., Edwards, R.L., Santini, W., 2016.
1974 Calibration of speleothem delta O-18 records against hydroclimate instrumental records in Central
1975 Brazil. *Global and Planet. Change* 139, 151-164.
- 1976 Morellón, M., Valero-Garcés, B., Vegas-Villarrúbia, T., González-Sampériz, P., Romero, O., Delgado-
1977 Huertas, A., Mata, P., Moreno, A., Rico, M., Corella, J.P., 2009. Lateglacial and Holocene
1978 palaeohydrology in the western Mediterranean region: the Lake Estanya record (NE Spain).
1979 *Quaternary Science Reviews* 28, 2582-2599.
- 1980 Moreno, A., Pérez-Mejías, C., Bartolomé, M., Sancho, C., Cacho, I., Stoll, H., Delgado-Huertas, A.,
1981 Hellstrom, J., Edwards, R.L., Cheng, H., 2017. New speleothem data from Molinos and Ejulve caves
1982 reveal Holocene hydrological variability in northeast Iberia. *Quaternary Research* 88, 223-233.
- 1983 Moreno, A., Sancho, C., Bartolomé, M., Oliva-Urcia, B., Delgado-Huertas, A., Estrela, M.J., Corell, D.,
1984 López-Moreno, J.I., Cacho, I., 2014. Climate controls on rainfall isotopes and their effects on cave
1985 drip water and speleothem growth: the case of Molinos cave (Teruel, NE Spain). *Climate Dynamics*
1986 43, 221-241.
- 1987 Moseley, G.E., Spötl, C., Cheng, H., Boch, R., Min, A., Edwards, R.L., 2015. Termination-II
1988 interstadial/stadial climate change recorded in two stalagmites from the north European Alps.
1989 *Quaternary Science Reviews* 127, 229-239.
- 1990 Müller, W., Fietzke, J., 2016. The role of LA-ICP-MS in palaeoclimate research. *Elements* 12, 329-334.

1991 Müller, W., Shelley, M., Miller, P., Broude, S., 2009. Initial performance metrics of a new custom-
1992 designed ArF excimer LA-ICPMS system coupled to a two-volume laser-ablation cell. *J. Anal. At.*
1993 *Spectrom.* 24, 209-214.

1994 Müller, W., Valley, J.W., Warter, V., Kodzon, R., Evans, D., Orland, I.J., 2015. Natural high-
1995 temperature metamorphic calcite as compositionally homogenous microanalytical standard?,
1996 *Goldschmidt 2015, Prague.*

1997 Murata, F., Terao, T., Hayashi, T., Asada, H., Matsumoto, J., 2007. Relationship between atmospheric
1998 conditions at Dhaka, Bangladesh, and rainfall at Cherrapunjee, India. *Natural Hazards* 44, 399-410.

1999 Myers, C.G., Oster, J.L., Sharp, W.D., Bennartz, R., Kelley, N.P., Covey, A.K., Breitenbach, S.F.M.,
2000 2015. Northeast Indian stalagmite records Pacific decadal climate change: Implications for moisture
2001 transport and drought in India. *Geophys. Res. Lett.* 42, 4124-4132.

2002 Nagra, G., Treble, P.C., Andersen, M.S., Bajo, P., Hellstrom, J., Baker, A., 2017. Dating stalagmites in
2003 mediterranean climates using annual trace element cycles. *Sci. Rep.* 7, 621.

2004 Noronha, A.L., Johnson, K.R., Southon, J.R., Hu, C., Ruan, J., McCabe-Glynn, S., 2015. Radiocarbon
2005 evidence for decomposition of aged organic matter in the vadose zone as the main source of
2006 speleothem carbon. *Quaternary Sci. Rev.* 127, 37-47.

2007 O'Neil, J.R., Clayton, R.M., Mayeda, T., 1969. Oxygen isotope fractionation in divalent metal
2008 carbonates. *J. Chem. Phys.* 30, 5547-5558.

2009 Oerter, E.J., Sharp, W.D., Oster, J.L., Ebeling, A., Valley, J.W., Kodzon, R., Orland, I.J., Hellstrom, J.,
2010 Woodhead, J.D., Hergt, J.M., Chadwick, O.A., Amundson, R., 2016. Pedothem carbonates reveal
2011 anomalous North American atmospheric circulation 70,000–55,000 years ago. *Proc Natl Acad Sci U S*
2012 *A* 113, 919-924.

2013 Onac, B.P., Pace-Graczyk, K., Atudirei, V., 2008. Stable isotope study of precipitation and cave drip
2014 water in Florida (USA): implications for speleothem-based paleoclimate studies. *Isot. Environ. Health*
2015 *Stud.* 44, 149-161.

2016 Orland, I.J., Bar-Matthews, M., Ayalon, A., Matthews, A., Kozdon, R., Ushikubo, T., Valley, J.W., 2012.
2017 Seasonal resolution of Eastern Mediterranean climate change since 34 ka from a Soreq Cave
2018 speleothem. *Geochim. Cosmochim. Acta* 89, 240-255.

2019 Orland, I.J., Bar-Matthews, M., Kita, N.T., Ayalon, A., Matthews, A., Valley, J.W., 2008. Seasonal
2020 climate change as revealed by ion microprobe analysis of delta O-18 in Soreq Cave (Israel)
2021 speleothems. *Geochimica Et Cosmochimica Acta* 72, A709-A709.

2022 Orland, I.J., Bar-Matthews, M., Kita, N.T., Ayalon, A., Matthews, A., Valley, J.W., 2009. Climate
2023 deterioration in the Eastern Mediterranean as revealed by ion microprobe analysis of a speleothem
2024 that grew from 2.2 to 0.9 ka in Soreq Cave, Israel. *Quaternary Research* 71, 27-35.

2025 Orland, I.J., Burstyn, Y., Bar-Matthews, M., Kozdon, R., Ayalon, A., Matthews, A., Valley, J.W., 2014.
2026 Seasonal climate signals (1990-2008) in a modern Soreq Cave stalagmite as revealed by high-
2027 resolution geochemical analysis. *Chemical Geology* 363, 322-333.

2028 Orland, I.J., Edwards, R.L., Cheng, H., Kozdon, R., Cross, M., Valley, J.W., 2015. Direct measurements
2029 of deglacial monsoon strength in a Chinese stalagmite. *Geology* 43, 555-558.

2030 Orland, I.J., He, F., Bar-Matthews, M., Chen, G., Ayalon, A., Kutzbach, J.E., 2019. Resolving seasonal
2031 rainfall changes in the Middle East during the last interglacial period. *Proc Natl Acad Sci U S A* 116,
2032 24985-24990.

2033 Orland, I.J.d., 2013. Seasonality from speleothems : high-resolution ion microprobe studies at Soreq
2034 Cave, Israel. Ann Arbor, MI : ProQuest LLC, 2013.

2035 Orr, P.C., 1952. Excavations in Moaning Cave. Santa Barbara Museum of Natural History Bulletin 1, 1-
2036 19.

2037 Ortega, R., Maire, R., Deves, G., Quinif, Y., 2005. High-resolution mapping of uranium and other trace
2038 elements in recrystallized aragonite-calcite speleothems from caves in the Pyrenees (France):
2039 Implications for U-series dating. Earth Planet. Sci. Lett. 237, 911-023.

2040 Oster, J.L., Montañez, I.P., Kelley, N.P., 2012. Response of a modern cave system to large seasonal
2041 precipitation variability. Geochim. Cosmochim. Acta 91, 92-108.

2042 Pacton, M., Breitenbach, S.F.M., Lechleitner, F.A., Vaks, A., Rollion-Bard, C., Gutareva, O.S., Osintcev,
2043 A.V., Vasconcelos, C., 2013. The role of microorganisms in the formation of a stalactite in Botovskaya
2044 Cave, Siberia – paleoenvironmental implications. Biogeosciences 10, 6115-6130.

2045 Parton, A., Farrant, A.R., Leng, M.J., Telfer, M.W., Groucutt, H.S., Petraglia, M.D., Parker, A.G., 2015.
2046 Alluvial fan records from southeast Arabia reveal multiple windows for human dispersal. Geol. 43,
2047 295-298.

2048 Peel, M.C., Finlayson, B.L., McMahon, T.A., 2007. Updated world map of the Köppen-Geiger climate
2049 classification. Hydrology and Earth System Sciences 11, 1633-1644.

2050 Perrin, J., Jeannin, P.-Y., Zwahlen, F., 2003. Epikarst storage in a karst aquifer: a conceptual model
2051 based on isotopic data, Milandre test site, Switzerland. Journal of Hydrology 279, 106-124.

2052 Prokop, P., Walanus, A., 2003. Trends and periodicity in the longest instrumental rainfall series for
2053 the area of most extreme rainfall in the world, northeast India. Geographia Polonica 76, 25-35.

2054 Pu, J., Wang, A., Shen, L., Yin, J., Yuan, D., Zhao, H., 2016. Factors controlling the growth rate, carbon
2055 and oxygen isotope variation in modern calcite precipitation in a subtropical cave, Southwest China.
2056 Journal of Asian Earth Sciences 119, 167-178.

2057 Railsback, L.B., 2018. A comparison of growth rate of late Holocene stalagmites with atmospheric
2058 precipitation and temperature, and its implications for paleoclimatology. *Quaternary Science*
2059 *Reviews* 187, 94-111.

2060 Railsback, L.B., Brook, G.A., Chen, J., Kalin, R., Fleisher, C., 1994. Environmental controls on the
2061 petrology of a late Holocene speleothem from Botswana with annual layers of aragonite and calcite.
2062 *J Sediment Res A*64, 147-155.

2063 Railsback, L.B., Liang, F.Y., Romani, J.R.V., Grandal-d'Anglade, A., Rodriguez, M.V., Fidalgo, L.S.,
2064 Mosquera, D.F., Cheng, H., Edwards, R.L., 2011. Petrographic and isotopic evidence for Holocene
2065 long-term climate change and shorter-term environmental shifts from a stalagmite from the Serra
2066 do Courel of northwestern Spain, and implications for climatic history across Europe and the
2067 Mediterranean. *Palaeogeography Palaeoc.* 305, 172-184.

2068 Railsback, L.B., Liang, F.Y., Vidal-Romani, J.R., Garrett, K.B., Sellers, R.C., Vaqueiro-Rodriguez, M.,
2069 Grandal-d'Anglade, A., Cheng, H., Edwards, R.L., 2017. Radiometric, isotopic, and petrographic
2070 evidence of changing interglacials over the past 550,000 years from six stalagmites from the Serra do
2071 Courel in the Cordillera Cantabrica of northwestern Spain. *Palaeogeography Palaeoc.* 466, 137-152.

2072 Ramakrishnan, P.S., Subhash, C.R., 1988. Vegetation, biomass and productivity of seral grasslands of
2073 Cherrapunji in north-east India. *Vegetatio* 74, 47-53.

2074 Ridley, H., Baldini, J., Prufer, K., Walczak, I., Breitenbach, S., 2015a. High-resolution monitoring of Yok
2075 Balum Cave, Belize: An investigation of seasonal ventilation regimes and the atmospheric and drip-
2076 flow response to a local earthquake. *Journal of Cave and Karst Studies* 77, 183-199.

2077 Ridley, H.E., Asmerom, Y., Baldini, J.U.L., Breitenbach, S.F.M., Aquino, V.V., Prufer, K.M., Culleton,
2078 B.J., Polyak, V., Lechleitner, F.A., Kennett, D.J., Zhang, M., Marwan, N., Macpherson, C.G., Baldini,

2079 L.M., Xiao, T., Peterkin, J.L., Awe, J., Haug, G.H., 2015b. Aerosol forcing of the position of the
2080 intertropical convergence zone since AD1550. *Nat. Geosci.* 8, 195–200.

2081 Riechelmann, D.F.C., Deininger, M., Scholz, D., Riechelmann, S., Schroder-Ritzrau, A., Spotl, C.,
2082 Richter, D.K., Mangini, A., Immenhauser, A., 2013. Disequilibrium carbon and oxygen isotope
2083 fractionation in recent cave calcite: Comparison of cave precipitates and model data. *Geochim.*
2084 *Cosmochim. Acta* 103, 232-244.

2085 Riechelmann, D.F.C., Schroder-Ritzrau, A., Scholz, D., Fohlmeister, J., Spotl, C., Richter, D.K., Mangini,
2086 A., 2011. Monitoring Bunker Cave (NW Germany): A prerequisite to interpret geochemical proxy
2087 data of speleothems from this site. *J Hydrol* 409, 682-695.

2088 Riechelmann, S., Breitenbach, S.F.M., Schroder-Ritzrau, A., Mangini, A., Immenhauser, A., 2019.
2089 Ventilation and Cave Air PCO₂ in the Bunker-Emst Cave System (NW Germany): Implications for
2090 Speleothem Proxy Data. *J Cave Karst Stud* 81, 98-112.

2091 Riechelmann, S., Schröder-Ritzrau, A., Spötl, C., Riechelmann, D.F.C., Richter, D.K., Mangini, A.,
2092 Frank, N., Breitenbach, S.F.M., Immenhauser, A., 2017. Sensitivity of Bunker Cave to climatic forcings
2093 highlighted through multi-annual monitoring of rain-, soil-, and dripwaters. *Chemical Geology* 449,
2094 194-205.

2095 Rittner, M., Muller, W., 2012. 2D mapping of LA-ICPMS trace element distributions using R.
2096 *Computers & Geosciences* 42, 152-161.

2097 Roberts, M.S., Smart, P.L., Baker, A., 1998. Annual trace element variations in a Holocene
2098 speleothem. *Earth Planet. Sci. Lett.* 154, 237-246.

2099 Ronay, E.R., Breitenbach, S.F.M., Oster, J.L., 2019. Sensitivity of speleothem records in the Indian
2100 Summer Monsoon region to dry season infiltration. *Sci Rep* 9, 5091.

2101 Sade, Z., Halevy, I., 2017. New constraints on kinetic isotope effects during CO₂(aq) hydration and
2102 hydroxylation: Revisiting theoretical and experimental data. *Geochim. Cosmochim. Acta* 214, 246-
2103 265.

2104 Santer, B.D., Po-Chedley, S., Zelinka, M.D., Cvijanovic, I., Bonfils, C., Durack, P.J., Fu, Q., Kiehl, J.,
2105 Mears, C., Painter, J., Pallotta, G., Solomon, S., Wentz, F.J., Zou, C.-Z., 2018. Human influence on the
2106 seasonal cycle of tropospheric temperature. *Science* 361, eaas8806.

2107 Schubert, B.A., Jahren, A.H., 2015. Seasonal temperature and precipitation recorded in the intra-
2108 annual oxygen isotope pattern of meteoric water and tree-ring cellulose. *Quaternary Science*
2109 *Reviews* 125, 1-14.

2110 Schwarz, K., Barth, J.A.C., Postigo-Rebollo, C., Grathwohl, P., 2009. Mixing and transport of water in a
2111 karst catchment: a case study from precipitation via seepage to the spring. *Hydrology and Earth*
2112 *System Sciences* 13, 285-292.

2113 Scropton, N., Burns, S.J., Dawson, P., Rhodes, J.M., Brent, K., McGee, D., Heijnis, H., Gadd, P.,
2114 Hantoro, W., Gagan, M., 2018. Rapid measurement of strontium in speleothems using core-scanning
2115 micro X-ray fluorescence. *Chemical Geology* 487, 12-22.

2116 Shen, C.C., Lin, K., Duan, W., Jiang, X., Partin, J.W., Edwards, R.L., Cheng, H., Tan, M., 2013. Testing
2117 the annual nature of speleothem banding. *Sci Rep* 3, 2633.

2118 Sherwin, C.M., Baldini, J.U.L., 2011. Cave air and hydrological controls on prior calcite precipitation
2119 and stalagmite growth rates: Implications for palaeoclimate reconstructions using speleothems.
2120 *Geochimica et Cosmochimica Acta* 75, 3915-3929.

2121 Shopov, Y.Y., Ford, D.C., Schwarcz, H.P., 1994. Luminescent microbanding in speleothems - high-
2122 resolution chronology and paleoclimate. *Geol.* 22, 407-410.

2123 Sliwinski, M.G., Kitajima, K., Kodzon, R., Spicuzza, M., Denny, A., Valley, J.W., 2017. In situ $\delta^{13}\text{C}$ and
2124 $\delta^{18}\text{O}$ microanalysis by SIMS: A method for characterizing the carbonate components of natural and
2125 engineered CO_2 -reservoirs. *International Journal of Greenhouse Gas Control* 57, 116-133.

2126 Sliwinski, M.G., Kodzon, R., Kitajima, K., Denny, A., Spicuzza, M., Valley, J.W., 2015. In-Situ, Micron-
2127 Scale $\delta^{13}\text{C}$ & $\delta^{18}\text{O}$ Analyses (by SIMS) of Chemo-Isotopically Zoned Carbonate Cements of
2128 Diagenetic Origin—A Case Study on the Implications for the Thermal and Burial History of the Eau
2129 Claire Fm., Illinois Basin (USA). AAPG Annual Convention and Exhibition.

2130 Smart, P.L., Friedrich, H., 1987. Water movement and storage in the unsaturated zone of a maturely
2131 karstified aquifer, Mendip Hills, England, The conference on environmental problems in karst
2132 terrains and their solution. National Water Well Association, Bowling Green, Kentucky, pp. 57-87.

2133 Smith, C.L., Fairchild, I.J., Spotl, C., Frisia, S., Borsato, A., Moreton, S.G., Wynn, P.M., 2009.
2134 Chronology building using objective identification of annual signals in trace element profiles of
2135 stalagmites. *Quat Geochronol* 4, 11-21.

2136 Spengler, R.N., 2019. *Fruit from the Sands: The Silk Road Origins of the Foods We Eat*, 1 ed.
2137 University of California Press, Oakland, California.

2138 Spötl, C., Fairchild, I.J., Tooth, A.F., 2005. Cave air control on dripwater geochemistry, Obir Caves
2139 (Austria): implications for speleothem deposition in dynamically ventilated caves. *Geochim.*
2140 *Cosmochim. Acta* 69, 2451-2468.

2141 Spötl, C., Matthey, D., 2006. Stable isotope microsampling of speleothems for palaeoenvironmental
2142 studies: A comparison of microdrill, micromill and laser ablation techniques. *Chem. Geol.* 235, 48-58.

2143 Stoll, H., Mendez-Vicente, A., Gonzalez-Lemos, S., Moreno, A., Cacho, I., Cheng, H., Edwards, R.L.,
2144 2015. Interpretation of orbital scale variability in mid-latitude speleothem $\delta^{18}\text{O}$: Significance of
2145 growth rate controlled kinetic fractionation effects. *Quaternary Science Reviews* 127, 215-228.

2146 Stoll, H.M., Müller, W., Prieto, M., 2012. I-STAL, a model for interpretation of Mg/Ca, Sr/Ca and
2147 Ba/Ca variations in speleothems and its forward and inverse application on seasonal to millennial
2148 scales. *Geochemistry Geophysics Geosystems* 13, 09004.

2149 Surić, M., Lončarić, R., Lončar, N., Buzjak, N., Bajo, P., Drysdale, R.N., 2017. Isotopic characterization
2150 of cave environments at varying altitudes on the eastern Adriatic coast (Croatia) – Implications for
2151 future speleothem-based studies. *Journal of Hydrology* 545, 367-380.

2152 Tabersky, D., Nishiguchi, K., Utani, K., Ohata, M., Dietiker, R., Fricker, M.B., de Maddalena, I.M.,
2153 Koch, J., Gunther, D., 2013. Aerosol entrainment and a large-capacity gas exchange device (Q-GED)
2154 for laser ablation inductively coupled plasma mass spectrometry in atmospheric pressure air. *J. Anal.*
2155 *At. Spectrom.* 28, 831-842.

2156 Tadros, C.V., Treble, P.C., Baker, A., Fairchild, I., Hankin, S., Roach, R., Markowska, M., McDonald, J.,
2157 2016. ENSO-cave drip water hydrochemical relationship: a 7-year dataset from south-eastern
2158 Australia. *Hydrology and Earth System Sciences* 20, 4625-4640.

2159 Tan, M., Baker, A., Genty, D., Smith, C., Esper, J., Cai, B.G., 2006. Applications of stalagmite laminae
2160 to paleoclimate reconstructions: Comparison with dendrochronology/climatology. *Quaternary Sci.*
2161 *Rev.* 25, 2103-2117.

2162 Taylor, W., Shnaider, S., Abdykanova, A., Fages, A., Welker, F., Irmer, F., Seguin-Orlando, A., Khan, N.,
2163 Douka, K., Kolobova, K., Orlando, L., Krivoshapkin, A., Boivin, N., 2018. Early pastoral economies
2164 along the Ancient Silk Road: Biomolecular evidence from the Alay Valley, Kyrgyzstan. *Plos One* 13,
2165 e0205646.

2166 Thompson, G.M., Lumsden, D.N., Walker, R.L., Carter, J.A., 1975. Uranium series dating of
2167 stalagmites from Blanchard Springs Caverns, U.S.A. *Geochim. Cosmochim. Acta* 39, 1211-1218.

2168 Treble, P., Shelley, J.M.G., Chappell, J., 2003. Comparison of high resolution sub-annual records of
2169 trace elements in a modern (1911-1992) speleothem with instrumental climate data from southwest
2170 Australia. *Earth Planet. Sci. Lett.* 216, 141-153.

2171 Treble, P.C., Bradley, C., Wood, A., Baker, A., Jex, C.N., Fairchild, I.J., Gagan, M.K., Cowley, J., Azcurra,
2172 C., 2013. An isotopic and modelling study of flow paths and storage in Quaternary calcarenite, SW
2173 Australia; implications for speleothem paleoclimate records. *Quaternary Sci. Rev.* 64, 90-103.

2174 Treble, P.C., Chappell, J., Gagan, M.K., McKeegan, K.D., Harrison, T.M., 2005a. In situ measurement
2175 of seasonal $\delta^{18}\text{O}$ variations and analysis of isotopic trends in a modern speleothem from southwest
2176 Australia. *Earth Planet. Sci. Lett.* 233, 17-32.

2177 Treble, P.C., Chappell, J., Shelley, J.M.G., 2005b. Complex speleothem growth processes revealed by
2178 trace element mapping and scanning electron microscopy of annual layers. *Geochim. Cosmochim.*
2179 *Acta* 69, 4855-4863.

2180 Treble, P.C., Schmitt, A.K., Edwards, R.L., McKeegan, K.D., Harrison, T.M., Grove, M., Cheng, H.,
2181 Wang, Y.J., 2007. High resolution Secondary Ionisation Mass Spectrometry (SIMS) $\delta\text{O-18}$
2182 analyses of Hulu Cave speleothem at the time of Heinrich Event 1. *Chem. Geol.* 238, 197-212.

2183 Tremaine, D.M., Froelich, P.N., Wang, Y., 2011. Speleothem calcite farmed in situ: Modern
2184 calibration of $\delta^{18}\text{O}$ and $\delta^{13}\text{C}$ paleoclimate proxies in a continuously-monitored natural cave system.
2185 *Geochimica et Cosmochimica Acta* 75, 4929-4950.

2186 Valley, J.W., Kita, N.T., 2009. In situ oxygen isotope geochemistry by ion microprobe, MAC short
2187 course: secondary ion mass spectrometry in the earth sciences, pp. 19-63.

2188 Vanghi, V., Borsato, A., Frisia, S., Howard, D., Gloy, G., Hellstrom, J., Bajo, P., 2019. High-resolution
2189 synchrotron X-ray fluorescence investigation of calcite coralloid speleothems: Elemental
2190 incorporation and their potential as environmental archives. *Sedimentology* 66, 2661–2685.

2191 Verheyden, S., Genty, D., Deflandre, G., Quinif, Y., Keppens, E., 2008. Monitoring climatological,
2192 hydrological and geochemical parameters in the Pere Noel cave (Belgium): implication for the
2193 interpretation of speleothem isotopic and geochemical time-series. *Int J Speleol* 37, 221-234.

2194 Vonhof, H.B., de Graaf, S., Spero, H.J., Schiebel, R., Verdegaal, S.J.A., Metcalfe, B., Haug, G.H., 2020.
2195 High-precision stable isotope analysis of <5 µg CaCO₃ samples by continuous-flow mass
2196 spectrometry. *Rapid Commun. Mass Spectrom.* 34, e8878.

2197 Vonhof, H.B., van Breukelen, M.R., Postma, O., Rowe, P.J., Atkinson, T.C., Kroon, D., 2006. A
2198 continuous-flow crushing device for on-line delta H-2 analysis of fluid inclusion water in
2199 speleothems. *Rapid Commun. Mass Spectrom.* 20, 2553-2558.

2200 Waite, A.J., Swart, P.K., 2015. The inversion of aragonite to calcite during the sampling of skeletal
2201 archives: Implications for proxy interpretation. *Rapid Commun Mass Spectrom* 29, 955-964.

2202 Walczak, I.W., 2016. Holocene climate variability revealed using geochemistry and Computed
2203 Tomography scanning of stalagmites from the North Atlantic Basin, Earth Sciences. Durham
2204 University, Durham, p. 199.

2205 Walczak, I.W., Baldini, J.U.L., Baldini, L.M., McDermott, F., Marsden, S., Standish, C.D., Richards, D.A.,
2206 Andreo, B., Slater, J., 2015. Reconstructing high-resolution climate using CT scanning of unsectioned
2207 stalagmites: A case study identifying the mid-Holocene onset of the Mediterranean climate in
2208 southern Iberia. *Quaternary Sci. Rev.* 127, 117-128.

2209 Wang, C., Bendle, J.A., Greene, S.E., Griffiths, M.L., Huang, J., Moossen, H., Zhang, H., Ashley, K., Xie,
2210 S., 2019a. Speleothem biomarker evidence for a negative terrestrial feedback on climate during
2211 Holocene warm periods. *Earth Planet. Sci. Lett.* 525, 115754.

2212 Wang, J.K., Johnson, K.R., Borsato, A., Amaya, D.J., Griffiths, M.L., Henderson, G.M., Frisia, S., Mason,
2213 A., 2019b. Hydroclimatic variability in Southeast Asia over the past two millennia. *Earth Planet. Sci.*
2214 *Lett.* 525, 115737.

2215 Wang, X.F., Edwards, R.L., Auler, A.S., Cheng, H., Kong, X.G., Wang, Y.J., Cruz, F.W., Dorale, J.A.,
2216 Chiang, H.W., 2017. Hydroclimate changes across the Amazon lowlands over the past 45,000 years.
2217 *Nature* 541, 204–207.

2218 Wang, Y.J., Cheng, H., Edwards, R.L., An, Z.S., Wu, J.Y., Shen, C.-C., Dorale, J.A., 2001. A high-
2219 resolution absolute-dated late Pleistocene monsoon record from Hulu Cave, China. *Science* 294,
2220 2345-2348.

2221 Wassenburg, J., Immenhauser, A., Richter, D., Jochum, K., Fietzke, J., Deininger, M., Goos, M., Scholz,
2222 D., Sabaoui, A., 2012. Climate and cave control on Pleistocene/Holocene calcite-to-aragonite
2223 transitions in speleothems from Morocco: Elemental and isotopic evidence. *Geochim. Cosmochim.*
2224 *Acta* 92, 23–47.

2225 Webb, M., Dredge, J., Barker, P.A., Müller, W., Jex, C., Desmarchelier, J., Hellstrom, J., Wynn, P.M.,
2226 2014. Quaternary climatic instability in south-east Australia from a multi-proxy speleothem record. *J.*
2227 *of Quaternary Sci.* 29, 589-596.

2228 Welte, C., Wacker, L., Hattendorf, B., Christl, M., Fohlmeister, J., Breitenbach, S.F.M., Robinson, L.F.,
2229 Andrews, A.H., Freiwald, A., Farmer, J.R., Yeman, C., Synal, H.A., Gunther, D., 2016. Laser Ablation -
2230 Accelerator Mass Spectrometry: An Approach for Rapid Radiocarbon Analyses of Carbonate Archives
2231 at High Spatial Resolution. *Anal. Chem.* 88, 8570-8576.

2232 Wiedenbeck, M., Bugoi, R., Duke, M.J.M., Dunai, T., Enzweiler, J., Horan, M., Jochum, K.P., Linge, K.,
2233 Kosler, J., Merchel, S., Morales, L.F.G., Nasdala, L., Stalder, R., Sylvester, P., Weis, U., Zoubir, A., 2012.

- 2234 GGR Biennial Critical Review: Analytical Developments Since 2010. *Geostandards and Geoanalytical*
2235 *Research* 36, 337-398.
- 2236 Wong, C.I., Banner, J.L., Musgrove, M., 2011. Seasonal dripwater Mg/Ca and Sr/Ca variations driven
2237 by cave ventilation: Implications for and modeling of speleothem paleoclimate records. *Geochimica*
2238 *et Cosmochimica Acta* 75, 3514-3529.
- 2239 Wong, C.I., Breecker, D.O., 2015. Advancements in the use of speleothems as climate archives.
2240 *Quaternary Science Reviews* 127, 1-18.
- 2241 Woodhead, J.D., Hellstrom, J., Hergt, J.M., Greig, A., Maas, R., 2007. Isotopic and elemental imaging
2242 of geological materials by laser ablation inductively coupled plasma-mass spectrometry.
2243 *Geostandards and Geoanalytical Research* 31, 331-343.
- 2244 Woodhead, J.D., Horstwood, M.S.A., Cottle, J.M., 2016. Advances in isotope ratio determination by
2245 LA-ICP-MS. *Elements* 12, 317-322.
- 2246 Wortham, B.E., Montanez, I.P., Rowland, D.J., Lerche, M., Browning, A., 2019. Mapping Fluid-Filled
2247 Inclusions in Stalagmites Using Coupled X-Ray and Neutron Computed Tomography: Potential as a
2248 Water Excess Proxy. *Geochemistry Geophysics Geosystems* 20, 2647-2656.
- 2249 Wu, X., Zhu, X., Pan, M., Zhang, M., 2014. Seasonal variability of oxygen and hydrogen stable
2250 isotopes in precipitation and cave drip water at Guilin, southwest China. *Environmental Earth*
2251 *Sciences* 72, 3183-3191.
- 2252 Wycech, J.B., Kelly, D.C., Kozdon, R., Orland, I.J., Spero, H.J., Valley, J.W., 2018. Comparison of $\delta^{18}\text{O}$
2253 analyses on individual planktic foraminifer (*Orbulina universa*) shells by SIMS and gas-source mass
2254 spectrometry. *Chemical Geology* 483, 119-130.

2255 Wynn, P.M., Fairchild, I.J., Borsato, A., Spotl, C., Hartland, A., Baker, A., Frisia, S., Baldini, J.U.L., 2018.
2256 Sulphate partitioning into calcite: Experimental verification of pH control and application to
2257 seasonality in speleothems. *Geochim. Cosmochim. Acta* 226, 69-83.

2258 Wynn, P.M., Fairchild, I.J., Frisia, S., Spotl, C., Baker, A., Borsato, A., EIMF, 2010. High-resolution
2259 sulphur isotope analysis of speleothem carbonate by secondary ionisation mass spectrometry.
2260 *Chemical Geology* 271, 101-107.

2261 Wynn, P.M., Fairchild, I.J., Spotl, C., Hartland, A., Matthey, D., Fayard, B., Cotte, M., 2014. Synchrotron
2262 X-ray distinction of seasonal hydrological and temperature patterns in speleothem carbonate.
2263 *Environ Chem* 11, 28-36.

2264 Yonge, C.J., Ford, D.C., Gray, J., Schwarcz, H.P., 1985. Stable isotope studies of cave seepage water.
2265 *Chemical Geology* 58, 97-105.

2266 Zeng, G., Luo, W., Wang, S., Du, X., 2015. Hydrogeochemical and climatic interpretations of isotopic
2267 signals from precipitation to drip waters in Liangfeng Cave, Guizhou Province, China. *Environmental*
2268 *Earth Sciences* 74, 1509-1519.

2269

2270 **Figure Captions:**

2271 Figure 1: Top Panel: Resolution of speleothem isotope records over time, compiled from the
2272 SISALv1b database. Individual record resolution (small black circles) and mean resolution of
2273 all available (black bars) and Holocene (blue bars) records published in a given year. Bottom
2274 panel: Total number of stalagmite records identified (grey bars), total number of stalagmite
2275 records in SISALv1b (black bars), and total number of Holocene records in SISALv1b (blue
2276 bars).

2277 Figure 2: Illustration of different drip responses from Yok Balum Cave, Belize, over
2278 approximately two months as captured by a series of automated drip loggers. Two clear rain
2279 events and the subsequent drip responses are indicated by the vertical dashed red lines.
2280 Rainfall amount is recorded directly over the cave site using a tipping bucket rain gauge.
2281 Techniques are discussed in more detail in (Ridley et al., 2015a).

2282 Figure 3: A new drip categorisation scheme designed to emphasise cave drip seasonality.
2283 The scheme does not use classification boundaries as such, but instead uses the data
2284 distribution to understand the hydrology. The scheme uses descriptors that map onto
2285 established drip terminology (see Panels B-D and main text for examples). A) Minimum and
2286 maximum hourly drip rates extracted for every month of record for numerous cave drips
2287 globally. The dashed line represents the 1:1 line, and all data points must necessarily plot
2288 over this (i.e., the minimum drip rate cannot exceed the maximum drip rate for any given
2289 month). The closer a point plots to the dashed line, the lower the difference between
2290 monthly maximum and minimum values for that point; if a point sits on the line the
2291 minimum and maximum values for that month are identical. Panels B-D illustrate some
2292 common drip types (using synthetic data) and their pattern when plotted on this diagram.
2293 Panels B-D are schematic and are not based on actual collected datasets; the symbols used
2294 are arbitrary and are not linked to the symbols used in Panel A.

2295 Figure 4: The simulated effects of sampling resolution on the climate signal extracted from a
2296 stalagmite. The stalagmite data are from stalagmite YOK-G (Yok Balum Cave, Belize), which
2297 was originally sampled with a micromill at a 100 micron (0.1 mm) step size (Ridley et al.,
2298 2015b). The chronology for the stalagmite is precise at the seasonal scale. The rainfall data

2299 (bottom panel) are from the Punta Gorda meteorological station (~30 km to the southeast
2300 of the cave site).

2301 Figure 5: Schematic of a sampling scheme for achieving ~50 micron spatial resolution. Plan
2302 view of a stalagmite surface with 1 mm conventional holes on the right and trenches cut for
2303 low and high resolution. The red trench was milled with a 0.8 mm diameter drill and the (blue-
2304 shaded) higher resolution trench was cut laterally, with each sample integrating 50 μm . The
2305 red corners highlight the area that is incorporated into subsequent steps, which in this case
2306 includes material from the current and the previous sample. In this example each high-
2307 resolution sample (e.g., yellow shaded area) integrates a minimal amount of powder of an
2308 older sample (because the milling direction is upward).

2309 Figure 6: Several examples of output generated by different geochemical-based techniques
2310 for extracting seasonal climate. A) Variability in sulphate in speleothem calcite (Obi84, Obir
2311 cave, Austria) as determined by SR- μXRF (Wynn et al., 2014). The clear annual sulphur maxima
2312 are evident as brighter green colours. B) Ion microprobe-resolved strontium and phosphorous
2313 cycles apparent in stalagmite CC3 from Crag Cave, southwestern Ireland (Baldini et al., 2002).
2314 The well-developed cycles illustrate stronger seasonality at the time of deposition (~8.336 ka
2315 BP) than currently present. C) Annual UV-luminescent banding in a stalagmite from Shihua
2316 Cave, Beijing, China (adapted from Tan et al. (2006)). D) well-develop carbon isotope ratio
2317 cycles in stalagmite YOK-G from Yok Balum Cave, Belize, constructed using data obtained via
2318 micromilling at a 100-micron spatial resolution and analyses of powders on an IRMS (Ridley
2319 et al., 2015b) (see also Figure 4). E) Mg cycles apparent in stalagmite BER-SWI-13 from
2320 Leamington Cave, Bermuda, resolved using LA-ICPMS-derived Mg data (Walczak, 2016). All
2321 panels show three to four cycles, interpreted as annual.

2322 Figure 7: A synthetic rainfall input signal (orange circles) with an annual temperature range of
2323 15 °C compared with two mean model outputs, one derived using an annual temperature
2324 range of 10 ± 6 °C (grey line), and another derived using an annual temperature range of $15 \pm$
2325 6 °C (blue line). At the beginning of the simulated rainfall input signal record (year = 0), April
2326 is the wettest month and November the driest month, but this shifts in polarity slowly through
2327 the record, moving through a brief phase with no seasonality in rainfall (year = 7), and then
2328 transitioning into a phase where April is the driest month (from year = 8). The vertical gridlines
2329 highlight the month of April during every model year. The simulated rainfall input signal
2330 amplitude and polarity is reproduced by the model very satisfactorily, provided that the
2331 model temperature range is realistic, as it is in Model 2. Note that the polarity of the simulated
2332 rainfall input signal is still reproduced by Model 1, but modelled rainfall seasonal amplitude
2333 is too large in order to compensate for the low amplitude of the modelled temperature range.

2334 Figure 8: Temperature (top panel) and rainfall (bottom panel) modelling results (black
2335 dashed lines) against 'noisy' synthetic input datasets (solid coloured lines) for seven model
2336 years. The grey rectangle highlights one model year (Year 4) where the input rainfall signal
2337 polarity was reversed; the model detects this shift. The modelling results presented are the
2338 mean values of all successful model runs for each timeslice.

2339 Figure 9: Mean modelled monthly temperature and rainfall data against Global Historical
2340 Climate Network (GHCN) and tree ring data. A) Stalagmite Keklik1 oxygen isotope ratio data
2341 from Bir-Uja Cave, Kyrgyzstan (input data) (Fohlmeister et al., 2017). B) Centennial-scale
2342 borehole temperature data from the Tian Shan region (Huang et al., 2000) from 1500 to
2343 2000 C.E. (input data, shifted upwards for clarity) (blue diamonds), modelled July
2344 temperature (black curve) (output), and NTREND summer temperature reconstruction for

2345 Asia Grid 2 (AG2) (red curve) (Cook et al., 2013). C) Modelled January rainfall (black curve)
2346 (output) and GHCN January rainfall for Tashkent (orange curve), both in % of total annual
2347 rainfall. The grey rectangles highlight the years 1797 and 1815 C.E. discussed in the text.

2348 Figure 10: Global seasonality in annual temperature (°C) and annual precipitation (mm). A)
2349 The annual temperature range was calculated as the maximum temperature of the warmest
2350 month minus the minimum temperature of the coldest month averaged over the period
2351 1970-2000. B) Precipitation seasonality was calculated as the precipitation amount of the
2352 wettest month minus the precipitation amount of the driest month averaged over the
2353 period 1970-2000. WorldClim Version 2 data (<https://www.worldclim.org/>) were obtained
2354 at a 2.5 minute (~4.5 km at the equator) spatial resolution (Fick and Hijmans, 2017). The
2355 data span the period 1970-2000 and thus may reflect anthropogenically-influenced
2356 temperature seasonality as discussed in Santer et al. (2018). Therefore, although the general
2357 spatial pattern of temperature (and potentially precipitation) seasonality may persist into
2358 the past, the magnitude of seasonality shifts may deviate from that presented here,
2359 particularly when extending records into the preindustrial era.

2360 Figure 11: Global seasonality in amount-weighted precipitation $\delta^{18}\text{O}$ (‰ VWMOW). The
2361 amount-weighted mean (WM) monthly precipitation $\delta^{18}\text{O}$ data (IAEA/WMO, 2001) were
2362 used to determine the annual range in precipitation isotopes globally (calculated as the
2363 maximum monthly WM $\delta^{18}\text{O}$ minus minimum monthly WM $\delta^{18}\text{O}$ at 267 stations (yellow
2364 symbols) with a complete 12-month dataset over the period 1961-1999. GNIP station data
2365 were interpolated onto a 2.5° X 2.5° global grid (~278 km X 278 km) (IAEA, 2001).

2366 Figure 12: A Hovmöller plot of the annual cycle of total-column precipitable water vapour
2367 for Central America, based on daily ERA5 re-analysis data across the region from -110 to -

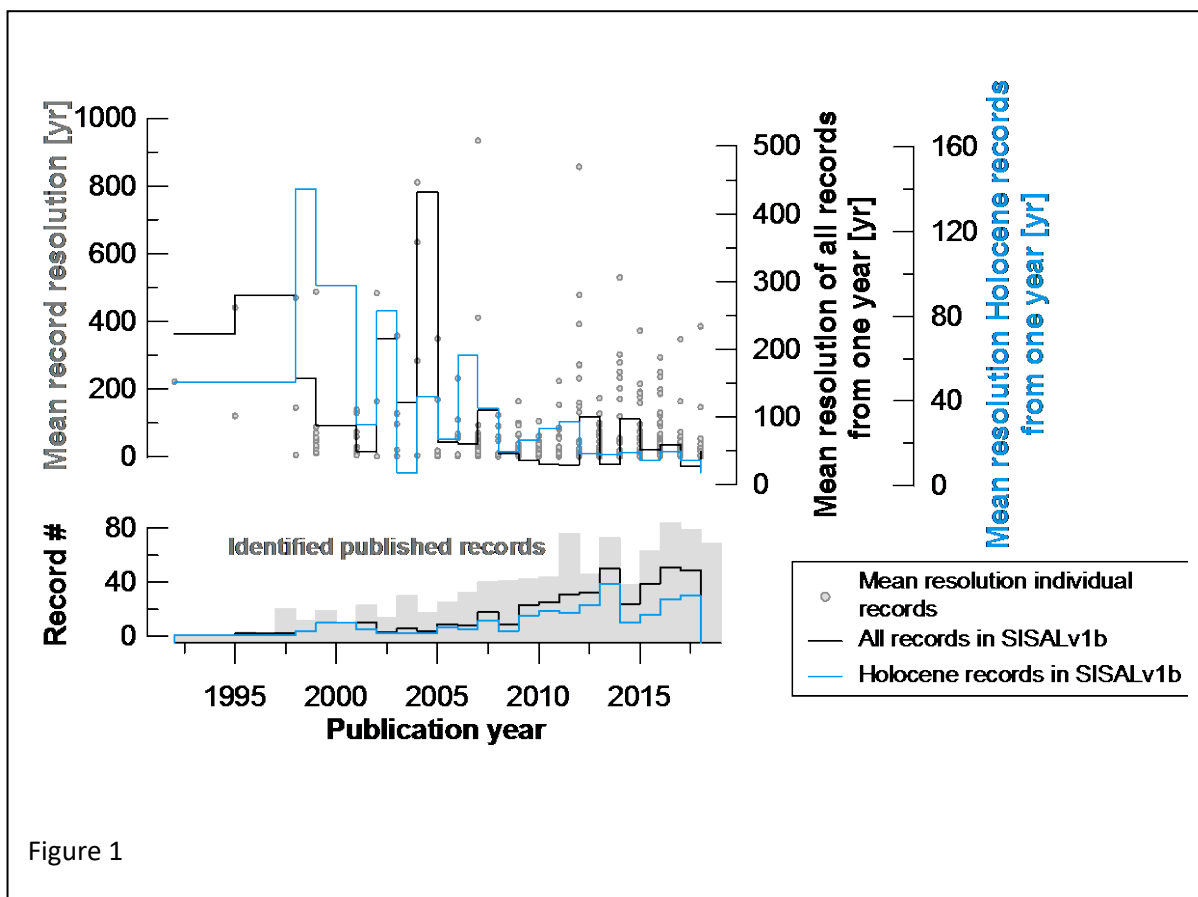
2368 80W and 0 to 35N for the period 1979-2018. Also indicated are the latitudes of three key
2369 cave sites that have yielded stalagmites which have produced oxygen isotope records of
2370 rainfall.

2371

2372 Figures:

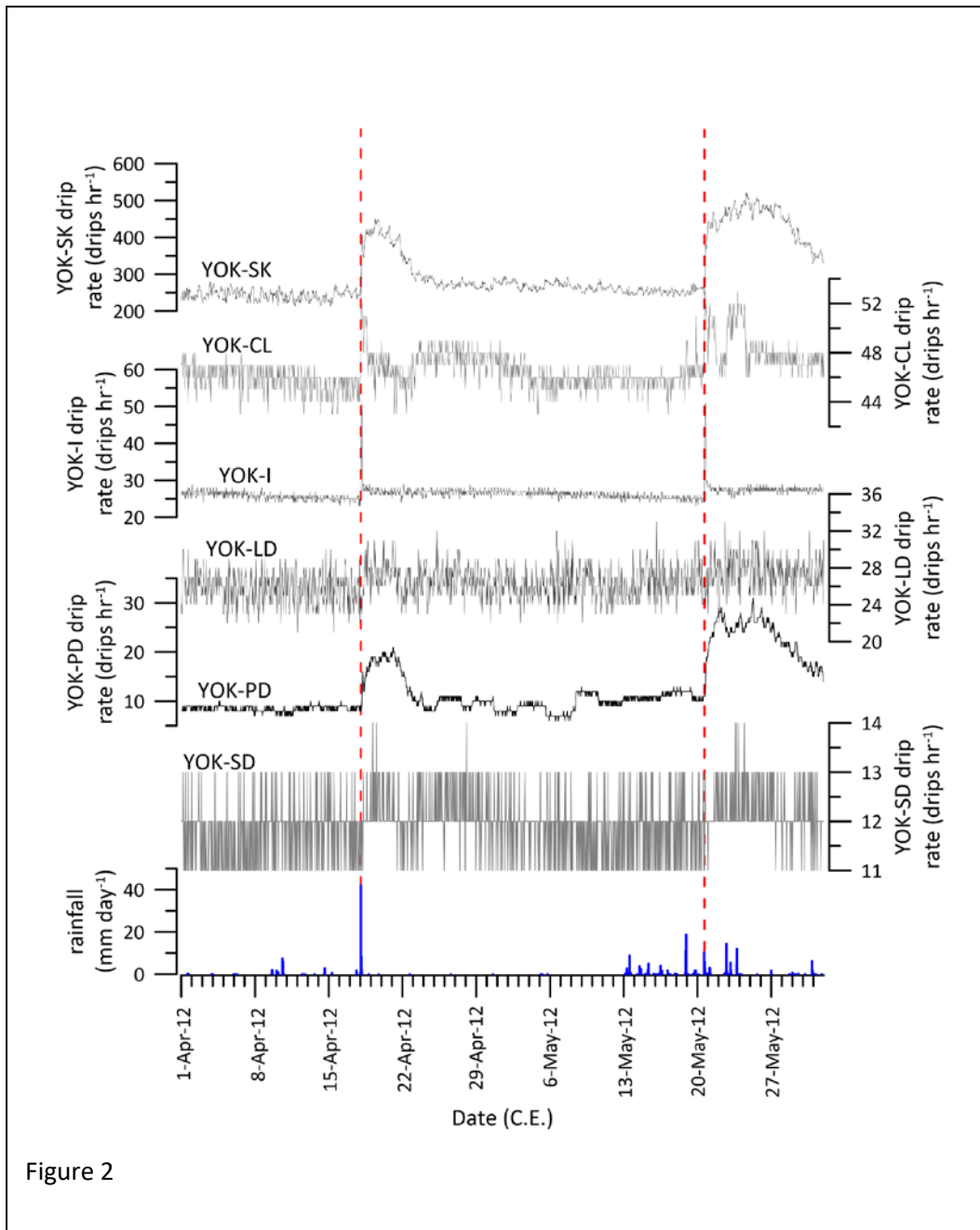
2373

2374



2375

2376



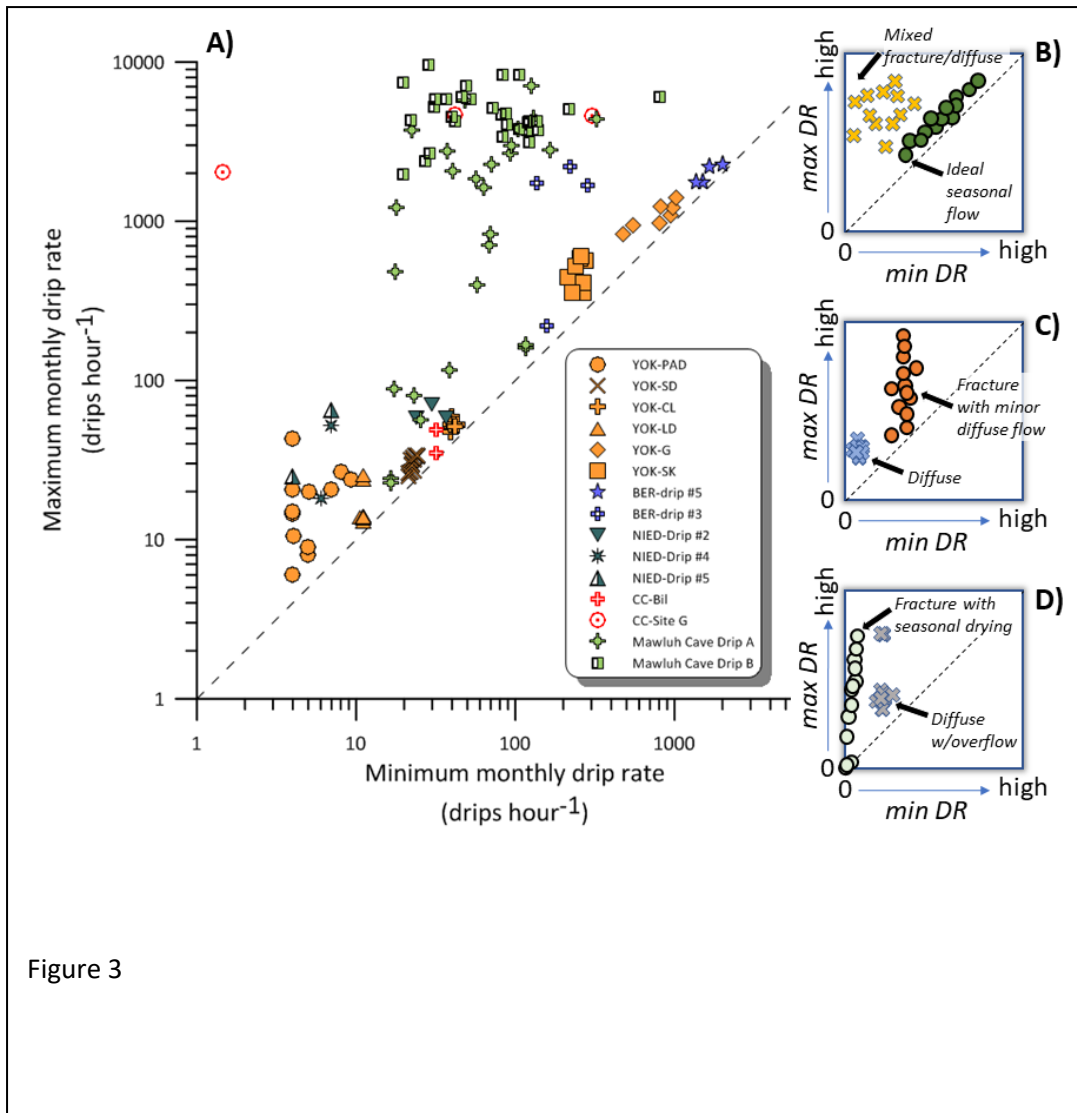


Figure 3

2380

2381

2382

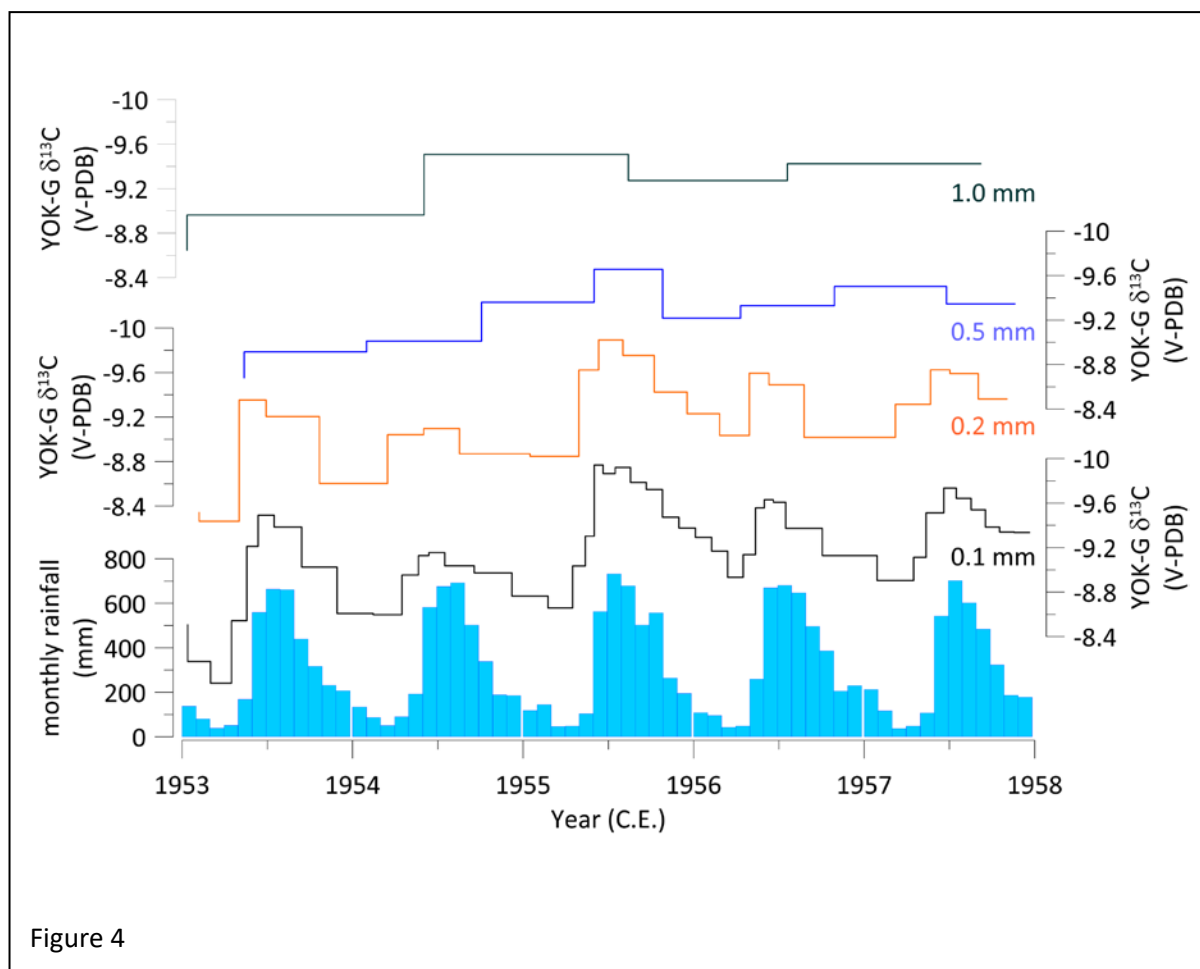


Figure 4

2383

2384

2385

2386

2387

2388

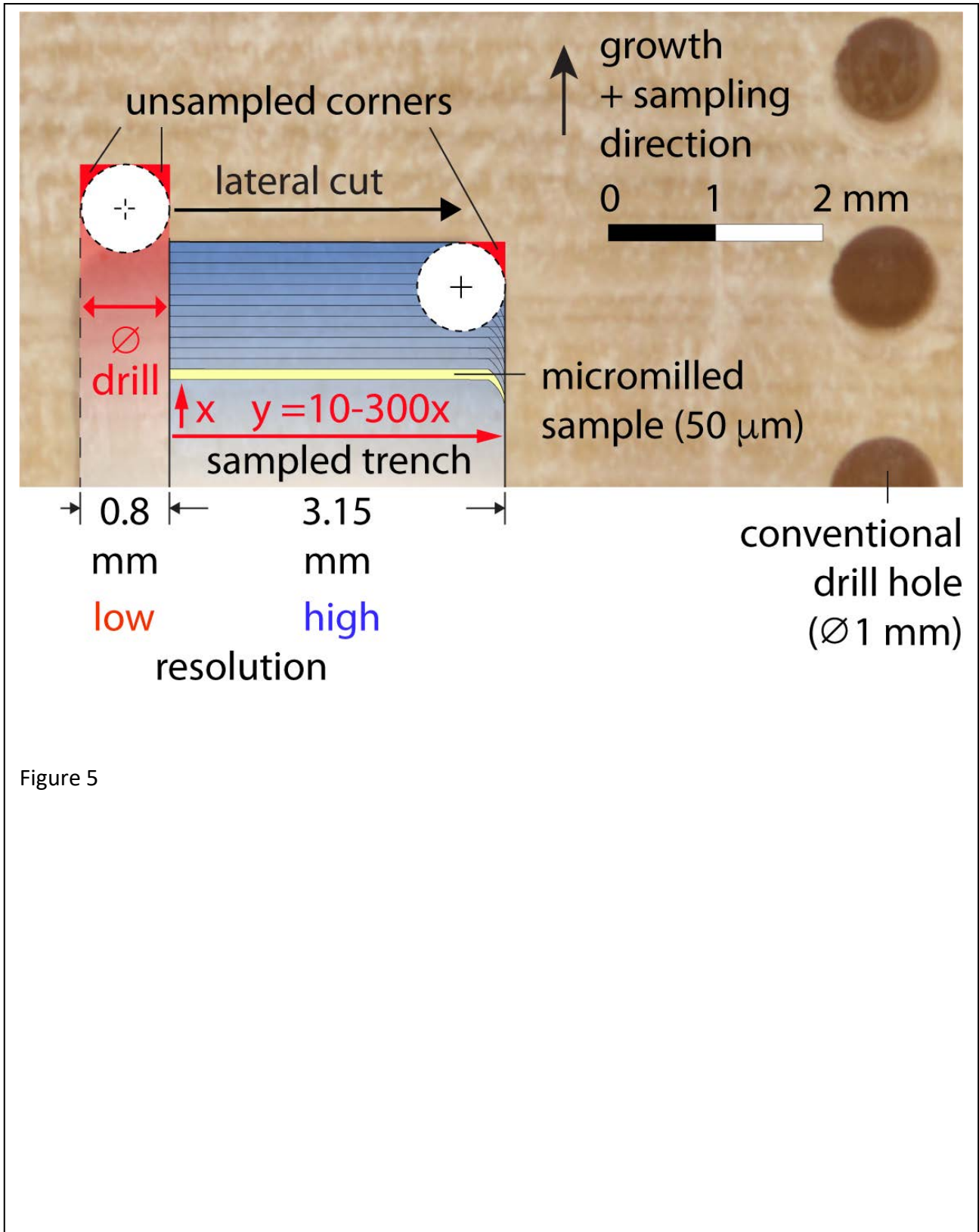


Figure 5

2391

2392

2393

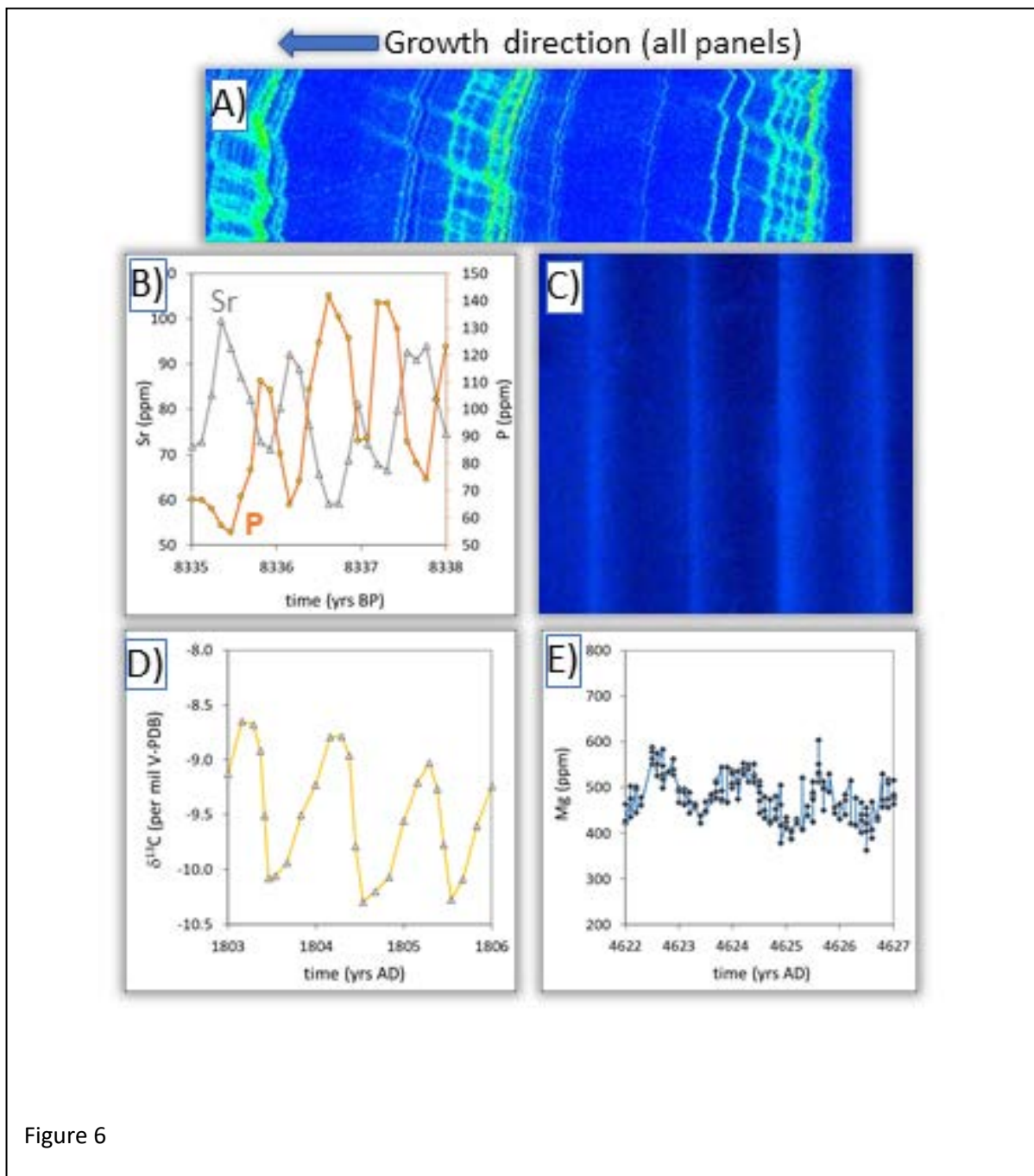


Figure 6

2394

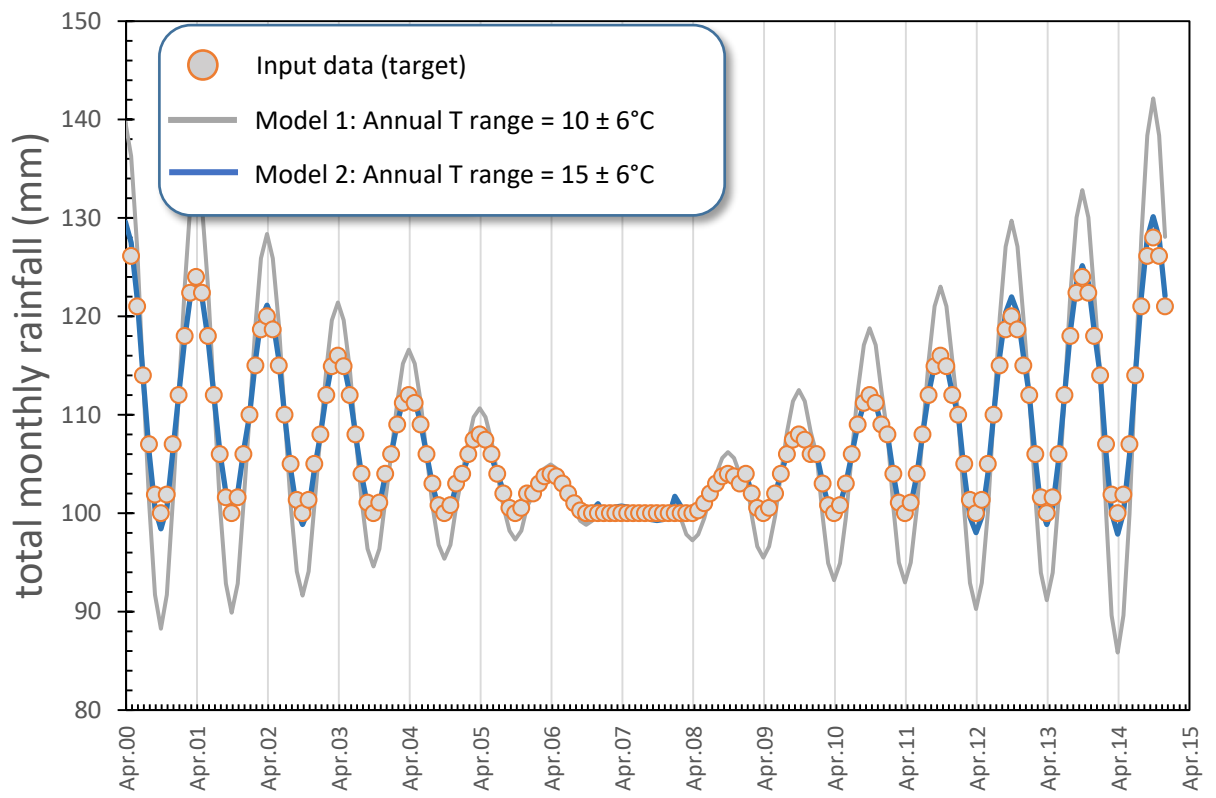


Figure 7

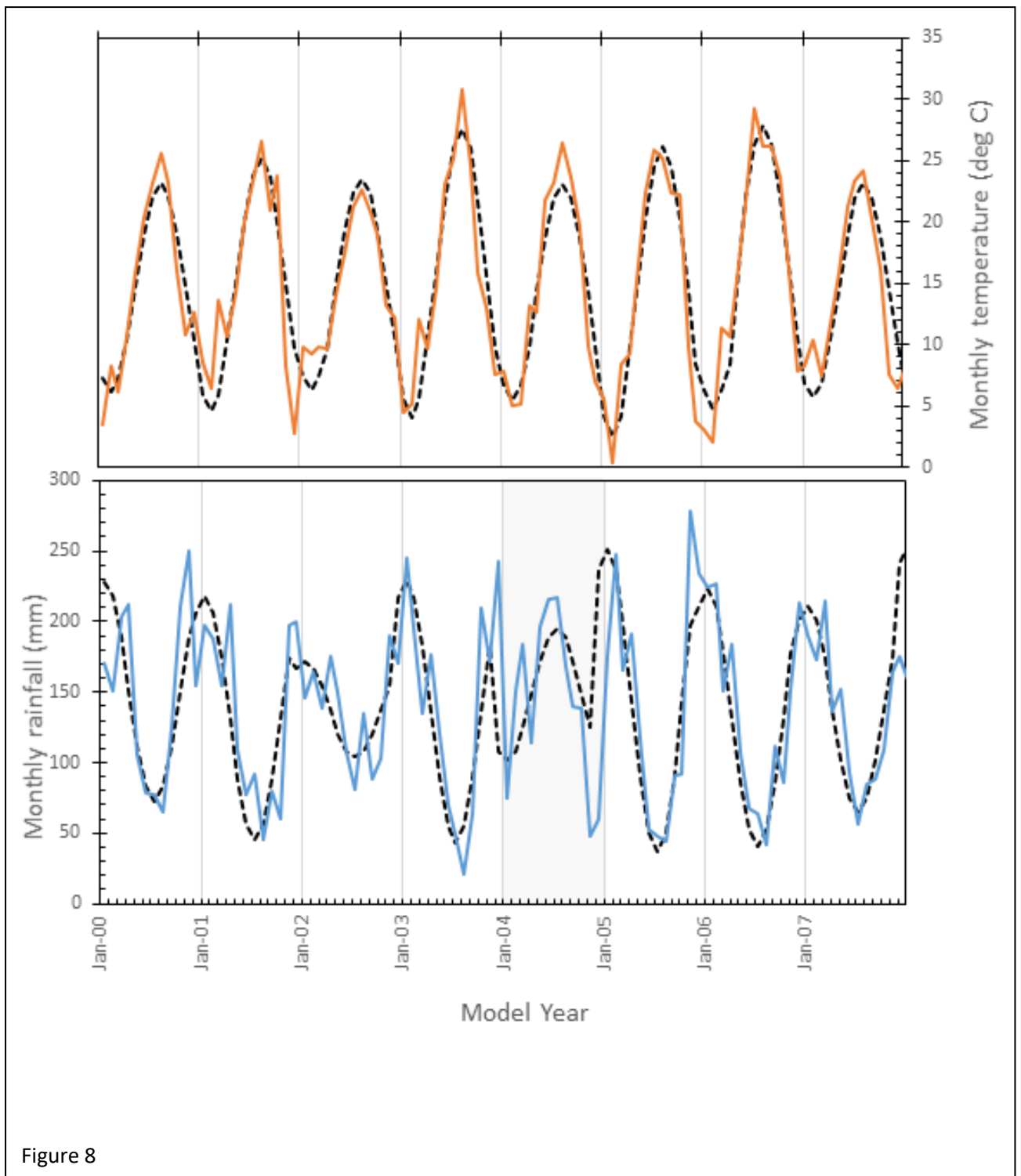


Figure 8

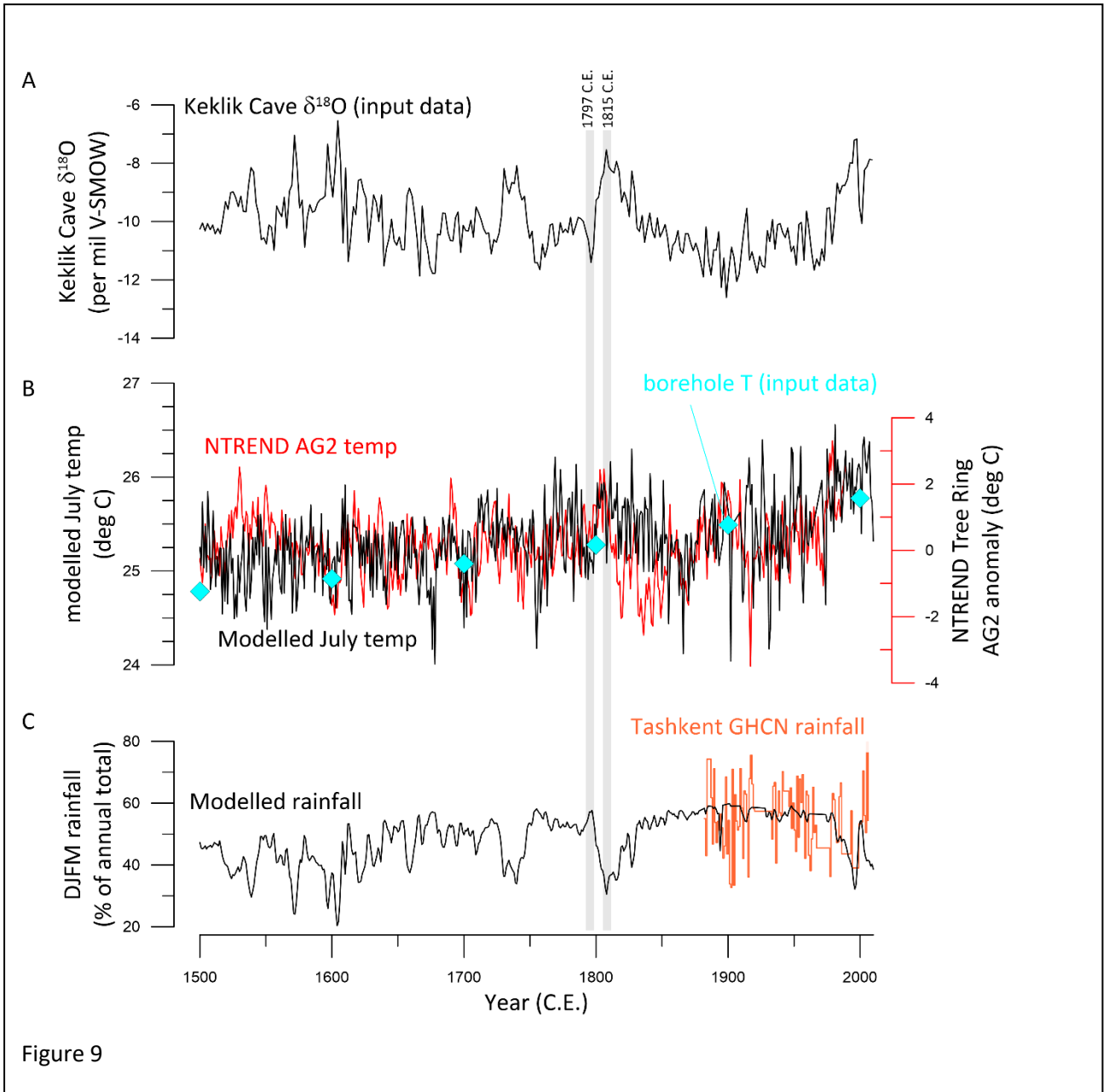


Figure 9

2401

2402

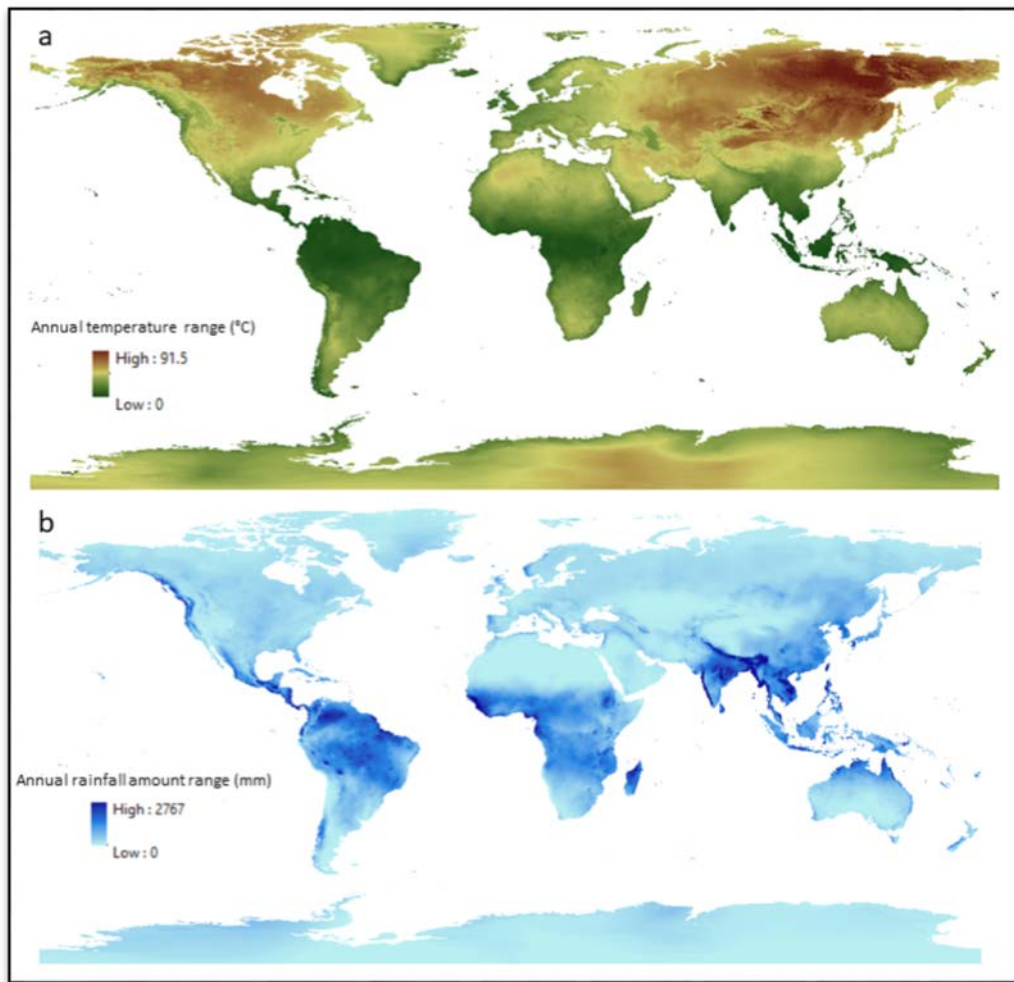


Figure 10

2405

2406

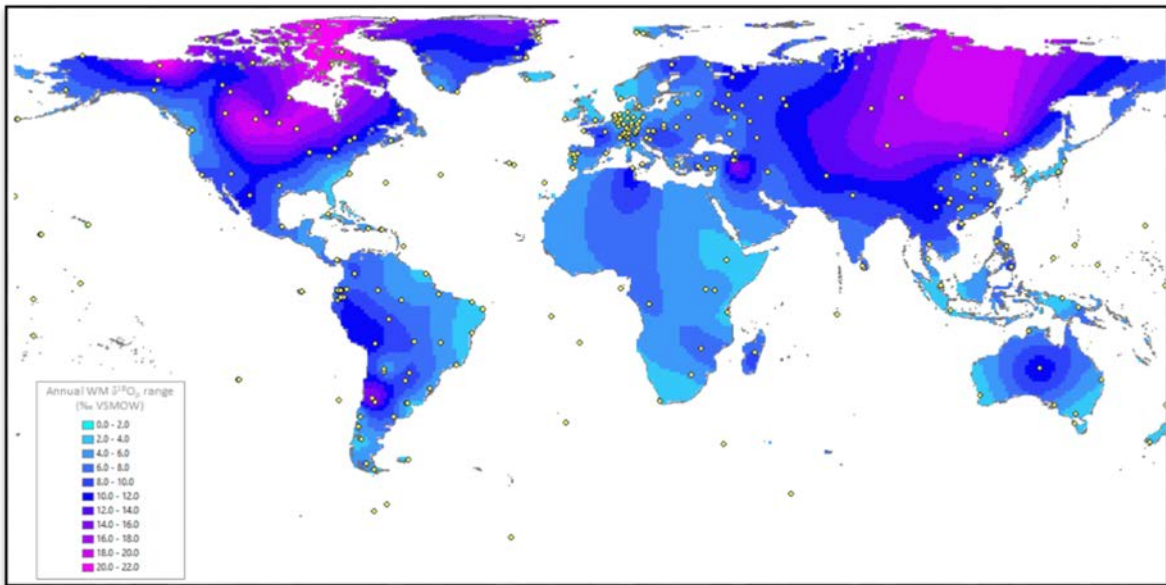
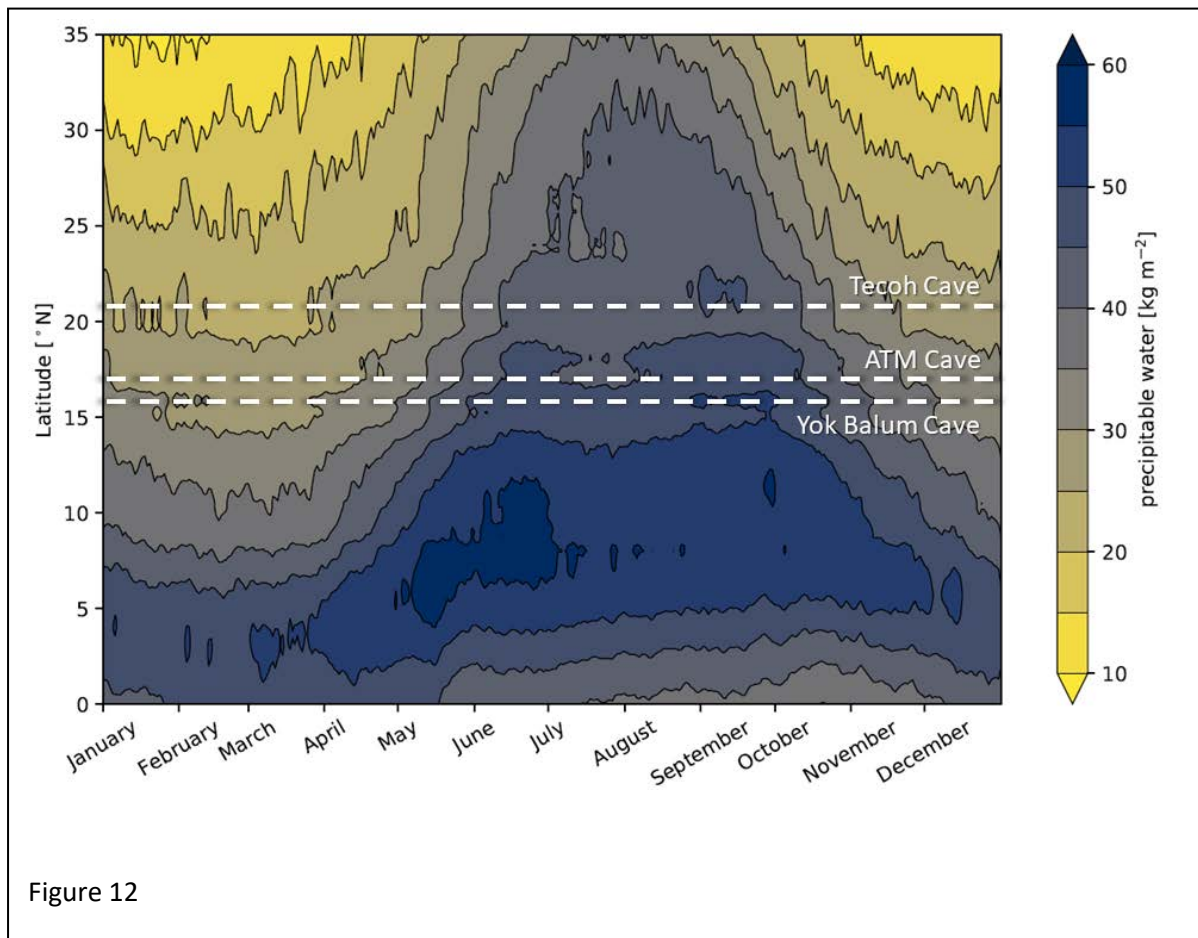


Figure 11

2407



2408

2409

2410